The modelling of the wind profile under stable stratification at heights relevant to wind power: A comparison of models of varying complexity

by

Michael Optis
B.Sc., University of Waterloo, 2005
M.A.Sc., University of Victoria, 2008

A Dissertation Submitted in Partial Fulfillment of the
Requirements for the Degree of

DOCTOR OF PHILOSOPHY

in the School of Earth and Ocean Sciences

The modelling of the wind profile under stable stratification at heights relevant to wind power: A comparison of models of varying complexity

by

Michael Optis
B.Sc., University of Waterloo, 2005
M.A.Sc., University of Victoria, 2008

Supervisory Committee

Dr. Adam Monahan, Supervisor
(School of Earth and Ocean Sciences)

Dr. Jody Klymak, Departmental Member
(School of Earth and Ocean Sciences)

Dr. Norm McFarlane, Scientist Emeritus
(School of Earth and Ocean Sciences)

Dr. Curran Crawford, Departmental Member
(Department of Engineering)

Supervisory Committee

Dr. Adam Monahan, Supervisor
(School of Earth and Ocean Sciences)

Dr. Jody Klymak, Departmental Member
(School of Earth and Ocean Sciences)

Dr. Norm McFarlane, Scientist Emeritus
(School of Earth and Ocean Sciences)

Dr. Curran Crawford, Departmental Member
(Department of Engineering)

ABSTRACT

The accurate modelling of the wind speed profile at altitudes relevant to wind energy (i.e. up to 200 m) is important for preliminary wind resource assessments, forecasting of the wind resource, and estimating shear loads on turbine blades. Modelling of the wind profile at these altitudes is particularly challenging in stable stratification due to weak turbulence and the influence of a broad range of additional processes. Models used to simulate the wind profile range from equilibrium-based 1D analytic extrapolation models to time-evolving 3D atmospheric models. Extrapolation models are advantageous due to their low computational requirements but provide a very limited account of atmospheric physics. Conversely, 3D models are more physically comprehensive but have considerably higher computational cost and data requirements. The middle ground between these two approaches has been largely unexplored.

The intent of this research is to compare the ability of a range of models of varying complexity to model the wind speed profile up to 200 m under stable stratification.

I focus in particular on models that are more physically robust than conventional extrapolation models but less computationally expensive than a 3D model. Observational data taken from the 213-m Cabauw meteorological tower in the Netherlands provide a basis for much of this analysis.

I begin with a detailed demonstration of the limitations and breakdown in stable stratification of Monin-Obukhov similarity theory (MOST), the theoretical basis for the logarithmic wind speed profile model. I show that MOST (and its various modifications) are reasonably accurate up to 200 m for stratification no stronger than weakly stable. At higher stratifications, the underlying assumptions of MOST break down and large errors in the modelled wind profiles are found.

I then consider the performance of a two-layer MOST-Ekman layer model, which provides a more physically-comprehensive description of turbulence compared to MOST-based models and accounts for the Coriolis force and large-scale wind forcing (i.e. geostrophic wind). I demonstrate considerable improvements in wind profile accuracy up to 200 m compared to MOST-based approaches.

Next, I contrast the performance of a two-layer model with a more physically-comprehensive equilibrium-based single-column model (SCM) approach. I demonstrate several limitations of the equilibrium SCM approach - including frequent model breakdown - that limit its usefulness. I also demonstrate no clear association between the accuracy of the wind profile and the order of turbulence closure used in the SCM. Furthermore, baroclinic influences due to the land-sea temperature gradient are shown to have only modest influence on the SCM wind speed profile in stable conditions. Overall, the equilibrium SCM (when it does not break down) is found to generally outperform the two-layer model.

Finally, I contrast the performance of the equilibrium SCM with a time-evolving SCM and a time-evolving 3D mesoscale model using a composite set of low-level jet (LLJ) case studies as well as a 10-year dataset at Cabauw. For the LLJ case studies, the time-evolving SCM and 3D model are found to accurately simulate the evolving stratification, the inertial oscillation, and the LLJ. The equilibrium SCM is shown to have comparatively less skill. Over the full 10-year data set, the sensitivity of the time-evolving SCM to horizontally-driven temperature changes in the ABL is found to be a considerable limitation. Despite its various limitations and simplified physics, the time-evolving SCM is generally found to be equally as accurate as the mesoscale model while using a fraction of the computational cost and requiring only a minimal amount of easily attainable local observations.

Overall, the time-evolving SCM model is found to perform the best (considering both accuracy and robustness) compared to a range of equilibrium approaches as well as a time-evolving 3D model, while offering the best balance of observational data requirements, physical applicability, and computational requirements. This thesis presents a compelling case for the use of SCMs in the field of wind energy meteorology.

Contents

List of Tables

List of Figures

ACKNOWLEDGEMENTS

I would like to thank:

My partner Lara, for her encouragement, support, and for holding down the fort through the many long nights at work

Adam Monahan, for his mentoring, advice, and meticulous editing. This work has been strengthened immensely due to his contributions

My committee members, for their guidance in the early stages of my research, in particular the useful and gruelling candidacy exam

Fred Bosveld, for providing relevant data for this thesis as well as many useful comments and dialogues pertaining to the work

Pedro Jimenez, for providing the relevant data for this thesis

National Sciences and Engineering Research Council, for the Postgraduate Scholarship from 2010-2013

John Montalbano, for the Montalbano Scholars Fellowship from 2010-2013

Environment Canada, for the Atmospheric and Meteorological Graduate Award in 2012-2013

Canadian Meteorological and Oceanographic Society, for the 2012 Weather Research House Award

Chapter 1

Introduction

1.1 Background

Wind energy is currently the fastest growing source of renewable energy. The 550 TWh of electricity generated globally in 2013 represented nearly a three-fold increase from 2009 generation and 4 % of global electricity production that year (IEA, 2014). With this increased production comes an increased need for the accurate modelling of the wind speed profile across altitudes swept out by a wind turbine blade. Such modelling is crucial for preliminary resource assessments, forecasting of the wind resource, and estimating vertical wind shear across the rotor blades. As wind power varies with the cube of wind speed, small errors in wind speed can lead to large errors in wind power.

The shape of the wind profile can vary considerably depending on thermal stratification (Stull, 1988). In Fig. 1.1 we contrast wind, temperature, and turbulence profiles in two distinct regimes: unstable stratification (typical during a summer day), and stable stratification (typical during a summer night). Several length scales are shown in the figure (and discussed throughout this thesis). The surface layer (SL) height is conventionally defined as the height at which the momentum flux is 10% lower than the surface value and the atmospheric boundary layer (ABL) height is conventionally defined as the height at which the momentum flux is equal to 5% its surface value. The Obukhov length (L), precisely defined in Eq. 2.2 can be interpreted as the height below which the mechanical shear production of turbulence kinetic energy dominates over buoyant production.

Both the unstable and stable wind profiles (Fig. 1.1(a)) are logarithmic within the

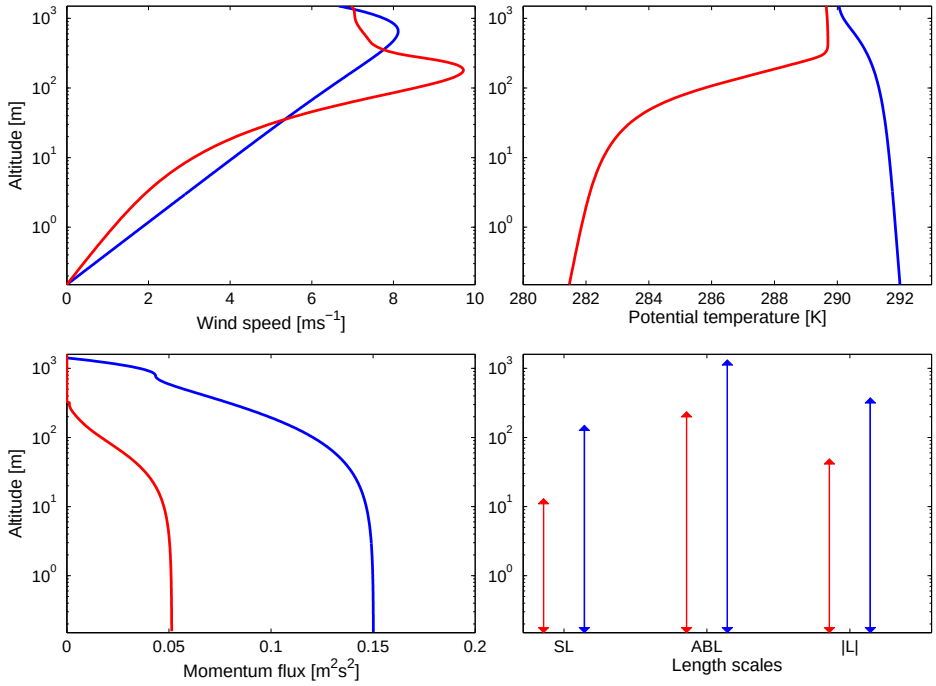

Figure 1.1: Comparison of atmospheric profiles for unstable conditions (blue) and stable conditions (red). Data are based on single-column model (SCM) simulations on May 5 2008 at 1400 UTC (unstable case) and May 6 2008 at 0400 UTC (stable case). See Chapter 5 for a detailed description of the simulations.

SL; however, the SL height is considerably lower for the stable case (about 10 m for the example shown) compared to the unstable case (about 150 m for this example). Peaks in the wind speed occur at about 180 m and 650 m for the stable and unstable cases, respectively. Potential temperature profiles are also distinct in the two cases (Fig. 1.1(b)). A negative gradient is observed in unstable conditions, and a sharper positive gradient in generally observed in stable conditions. We note that the ABL height coincides with the altitude at which the temperature gradient becomes small (approximately 230 m and 1300 m in stable and unstable conditions, respectively). The atmosphere is actively turbulent within the ABL, while in the layer above (often referred to as the residual layer) the turbulence dissipates over time. Increased turbulent mixing due to buoyant production of turbulence in unstable conditions leads to larger magnitudes of the momentum flux (Fig. 1.1(c)) compared to stable conditions, where negative buoyancy suppresses turbulent mixing. We also note a deeper constant flux layer near the surface in unstable conditions relative to stable conditions.

By definition, L is positive when the surface heat flux is downward (stable stratification) and negative when it is upward (unstable stratification). For the case under consideration, —L— is larger in unstable conditions relative to stable conditions, although this is not always generally the case.

The wind energy community has historically relied on idealized and quasi-empirical equilibrium-based (i.e. no time dependence) equations to extrapolate near-surface winds up to altitudes swept out by a wind turbine blade. The most commonly used equations include the power law profile (not based on atmospheric physics) and the logarithmic wind speed profile derived from Monin-Obukhov similarity theory (MOST) (Lange and Focken, 2005; Emeis, 2013). The logarithmic wind speed profile (generally recognized as more accurate than the power law profile) has been used extensively over the last 30 years (e.g. Holtslag, 1984; Troen and Petersen, 1989; Petersen et al., 1998; Burton et al., 2001; Lange and Focken, 2005; Motta et al., 2005; van den Berg, 2008; Monteiro et al., 2009; Emeis, 2010, 2013; Giebel, 2011; Drechsel et al., 2012).

Several assumptions underlying MOST limit its general applicability. These assumptions include constant turbulent fluxes with altitude, horizontally homogeneous surface roughness, and sustained, surface-based turbulence being the dominant process controlling vertical mixing. These assumptions have been found to provide reasonable approximations up to 100-200 m under unstable and neutral stratification where turbulent mixing is generally intense. Consequently, the logarithmic wind speed profile is generally accurate up to these altitudes under these conditions. Under stable stratification, turbulent fluxes can change considerably over much smaller altitude ranges, surface heterogeneities become more influential (Verkaik and Holtslag, 2007), and a range of processes other than turbulence can have considerable influence on vertical mixing and the wind profile (e.g. intermittent turbulence (Poulos et al., 2002), surface decoupling, gravity waves (Mahrt, 1998), baroclinicity (Mahrt, 1998), thin and 'upside-down' boundary layers (Mahrt and Vickers, 2002), and the Coriolis force causing rotation of the wind vector with altitude (Emeis, 2013), time-evolving inertial oscillations (Baas et al., 2012), and time-evolving low-level jets (Van de Wiel et al., 2010)). These factors limit the range of altitudes over which MOST should theoretically be reasonable.

The average maximum altitude swept out by a wind turbine blade was around 50 m in 1990 (Landtz et al., 2012). At that time, the logarithmic wind speed profile was generally sufficient for wind energy purposes in most atmospheric conditions

apart from the highest stability regimes. By 2000, the average maximum altitude had reached 80 m, and by 2010 it had reached 150 m (Landtz et al., 2012). The tallest wind turbine today sweeps out altitudes up to 220 m, and even larger turbines are being considered (WPM, 2015). Consequently, the logarithmic wind speed profile has become increasingly inappropriate for wind energy purposes over a broader range of stability classes. Above 200 m, the use of the logarithmic wind speed profile in neutral and possibly unstable conditions may often be inappropriate.

Despite these limitations, the logarithmic wind speed profile - and various modifications to it - are still frequently applied in stable stratification at inappropriately high altitudes (e.g. Gryning et al., 2007; Gryning and Batchvarova, 2008; Pena et al., 2010; Sathe et al., 2011, 2012; Kumar and Sharan, 2012). In this regard, a comprehensive demonstration of the limitations and breakdown of MOST under such conditions - currently absent in the literature - would be a valuable contribution to the field.

A better understanding of available models that are more applicable at higher altitudes and stratification is also required. A broad range of models are currently used for wind modelling at altitudes relevant to wind energy. These models range from simple equilibrium-based extrapolation equations to physically-comprehensive high-resolution 3D atmospheric models (e.g. large eddy simulations). In terms of equilibrium-based extrapolation models, a two-layer MOST-Ekman model represents a natural extension of MOST to account for processes well above the surface. In the two-layer model, the logarithmic wind speed equation is applied within the surface layer (where constant turbulent fluxes with altitude is a reasonable approximation) and the Ekman layer equations are applied above (Emeis, 2013). The two-layer model specifically accounts for the Coriolis force and the large-scale wind forcing (i.e. geostrophic wind), which should in principle provide more accurate wind profiles at higher altitudes compared to the logarithmic profile. A detailed analysis of the ability of such a model to extrapolate wind profiles has not previously been carried out.

High-resolution 3D models such as large-eddy simulations (LES) are limited by their computational cost. For wind resource assessment and forecasting purposes, mesoscale models (generally with horizontal resolutions above 1 km) generally provide the best balance of accuracy and computational cost. Mesoscale models - such as the Weather and Research Forecasting (WRF) model - are commonly used for purposes ranging from resource assessments, wind farm siting, predicting ramp events, and turbine spacing (e.g. Storm et al., 2009, 2010; Floors et al., 2013; Zhang et al.,

2013; Nunalee and Basu, 2014; Yang et al., 2014). Mesoscale models have considerable advantage over extrapolation equations due to the ability to incorporate time-dependence, the inclusion of 3D processes, and the more comprehensive account of atmospheric physics. However, the large data requirements (e.g. synoptic-scale forcings, detailed surface characteristics) and high computational cost may not be practical when quick and cost-effective methods for estimating the wind profile are required.

A single-column model (SCM) provides a useful middle ground between simple but highly-idealized extrapolation equations and physically-comprehensive but computationally-expensive 3D mesoscale models. SCMs are advantageous compared to 3D models due to their low computational requirements, flexibility in determining which processes and parameterizations are included (e.g. turbulence, radiation, entrainment, land surface characteristics, etc.), the ability to specify a lower boundary above the surface, and the ability to incorporate local observations. The complexity of an SCM can vary from models that incorporate the complete physics of a 3D model to highly idealized representations that consider only the momentum and temperature budgets. SCMs have been used successfully in idealized studies of the atmospheric boundary layer (e.g. Weng and Taylor, 2003, 2006; Cuxart et al., 2006; Edwards et al., 2006; Sterk et al., 2013; Sorbjan, 2012, 2014). However, the ability of SCMs to provide an accurate simulation of the observed wind profile over a broad range of atmospheric conditions has not been explored.

1.2 Dissertation objectives and outline

This thesis provides a detailed assessment of a range of models in the ability to simulate the wind profile up to 200 m under stable stratification. Observational data taken from the 213-m Cabauw meteorological tower in the Netherlands provide a basis for much of this analysis (Van Ulden and Wieringa, 1996). The tower is located in locally flat terrain with higher regional roughness due to small towns and belts of trees. This roughness distribution leads to a well-defined internal boundary layer at Cabauw. Furthermore, the proximity to the North Sea (about 50 km) and often large land-sea temperature gradients can lead to strong baroclinicity and temperature advection at the tower. Therefore, the wind regime at Cabauw is more complex than that of the prairies or offshore areas where surface roughness and temperatures are more horizontally homogeneous. Furthermore, the wind regime at Cabauw is less

complex than that of mountainous or urban areas where large changes in topography are observed.

There are 4 main objectives of this thesis:

1. Demonstrate in detail the limitations and breakdown of MOST and the associated logarithmic wind speed profile (including their various modifications)

2. Compare the performance of the logarithmic wind speed profile (and its various modifications) to the two-layer model

3. Compare the performance of the two-layer model with an equilibrium-based SCM

4. Compare the performance of an equilibrium SCM, a time-evolving SCM, and a 3D mesoscale model

Chapters 2 through 5 address objectives 1 through 4, respectively. An overview of the main contributions of the thesis, key conclusions drawn from the thesis results, and recommendations for future work are provided in Chapter 6. The work presented in Chapters 2 and 3 was done in collaboration with Fred Bosveld at the Royal Netherlands Meteorological Institute.

Chapter 2

Limitations and breakdown of Monin-Obukhov similarity theory for wind profile extrapolation under stable stratification

The contents of this chapter are based on the following manuscript:

Optis, M., A. Monahan, and F. Bosveld (2014). 'Limitations and breakdown of Monin-Obukhov similarity theory for wind profile extrapolation under stable stratification'. *Wind Energy*, accepted Dec. 2014.

Note that F. Bosveld provided and helped to interpret some data used in this analysis, and also provided feedback on the manuscript. The analysis presented here was conducted by M. Optis.

2.1 Introduction

2.1.1 The logarithmic wind speed model

The accurate characterization of the near-surface wind speed profile (up to altitudes of about 200 m) is important for a variety of wind energy applications, including wind energy resource assessment and forecasting, and estimating wind shear across turbine blades. In many cases, quick and cost-effective methods for wind energy assessment are needed, such as the preliminary assessment of a wind energy resource from field

data or real-time hub-height wind speed estimations upwind of a wind farm. For cases in which the measurement of near-surface wind speeds has been made (e.g. 10 m winds at nearby weather stations, 60 m winds at a meteorological tower), the extrapolation of near-surface winds to hub-height using simple diagnostic models is a practical and cost-effective approach.

The most established of these simple models is the logarithmic wind speed profile model, resulting from Monin-Obukhov similarity theory (MOST; Monin and Obukhov, 1954). According to MOST, any properly non-dimensionalized statistics of turbulence and the eddy-averaged flow can be expressed as a universal function of a non-dimensional parameter. The logarithmic wind speed profile in particular is derived from consideration of the non-dimensionalized vertical gradient of the wind speed,

$$\phi_m\left(\frac{z}{L}\right) = \frac{\kappa z}{u_*}\frac{\partial \bar{U}}{\partial z} \tag{2.1}$$

where ϕ_m is the non-dimensional wind shear (whose functional form is determined through a combination of theoretical and empirical analyses), κ is the von Karman constant (normally taken to be 0.4), $u_* = \left[\left(\overline{u'w'}\right)_s^2 + \left(\overline{v'w'}\right)_s^2\right]^{1/4}$ is the friction velocity derived from the two horizontal components of the surface vertical turbulent momentum flux, $\bar{U}$ is the wind speed averaged over turbulent timescales and z is the height above the surface. The dimensional quantity L is the Obukhov length,

$$L = -\frac{u_*^3 \theta_s}{\kappa g(\overline{w'\theta'})_s} \tag{2.2}$$

where g is the acceleration due to gravity, θ_s is the surface potential temperature, and $(\overline{w'\theta'})_s$ is the surface turbulent temperature flux. Over a range of altitudes for which u_* and $(\overline{w'\theta'})_s$ (and therefore L) vary weakly with altitude upward from the surface and can be approximated as being constant, integrating Eq. 2.1 between z and the roughness length z_0 (the height above the surface where the wind speed is defined to be zero) yields the well-known logarithmic wind speed equation,

$$\bar{U}(z) = \frac{u_*}{\kappa}\left[\ln\left(\frac{z}{z_0}\right) - \psi_m\left(\frac{z}{L}, \frac{z_0}{L}\right)\right] \tag{2.3}$$

where ψ_m accounts for the influence of stability and is derived from ϕ_m,

$$\psi_m\left(\frac{z}{L},\frac{z_0}{L}\right)=\int_{z_0/L}^{z/L}\frac{1-\phi_m(\zeta)}{\zeta}\,\mathrm{d}\zeta. \tag{2.4}$$

Although Eq. 2.3 is not strictly logarithmic when $\psi_m \neq 0$, we follow common practice in the literature and refer to Eq. 2.3 as the "logarithmic wind speed equation". Eq. 2.3 has frequently been used for wind energy resource assessment and forecasting at altitudes within a few hundred metres of the surface. Over the last two decades, it has been used extensively in the field of wind energy meteorology (e.g. Holtslag, 1984; Troen and Petersen, 1989; Petersen et al., 1998; Burton et al., 2001; Lange and Focken, 2005; Motta et al., 2005; van den Berg, 2008; Monteiro et al., 2009; Emeis, 2010, 2013; Giebel, 2011; Drechsel et al., 2012). For wind energy forecasting in particular, the logarithmic wind speed model has been used to interpolate wind speeds between two atmospheric model levels to hub-height, extrapolate observed wind speeds (e.g. tower measurements) to hub-height, or extrapolate the geostrophic winds to hub-height using the friction velocity computed from the geostrophic-drag law (Tennekes, 1973).

2.1.2 Assumptions of MOST

The approximation of constant turbulent fluxes with altitude required to derive Eq. 2.3 limits its application in several ways. The first limitation is that surrounding surface characteristics must be approximately horizontally homogeneous. When surrounding surface conditions are not homogeneous, the vertical structure of turbulence can vary considerably. In particular, changes in upstream surface roughness features can lead to the formation of internal boundary layers (IBLs) at a given location (Verkaik and Holtslag, 2007). These structures form because the properties of turbulence at higher altitudes are influenced by roughness features farther upstream due to the time taken for the turbulence generated by surface roughness elements to be mixed upwards. Turbulent statistics at a given altitude z are found to reflect roughness features a distance of roughly $10z$ upstream in neutral conditions (Verkaik and Holtslag, 2007). In the presence of IBLs, a single z_0 value used to construct the entire wind speed profile is inappropriate. Rather, different altitudes will be associated with different z_0 values. Various modifications to the logarithmic wind speed profile to account for IBLs have been proposed (e.g. Lange and Focken, 2005; Emeis, 2013).

Provided surface conditions are horizontally homogeneous, the approximation of constant turbulent fluxes with altitude still limits the application of the logarithmic wind speed model to the surface layer (SL), the lowermost portion of the atmospheric boundary layer (ABL) (bottom $\approx 10\%$) in which changes in the turbulent fluxes with altitude are small ($\approx 10\%$) compared to their surface values (Stull, 1988; Garratt, 1994). With increasing distance above the SL, turbulent fluxes generally decrease and the approximation of a constant flux profile becomes increasingly unrepresentative at higher altitudes.

The derivation of Eq. 2.3 additionally assumes that turbulence is the only mechanism controlling the wind speed profile and considers only the change of wind speed with altitude (and not separate wind vector components). These assumptions further limit the application of Eq. 2.3 to conditions in which the influence of other mechanisms controlling the vertical wind speed profile, as well as the rotation of the wind vector with altitude, are negligble. Specifically, these assumptions neglect the influence of the Coriolis force on the wind speed profile. The influence of the Coriolis force can be understood in terms of an idealized horizontal force balance between the pressure gradient force, momentum flux gradient and the Coriolis force, as illustrated in Fig. 2.1. Above the ABL, the momentum flux and its gradient are approximately zero and the wind vector flows along the isobars (i.e. the geostrophic wind). Within the ABL, the momentum flux gradient is non-negligible, and the resulting force balance rotates the wind vector in a cross-isobaric direction. Close to the surface (e.g. mid-SL and lower-SL), where the wind speed - and therefore the Coriolis force - is small, the dominant force balance is between the momentum flux gradient and the pressure gradient force. Consequently, the resulting wind directions are approximately the same over this range of heights. Therefore, the application of the logarithmic wind speed model is limited to low altitudes (i.e. within the SL) where the influence of the Coriolis force and the rotation of the wind vector are negligible.

2.1.3 Role of stability

The limitations of the logarithmic wind speed model described in Sect. 2.1.2 become more restrictive under increasing stable stratification. With increased stratification (and therefore decreased vertical turbulent mixing), the properties of turbulence at a given altitude are influenced by roughness features increasingly far upstream due to the larger time required for surface turbulence to be mixed upwards. In inhomo-

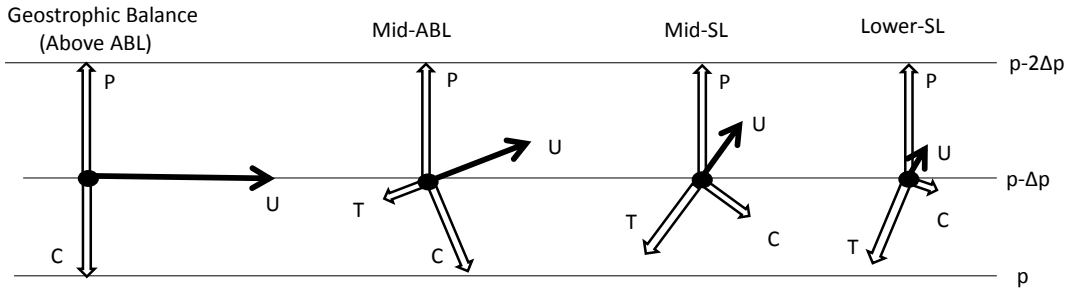

Figure 2.1: Idealized horizontal force balance of an air parcel at different altitudes and the resulting wind direction, assuming horizontal homogeneity and steady-state conditions (adapted from Holton (2004)). P denotes the pressure gradient force, C the Coriolis force, T the turbulent momentum flux gradient, and U the wind vector. Lines labelled p, $p - \Delta p$ and $p - 2\Delta p$ represent the horizontal isobars.

geneous terrain, IBL structures can persist over greater distances, leading to more complicated vertical structures of turbulence at a given location and possibly the presence of several IBLs at low altitudes (Holtslag, 1984; Verkaik and Holtslag, 2007). In the extreme stability limit, surface decoupling results in localized turbulence aloft, independent of upstream or local roughness (Nieuwstadt, 1984; Mahrt, 1999, 2014). The estimation of z_0 in inhomogeneous terrain is therefore more difficult in stable stratification. In fact, z_0 itself becomes a function of stratification. Conversely under unstable conditions, vertical turbulent mixing is strong, the upstream footprint is smaller, and the value of z_0 is simpler to estimate.

The height of the surface layer, h_{SL}, is also strongly influenced by stability. Under neutral and especially unstable conditions, vertical turbulent mixing is normally intense in the lower few hundred metres of the ABL, resulting in h_{SL} values as great as 200 m or more (Stull, 1988; Garratt, 1994). Under stable stratification, the suppression of vertical turbulent mixing results in a sharp decrease of turbulent fluxes with altitude from the near-surface shear layer. Consequently, the SL depth is significantly lower, ranging from about 20-30 m under moderately stable conditions to 1-5 m under extremely stable conditions (Holtslag, 1984; Stull, 1988; Garratt, 1994). Under these conditions, and to the extent that the assumptions of MOST are still valid (Mahrt, 1998), the logarithmic wind speed profile is valid only at very low altitudes.

Furthermore, determining the form of the stability function ϕ_m (i.e. quantifying

the relationship between wind speed shear and turbulence) becomes more difficult in stable stratification. Weak turbulence can lead to large scatter in the observations, and the influence of local mechanisms (e.g. gravity waves) can influence the relationship (Van de Wiel et al., 2002; Mahrt, 2014). Therefore, values of ϕ_m tend to differ across different field experiments under stable conditions (Sect. 2.4.3). Conversely, in unstable conditions where turbulence is strong, the form of ϕ_m is unambiguous and robustly characterized.

Finally, in stable conditions the Coriolis force becomes non-negligible at low altitudes. This force results in substantial rotation of the wind vector with altitude, which allows for local maxima in the wind profiles at low altitudes (Stull, 1988). Such rotation becomes another confounding factor for IBLs and determining z_0, since turbulence at higher altitudes is characteristic of upstream roughness in a different direction than at lower altitudes. The Coriolis force also causes inertial oscillations, which have considerable influence on the wind speed profile in very stable conditions. In particular, inertial oscillations often lead to the formation of low-level jets (LLJs) with influence extending below 200 m under certain conditions (e.g. low wind speeds and low regional roughness) (Baas et al., 2009; Van de Wiel et al., 2010; Banta et al., 2013). As noted above, turbulent fluxes in conditions of extreme stability become so weak and intermittent above a very shallow SL that winds aloft can decouple from the surface. Under this regime of 'z-less stratification', the turbulent flux and intensity become localized and are no longer affected by the distance from the surface, making the surface-based mixing length $l_m = \kappa z \phi_m^{-1}$ assumed by MOST an inappropriate turbulent length scale (Nieuwstadt, 1984; Mahrt, 1999; Mahrt and Vickers, 2006; Sorbjan and Grachev, 2010). Baroclinicity can also influence wind speed shear and momentum mixing across all stabilities, while gravity waves become influential under extreme stability (Mahrt, 1999; Mahrt and Vickers, 2006).

2.1.4 Intent and Overview of Study

The intent of this study is to demonstrate in detail the limitations of the logarithmic wind speed model as a tool for extrapolating wind speeds, and in particular how these limitations become more restrictive under increasing stable stratification. Data sources are described in Sect. 2.2. In Sect. 2.3, we first demonstrate the uncertainty associated with different characterizations of z_0 and the inaccuracy of surface flux-based extrapolations in the presence of internal boundary layers (IBLs). We then

explore several modifications intended to reduce uncertainty and improve accuracy, including the elimination of z_0 as a required parameter and the determination of a 'bulk' Obukhov length based on wind speed and temperature measurements at different altitudes rather than on surface fluxes. In Sect. 2.4, we address the limitations of the logarithmic wind speed model when applied above the SL. First, we quantitatively examine the role of the Coriolis force above the SL, in particular the rotation of the wind vector with altitude, and examine the degree of decoupling of surface winds from those aloft in increasing stratification. We then compare different forms of the stability function ϕ_m and explore the sensitivity of wind speed profiles to the choice of ϕ_m. In Sect. 2.5, we explore modifications to the logarithmic wind speed model that are intended to extend its range of application above the SL. A discussion is provided in Sect. 2.6, and conclusions in Sect. 2.7. While this analysis considers data from a single location, the factors resulting in the limitations of MOST (IBLs, uncertain estimates of z_0 and ϕ_m, shallow SLs, and the influence of wind vector rotation) are generic.

2.2 Data Sources

This study makes use of data obtained from the Cabauw Meteorological Tower in the Netherlands, operated by the Royal Netherlands Meteorological Institute (KNMI). Measurements of meteorological variables at 10-min resolution were obtained from January 1 2001 to December 31 2010 (these data are available at http://www.cesar-database.nl). Wind speed and direction measurements are made at 10 m, 20 m, 40 m, 80 m, 140 m, and 200 m, and temperature measurements are made at these altitudes as well as 2 m. Surface pressure measurements are also provided, which are used to calculate the potential temperature at different heights. Turbulent momentum and temperature flux measurements made at altitudes of 5 m, 60 m, 100 m and 180 m are provided by KNMI for the period July 1 2007 to June 30 2008. Surface geostrophic wind components at 1-hr resolution derived from surface pressure measurements in the vicinity of Cabauw are provided by KNMI and are linearly interpolated to 10-min resolution. Observations for which 200 m wind speeds are less than 5 m s^{-1} are excluded from the analysis (representing 22 % of the data). Under these conditions, the flux-gradient relationships are known to perform poorly (Mahrt, 1998). Furthermore, low wind speed conditions are not of interest for wind energy applications, so the accuracy of different wind speed profile models under these conditions is not relevant

in the present context. Throughout this analysis, we consider several stability classes based on the bulk Richardson number measured between 200 m and the surface (Table 2.1),

$$Ri_B = \frac{g}{\theta_{avg}} \frac{z_{200}(\theta_{200} - \theta_{surf})}{U_{200}^2} \tag{2.5}$$

where θ_{avg} is the average potential temperature in the lower 200 m. The Ri_B value provides a measure of dynamic stability and is therefore more appropriate than other stability measures such as $\Delta\theta$, which is a measure of only static stability.

Stability class	Ri_B range
Unstable	$Ri_B < -0.02$
Neutral	$-0.02 \leq Ri_B < 0.02$
Weakly stable	$0.02 \leq Ri_B < 0.05$
Moderately stable	$0.05 \leq Ri_B < 0.15$
Very stable	$0.15 \leq Ri_B < 0.5$
Extremely stable	$Ri_B \geq 0.5$

Table 2.1: Stability class ranges used throughout this analysis based on the bulk Richardson number between 200 m and the surface.

2.3 Limitations in inhomogeneous terrain

In this section, we explore the uncertainty and inaccuracy associated with applying the logarithmic wind speed model in inhomogeneous surface roughness conditions.

2.3.1 Uncertainty in z_0 and internal boundary layers

The logarithmic wind speed profile is subject to considerable uncertainty as a result of difficulty in estimating z_0. The value of z_0 at a given location is generally categorized in 5-30° wind direction segments. Verkaik and Holtslag (2007) have determined z_0 at Cabauw using the various methods described in Table 2.2 and illustrated in Fig. 2.2. Local and mesoscale land-use based z_0 values were not published in Verkaik and

Holtslag (2007), but are provided directly by KNMI. As shown in Fig. 2.2, z_0 can vary substantially between different formulations, sometimes by one or more orders of magnitude for the same wind direction (e.g. between 230° and 250°). If MOST was perfectly valid and turbulent fluxes were constant across the different measurement altitudes used to determine z_0 in Fig. 2.2, we would expect similar values of z_0 across different formulations. Indeed, we would expect identical z_0 values when the same approach is used with information from different altitudes (e.g. Profile 10-40 m and Profile 10-200 m). The large differences between z_0 formulations observed in Fig. 2.2 indicate that MOST is not perfectly valid at Cabauw, due in part to the inhomogeneity in the surrounding surface roughness. The immediate surroundings at Cabauw (within 200 m) have relatively low roughness, while further from the tower (within 1-2 km) roughness increases significantly due to the presence of small towns and belts of trees (Verkaik and Holtslag, 2007). Since the z_0 formulations considered in Fig. 2.2 are determined over a range of altitudes, they capture upstream roughness features over a range of distances from Cabauw (e.g. 100-m drag method captures features farther upstream than 20-m drag method). Likewise, local land-use values of z_0 are more representative of turbulence at lower altitudes, while regional land-use values are more representative at higher altitudes.

The low local roughness and high regional roughness at Cabauw result in a specific IBL structure. We demonstrate this structure using 1 year of turbulent flux profile data at Cabauw (Fig. 2.3). For horizontally homogeneous surface roughness, we would expect nearly equal momentum fluxes between 5 m and 60 m for unstable and neutral conditions, and larger flux magnitudes at 5 m for stable conditions compared to those at 60 m. However, Fig. 2.3(a) demonstrates that the near-surface turbulent momentum fluxes are lower in magnitude relative to those aloft across all stability classes, and is therefore indicative of the influence of IBLs and not of an "upside-down" boundary layer in which turbulent fluxes increase with altitude, sometimes seen in very stable stratification (e.g. Mahrt, 2014). Temperature flux profiles are generally less affected by surface roughness-generated IBLs (Bosveld, 2015), which is evident in Fig. 2.3(b). Lower momentum fluxes at 5 m result in larger magnitudes of $|L^{-1}|$ at 5 m (Fig. 2.3 (c)) which are indicative of a more unstable near-surface layer in unstable conditions and a more stable near-surface layer in stable conditions, relative to the flow aloft.

We now examine the sensitivity of the logarithmic wind speed model to these different z_0 formulations and the IBL structure at Cabauw. For this analysis we

Formulation	Abbreviation	Description
Land-use maps	LU	Land-use maps characterize the surrounding terrain into different roughness length categories. In inhomogeneous terrain, z_0 values can vary significantly for a given wind direction, and are often categorized as 'local' (e.g. within 1 km radius) or 'regional' (e.g. outside 1 km radius) (Troen and Petersen, 1989; Petersen et al., 1998)
Standard deviation to mean wind speed ratio	Std/Mean	The friction velocity is found to be strongly related to the standard deviation of the horizontal wind speed at 10 m, σ_U. Beljaars (1987) found that $\sigma_U/u_* \approx 2.2$ for neutral conditions, which is used to compute z_0 from the neutral logarithmic wind speed equation (Beljaars, 1987; Verkaik and Holtslag, 2007)
Gustiness	Gustiness	In cases where high resolution measurements of σ_U cannot be made, the peak gustiness ($U_{max} - \bar{U}$) measured over several short time intervals (e.g. 10 min) can be averaged to estimate σ_U (Beljaars, 1987; Verkaik and Holtslag, 2007).
Profile	Prof	Observed wind speed profiles are extrapolated to $\bar{U}(z_0) = 0$, from which z_0 can be determined from the logarithmic wind speed equation (Nieuwstadt, 1978; Verkaik and Holtslag, 2007).
Drag coefficient	Drag	The drag coefficient $C_d = (u_*/\bar{U})^2$ can be determined at a particular height, where u_* is measured or diagnosed. The roughness length can then be computed using the logarithmic wind speed equation (Verkaik and Holtslag, 2007).

Table 2.2: Description of different z_0 formulations, along with abbreviations used in this study.

Stability function	Range of applicability	Reference	Abbreviation
$\phi_m = 1 + \beta\zeta$	$\zeta > 0$	Businger et al. (1971)	B71
$\phi_m = 1 + \beta\zeta$ $\phi_m = 1 + \beta$	$0 \leq \zeta \leq 1$ $\zeta > 1$	Webb (1970)	W70
$\phi_m = 1 + \beta\zeta$ $\phi_m = 8 - 4.25\zeta^{-1} + \zeta^{-2}$ $\phi_m = 0.76\zeta$	$0 \leq \zeta \leq 0.5$ $0.5 \leq \zeta < 10$ $\zeta \geq 10$	Hicks (1976)	H76
$\phi_m = (1 + \beta\zeta)\left[1 + 0.0079\zeta(1 + \beta\zeta)\right]^{-1}$ $\phi_m = (1 + \beta)[1 + 0.0079(1 + \beta)]^{-1}$	$0 \leq \zeta \leq 1$ $\zeta > 1$	Clarke (1970)	C70
$\phi_m = 1 + a\zeta + b\zeta(1 + c - d\zeta)\exp(-d\zeta)$ $a = 1, b = 2/3, c = 5, d = 0.35$	$0 \leq \zeta \leq 10$	Beljaars and Holtslag (1991)	BH91
$\phi_m = 1 + e\left[\zeta + \zeta^f(1 + \zeta^f)^{(1-f)/f}\right]\left[\zeta + (1 + \zeta^f)^{1/f}\right]^{-1}$ $e = 6.1, f = 2.5$	$\zeta > 0$	Cheng and Brutsaert (2005)	C05

Table 2.3: Different stability function formulations considered in this analysis and their range of application, where $\zeta = z/L$.

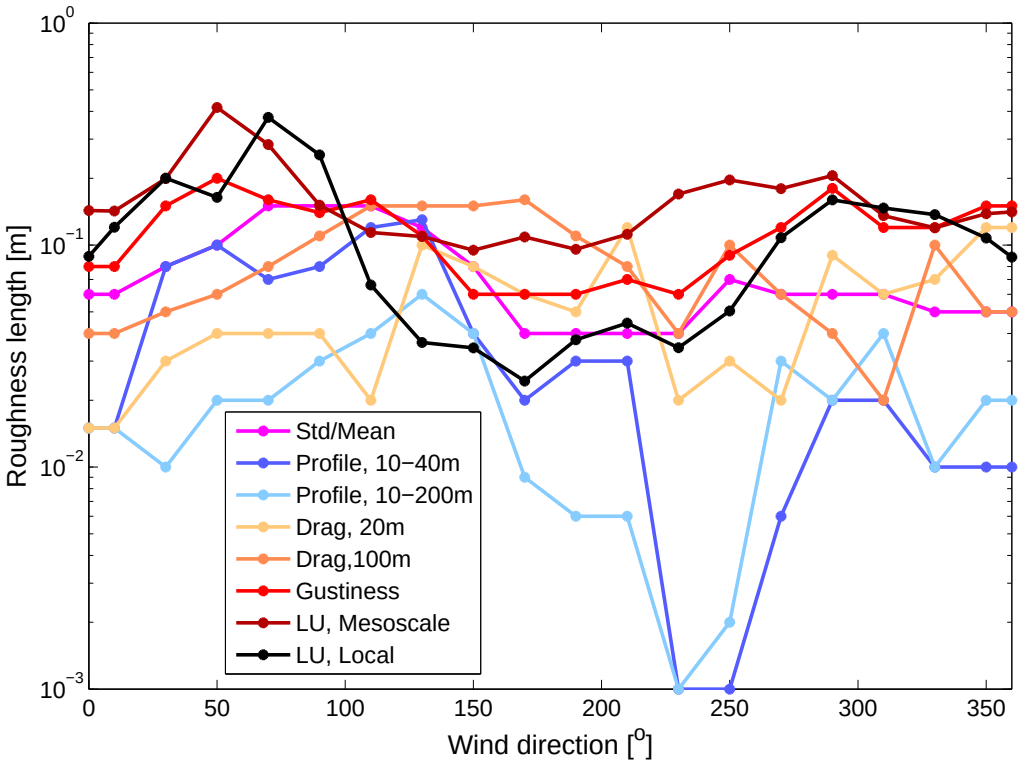

Figure 2.2: Mean roughness length by wind direction for various formulations at Cabauw, based on data from Verkaik and Holtslag (2007) and KNMI.

consider unstable through weakly stable conditions and heights up to 80 m. These criteria ensure that observations are largely limited within the SL or just above it and also minimize the variability associated with different stability function formulations, which diverge considerably in strongly stable conditions (Sect. 2.4.3). We extrapolate 10 m wind speeds up to 80 m using the different z_0 formulations through the ratio of the logarithmic wind speed equation at 10 m and at the alitude z:

$$\bar{U}(z) = \bar{U}_{10} \frac{\left[\ln\left(\frac{z}{z_0}\right) - \psi_m\left(\frac{z}{L}, \frac{z_0}{L}\right)\right]}{\left[\ln\left(\frac{10}{z_0}\right) - \psi_m\left(\frac{10}{L}, \frac{z_0}{L}\right)\right]} \tag{2.6}$$

We use the Beljaars and Holtslag (1991) form of ψ_m (Table 2.3) in Eq. 2.6 for $L > 0$, as this form was determined based on Cabauw data. We use the well-known and widely-accepted Dyer and Hicks (1970) form of ψ_m for $L < 0$,

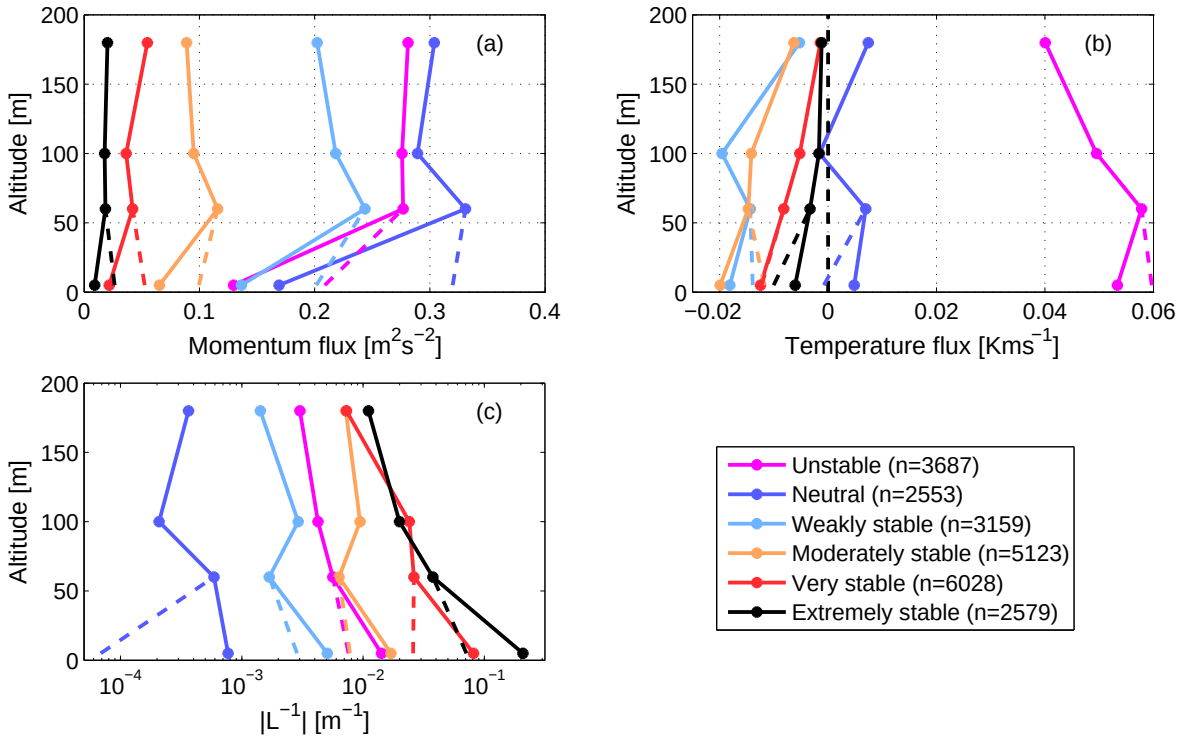

Figure 2.3: Vertical profiles of: (a) mean turbulent momentum flux, (b) mean turbulent temperature flux, and (c) median $|L^{-1}|$ for a range of stability classes. Bold lines denote flux-measured values, while the dotted lines connect to surface bulk values computed from Eq. 2.13 using measurements at 20 m and 10 m.

$$\psi_M(\zeta) = \frac{\pi}{2} - 2\arctan(x) + \log\frac{(1+x)^2(1+x^2)}{8}, \tag{2.7}$$

where $x = (1-16z/L)^{1/4}$. The range of mean wind speed profiles across different z_0 formulations is considerable (Fig. 2.4). The range is smallest in unstable conditions and largest in weakly stable conditions, due to the higher sensitivity of Eq. 2.6 to changes in z_0 when $\psi_m < 0$ (i.e. stable), and lower sensitivity when $\psi_m > 0$ (i.e. unstable). Furthermore, the modelled wind speed profiles are generally evenly distributed around the observed profile in unstable conditions and generally have larger magnitude in neutral and weakly stable conditions. This apparent shift of the modelled profiles in relation to stability is a consequence of the local IBL at Cabauw. The use of a surface flux-derived Obukhov length in the logarithmic wind speed model over-corrects for stability at Cabauw, resulting in underestimates of wind speeds aloft

in unstable conditions (not clearly evident in Fig. 2.4(a)) and overestimates in stable conditions (clearly evident in Fig. 2.4(c)). By contrast, had the local roughness been *higher* than the regional roughness, then the wind speed profiles would have *under-corrected* for stability and opposite shifts to those in Fig. 2.4 would have been observed.

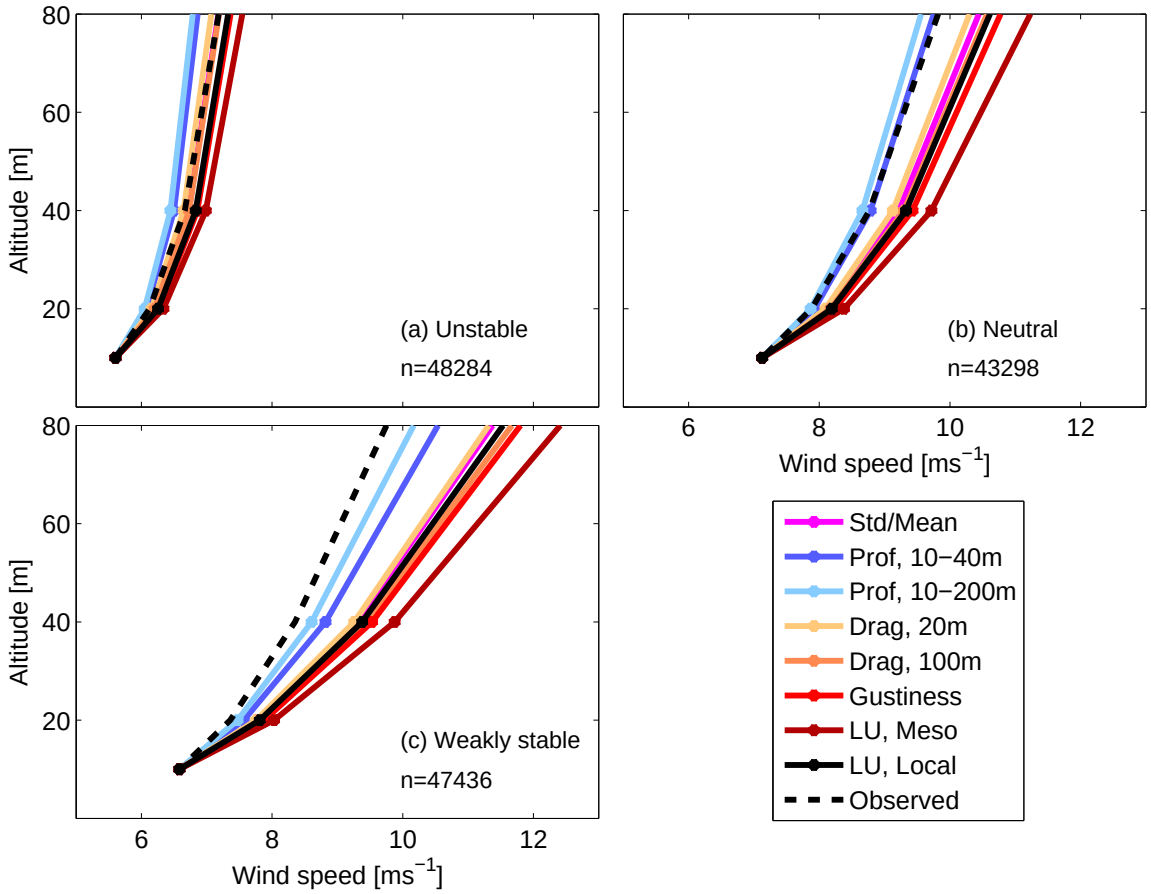

Figure 2.4: Modelled and observed mean wind speed profiles for (a) unstable, (b) neutral, and (c) weakly stable conditions over a range of z_0 formulations. In each plot, n denotes the number of profiles in the mean.

2.3.2 Correcting for IBLs and z_0 variability with a 'bulk' Obukhov length

An alternative approach to determining L which can mitigate the influence of IBLs involves using wind speed and temperature measurements at one or more altitudes

in place of turbulent flux measurements (e.g. De Bruin et al., 2000). Specifically, the 'bulk' Obukhov length is derived from the bulk Richardson number, Ri_B, between two altitudes, z_2 and z_1 ,

$$Ri_B = \frac{g}{\theta_{avg}} \frac{\Delta\theta/\Delta z}{(\Delta U/\Delta z)^2} = \frac{g}{\theta_{avg}} (z_2 - z_1) \frac{\theta(z_2) - \theta(z_1)}{[U(z_2) - U(z_1)]^2} \tag{2.8}$$

where θ_{avg} is the mean potential temperature between z_2 and z_1, and $z_2 > z_1$. To determine the related Obukhov length, we use the MOST-based profiles for wind speed and temperature between altitudes z_2 and z_1,

$$\bar{U}(z_2) - \bar{U}(z_1) = \frac{u_*}{\kappa} \left[\ln\left(\frac{z_2}{z_1}\right) - \psi_m\left(\frac{z_2}{L}, \frac{z_1}{L}\right) \right], \tag{2.9}$$

$$\bar{\theta}(z_2) - \bar{\theta}(z_1) = \frac{-(\overline{w'\theta'})_s}{\kappa u_*} \left[\ln\left(\frac{z_2}{z_1}\right) - \psi_h\left(\frac{z_2}{L}, \frac{z_1}{L}\right) \right] \tag{2.10}$$

where ψ_h is the stability function for heat. For $L > 0$, we use the Beljaars and Holtslag (1991) form based on Cabauw data,

$$\psi_h = -\left(1 + \frac{2}{3}a\frac{z}{L}\right)^{3/2} + \left(1 + \frac{2}{3}a\frac{z_0}{L}\right)^{3/2} - b\left(\frac{z}{L} - \frac{c}{d}\right)\exp\left(-d\frac{z}{L}\right) + b\left(\frac{z_0}{L} - \frac{c}{d}\right)\exp\left(-d\frac{z_0}{L}\right) \tag{2.11}$$

For $L < 0$, we use the well-known and widely accepted Dyer and Hicks (1970) form,

$$\psi_h = 2\log\left(\frac{1 + x^2}{2}\right) \tag{2.12}$$

Combining Eqs. 2.9 - 2.10 with Eqs. 2.2 and 2.8 results in an expression relating Ri_B to the bulk Obukhov length between z_2 and z_1,

$$Ri_B = \left(\frac{z_2 - z_1}{L}\right) \frac{\ln\left(\frac{z_2}{z_1}\right) - \psi_h\left(\frac{z_2}{L}, \frac{z_1}{L}\right)}{\left[\ln\left(\frac{z_2}{z_1}\right) - \psi_m\left(\frac{z_2}{L}, \frac{z_1}{L}\right)\right]^2} \tag{2.13}$$

Using Eq. 2.13, the bulk Obukhov length can be computed iteratively given Ri_B.

In the context of correcting for IBLs, this approach is particularly advantageous as altitudes z_2 and z_1 can be selected above the IBL. The resulting value for L would then be more characteristic of upstream roughness and therefore more applicable at higher altitudes than the surface flux-based value. However, there are limitations to this approach. First, this bulk approach assumes the validity of MOST between the measurement altitudes and therefore will break down for higher altitudes and stronger stability. Low near-surface winds under very stable stratification result in very low values of $(\Delta U/\Delta z)^2$ in Eq. 2.5, and consequently very low bulk values of L. Second, setting the lower boundary at the surface (i.e. $z_1 = z_0$) results in large uncertainty, given the difficulty in measuring the value of the roughness length for temperature, z_{0h} (i.e. the height at which the air temperature is equal to the surface temperature). The value of z_{0h} has been observed to be at least one order of magnitude less than z_0 (e.g. Kou-Fang Lo, 1996; van den Hurk and Holtslag, 1997). Therefore, z_1 should be set at some height above the surface where temperature measurements are made (e.g. 2 m). Finally, the bulk approach breaks down when the difference in observations between two altitudes is small or comparable to the measurement uncertainty (e.g. 0.1 K for temperature measurements). Therefore, the bulk approach should only be applied within an altitude range where sufficiently large wind and temperature gradients exist (e.g. close to the surface).

In the context of correcting for the IBL at Cabauw when extrapolating surface wind speeds up to 80 m, we require values of L that are closer to neutral compared to the flux-derived value at 5 m. We explore bulk values of L determined between a range of altitudes at Cabauw in Fig. 2.5 using probability density functions (PDFs) of $|L|$, separately considering cases where $L < 0$ and $L > 0$. We compute 2-m wind speeds based on logarithmic interpolation between 10 m and z_0 and note that the absence of direct observations of wind speed at 2 m means that z_0 must still enter the calculation when $z_1 = 2$ m. We consider two end members of the z_0 formulations: 'Land-use, mesoscale' (highest roughness) and 'Profile 10-200m' (lowest roughness). When winds and temperature are both available at z_1 (as when $z_1 = 10$ m), z_0 and its associated uncertainty do not enter the calculation.

As seen in Fig. 2.5, distributions of bulk values of $|L|$ are generally shifted to larger values (i.e. more neutral characterization) than that of the 5-m flux-derived values. We attribute this result to the fact that all z_0 formulations considered (which are measured at 10 m or higher) are more representative of upstream roughness elements and therefore larger than z_0 values at the surface flux altitude (i.e. 5 m), which would

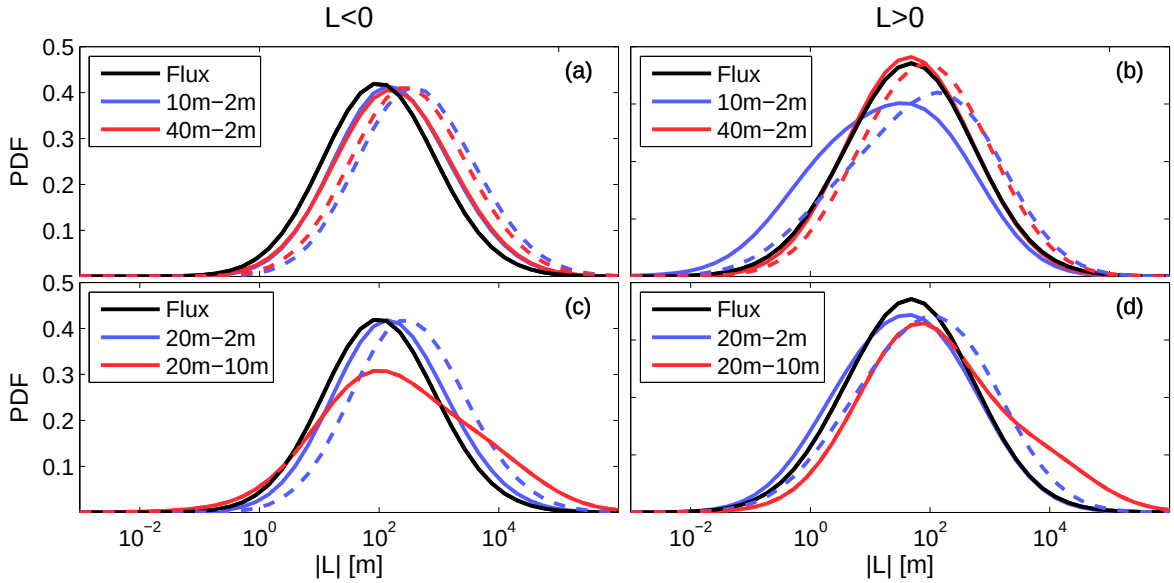

Figure 2.5: Probability density functions of $|L|$, for 5-m flux-derived values as well as bulk-derived values evaluated between different heights. Different columns separate cases where $L < 0$ (left) and $L > 0$ (right), and different rows separate cases where z_2 is varied (top) and z_1 is varied (bottom). In cases where $z_1 = 2$ m, solid lines correspond to the 'Profile, 10-200m' formulation of z_0, while dotted lines correspond to the 'Land-use, mesoscale' formulation.

reflect roughness features in the immediate vicinity (i.e. 50 m) of the tower. We also observe that higher values of z_0 are associated with considerably higher bulk values of $|L|$. We can use PDFs of bulk $|L|$ values to deduce information about the height of the local IBL in different stability conditions. In particular, we observe that bulk $|L|$ values derived between 10-2 m and 40-2 m (i.e. $|L_{10-2}|$, $|L_{40-2}|$) for $L < 0$ are nearly identical (Fig. 2.5 (a)). This approximately constant value of $|L|$ between 10 m and 40 m is indicative of a SL up to 40 m and provides evidence of a local IBL height at Cabauw generally above 40 m in unstable conditions. Conversely, for $L > 0$, we observe that the distribution of $|L_{10-2}|$ values are generally smaller (i.e. more stable characterization) than those of $|L_{40-2}|$ for low values of $|L|$ (Fig. 2.5 (b)). This result indicates a local IBL height generally between 10 m and 40 m in stable conditions. Finally, we observe that the distribution of bulk $|L|$ values measured between 20m-10m (i.e. $|L_{20-10}|$) are generally lower for $L < 0$ for low values of $|L|$, which we attribute to the tendency of the bulk approach to overestimate the magnitude of stability when $U_{20} - U_{10}$ is small. In addition, we see large shifts in the distributions

towards high values of $|L|$, which may be attributed to the measurement uncertainty for low $\Delta\theta$ values which may often lead to underestimates of $\Delta\theta$ (and therefore large $|L|$ values). Neutral conditions exist for $|L| > 500$ m, so these large shifts simply characterize 'more neutral' conditions and have negligible influence in wind profile extrapolation.

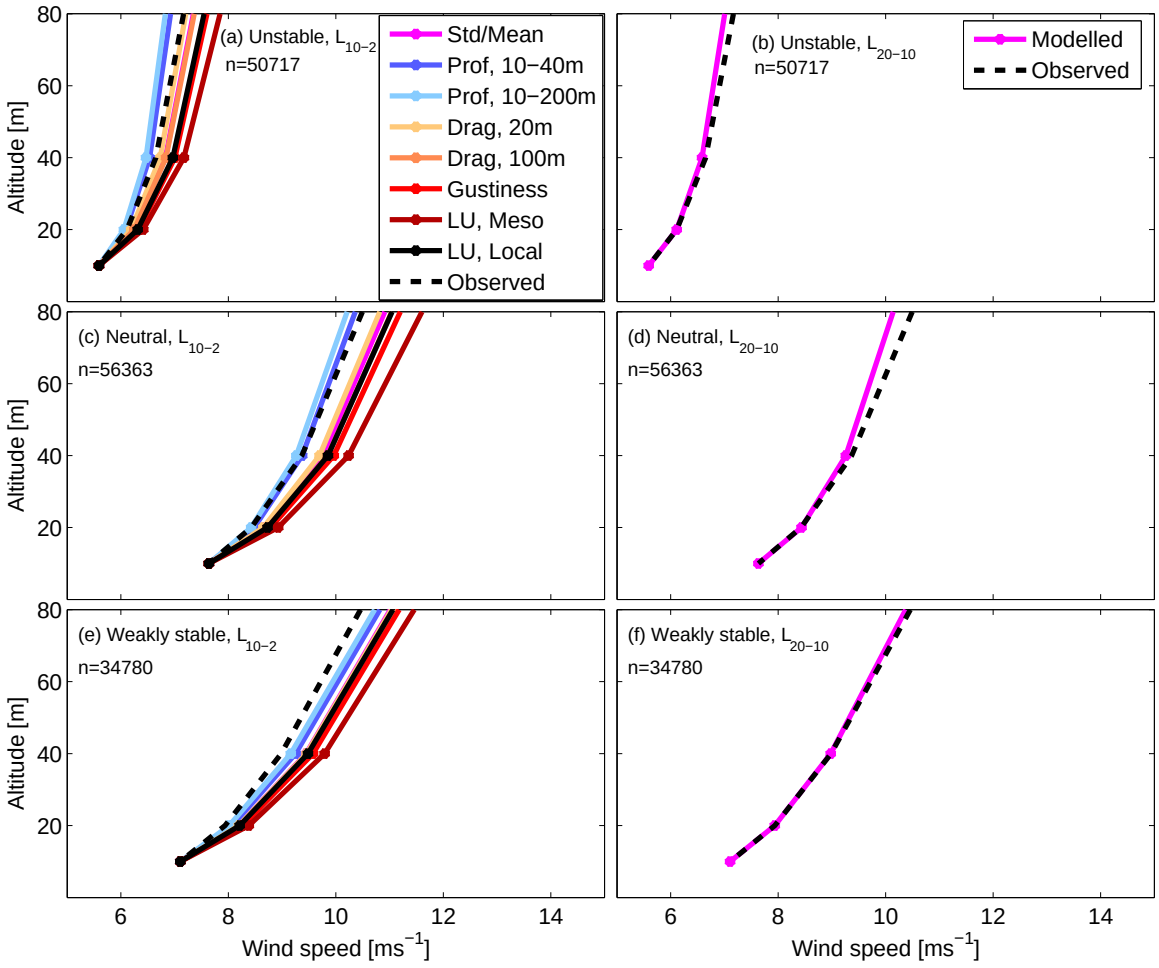

Figure 2.6: Mean modelled and observed wind speed profiles for (a) unstable, (b) neutral, and (c) weakly stable conditions. Modelled profiles are based on different bulk values of L and a range of z_0 formulations.

In Fig. 2.6, we explore the sensitivity of extrapolated wind speed profiles to two different bulk L formulations: L_{10-2} and L_{20-10}. We extrapolate 10 m wind speeds up to 80 m using Eq. 2.6 for the L_{10-2} case. For the L_{20-10} case, which does not require the specification of z_0, we use Eq. 2.9 with $z_1 = 10$ m (note that the u_* term in Eq.

2.9 is calculated using $z_2 = 20$ m and $z_1 = 10$ m). The modelled profiles using L_{10-2} are not substantially different compared to the use of flux-derived values of L (Fig. 2.4) although the 'Profile' approaches generally demonstrate higher accuracy across all stability classes compared to other z_0 approaches. This result is not surprising given that z_0 values for the 'Profile' approach were determined based on fitting a logarithmic wind speed profile to observations. The modelled profiles using L_{20-10} show strong agreement with observations on average, apart from a modest tendency to underestimate wind speeds above 100 m in unstable and neutral conditions, which we attribute to the tendency of the bulk approach to overestimate the magnitude of stability when $U_{20} - U_{10}$ is small.

Overall, both bulk approaches provide some correction for IBLs at Cabauw and provide an improvement in extrapolated wind speeds compared to the surface flux approach. The absence of a need to specify z_0 in the L_{20-10} approach is a considerable advantage and eliminates a key uncertainty in the logarithmic wind speed profile at the expense of requiring observations of wind speeds and temperature at two different altitudes.

Finally, we determine bulk values of u_* and $(\overline{w'\theta'})_s$ from L_{20-10} using Eqs. 2.9 - 2.10 and plot these values at the surface along with the flux profiles in Fig. 2.3. As seen in the figure, the bulk values are generally much closer to the 60 m values than the 5-m flux values (particularly the $|L^{-1}|$ profiles) as would be expected in horizontally homogeneous conditions, so the bulk approach has compensated for the presence of IBLs at Cabauw. Given this improved stability characterization of L_{20-10} compared to the surface flux-derived values and the reduction of uncertainties resulting from avoiding the need to specify a value of z_0, the L_{20-10} values will be used for wind profile extrapolation in the remainder of this study.

2.4 Breakdown of Monin-Obukhov similarity theory above the surface layer

Having demonstrated the limitations of MOST in inhomogeneous terrain, we now turn to the breakdown of MOST when extended above the surface layer.

2.4.1 Role of Coriolis force

As discussed in Sect. 2.1.3, the influence of the Coriolis force on the wind speed profile is non-negligible under conditions of weak turbulent mixing. This force leads to the rotation of the wind vector with altitude which allows a local maximum in the wind speed profile. We demonstrate this rotation in Fig. 2.7, where the mean of the angles between the 10 m winds and those aloft are shown for the different stability classes. As demonstrated in Fig. 2.7, the rotation of the wind vector increases with stability, which results from the increased influence of the Coriolis force at increasing distances above the SL (see Fig. 2.1). In extremely stable conditions the rotation is on average greater than 45° between 10 m and 200 m, compared to less than 5° in unstable conditions. As discussed in Sect. 2.1.2, h_{SL} may effectively be defined as the layer near the surface in which the rotation of the wind vector with altitude is minimal. We can use this fact and the results of Fig. 2.7 to deduce the mean height of the SL for the different stability classes. If we take h_{SL} as the height at which the wind vector rotation is 3°, we obtain $h_{SL} \simeq 200$ m for unstable conditions, $h_{SL} \simeq 140$ m for neutral conditions, $h_{SL} \simeq 70$ m for weakly stable conditions, $h_{SL} \simeq 40$ m for moderately stable conditions, $h_{SL} \simeq 20$ m for very stable conditions, and $h_{SL} < 20$ m for extremely stable conditions.

Furthermore, the Coriolis force also has a time-dependent influence, causing inertial oscillations and LLJs with amplitudes that become larger with weakening turbulence. At the Cabauw site, LLJs caused by inertial oscillations are a frequent phenomena, as demonstrated in detail in Baas et al. (2009). Under the influence of the Coriolis force above the SL, the wind speed profile in this region is generally not described by the logarithmic profile, and similarity-based profiles such as MOST are no longer representative of the flow.

2.4.2 Surface decoupling

With weak turbulent mixing, the validity of surface-based extrapolations becomes more limited. As discussed in Sect. 2.1.3, reduced turbulent mixing increases the time required for a turbulence signal at the surface to be propagated upwards. In extreme cases, the collapse of turbulence can lead to surface decoupling from the winds aloft (Mahrt, 1999, 2014). We demonstrate the degree of decoupling for the different stability classes by considering the square of the linear correlation coefficients between wind speeds at 10 m and those aloft (Fig. 2.8). In general, correlations are strong

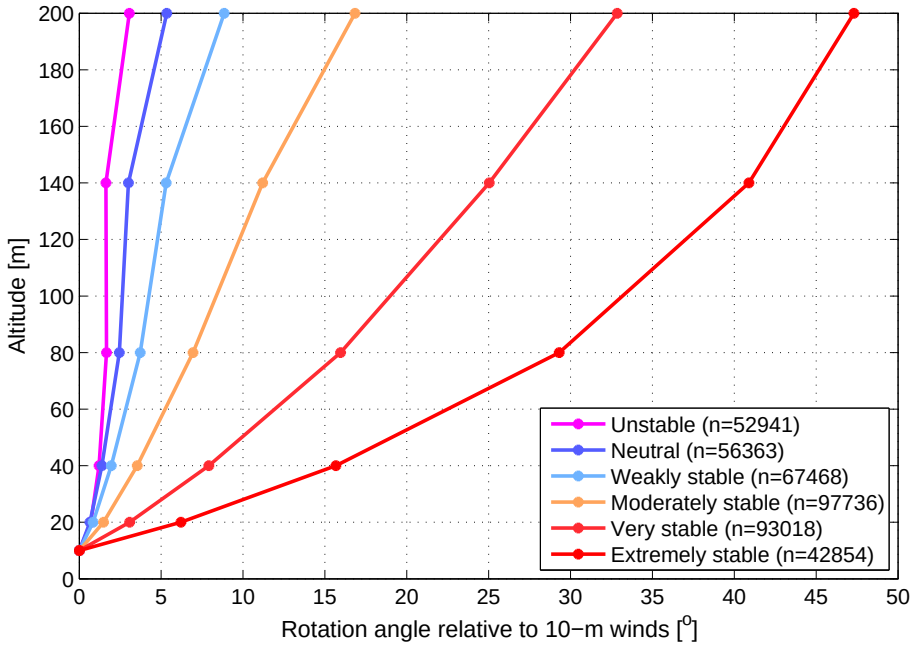

Figure 2.7: Mean rotation of the wind vector relative to 10-m winds under different stability classes.

at low altitudes and low stability ranges, corresponding to the effective transport of turbulence between the two altitudes. Correlations are weak at high altitudes and high stability ranges, corresponding to less effective transport of turbulence. In particular, the wind speeds between 10-200 m and 10-140 m show relatively weak correlation in very and extremely stable conditions, indicative of weak coupling. The performance of any entirely surface-based extrapolation (temperature, humidity, etc.) is expected to be limited by this weak coupling.

2.4.3 Applying the logarithmic wind speed model above the surface layer

Having demonstrated the factors resulting in the limitations of MOST above the SL, we now examine the accuracy of the logarithmic wind speed model in this regime.

We first consider the uncertainty associated with different forms of the stability function, ϕ_m. The original formulation of $\phi_m = 1 + \beta z/L$ under stable stratification (Businger et al., 1971) was based on the concept of 'z-less stratification': if the height

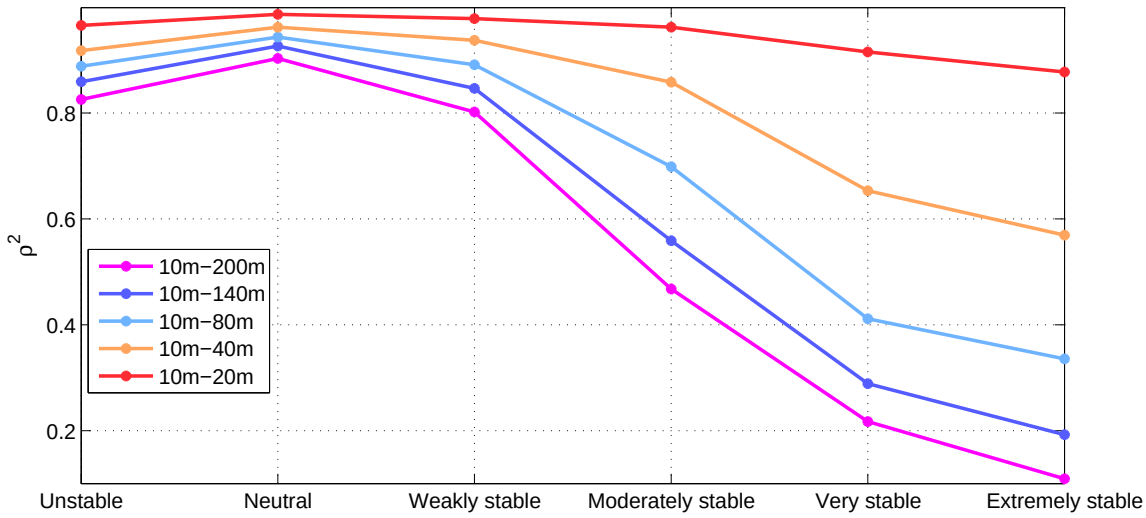

Figure 2.8: Square of the linear correlation coefficient between 10-min averaged 10-m wind speeds and those aloft for different stability classes. Bin sizes by stability classe are the same as those shown in Fig. 2.7.

above the surface ceases to be a valid scaling parameter in very to extremely stable conditions, then according to Eq. 2.1 the stability function should take the form $\phi_m \simeq \beta z/L$ (Webb, 1970). The quantity β is an empirical constant determined from field experiments in the SL over relatively flat, homogeneous terrain. A linear interpolation of this 'z-less' case and the neutral case ($\phi_m = 1$) leads to $\phi_m = 1+\beta z/L$, with $\beta \approx 5$ a commonly used value (Webb, 1970).

Subsequent field studies across a broader range of experimental conditions indicated that ϕ_m increased more slowly for $z/L > 1$ than indicated in the Businger et al. (1971) formulation. These studies have lead to a range of proposed alternative forms of the stability function designed to be applicable for $z/L > 1$ (Sharan and Aditi, 2009). These functions are summarized in Table 2.3 and plotted in Fig. 2.9 along with the associated ψ_m. Also plotted in Fig. 2.9 are the forms of ϕ_m and ψ_m for unstable conditions using the well-known and widely-accepted form of Dyer and Hicks (1970),

$$\phi_m = \left(1 - 16\frac{z}{L}\right)^{-1/4} \tag{2.14}$$

which when integrated leads to Eq. 2.7.

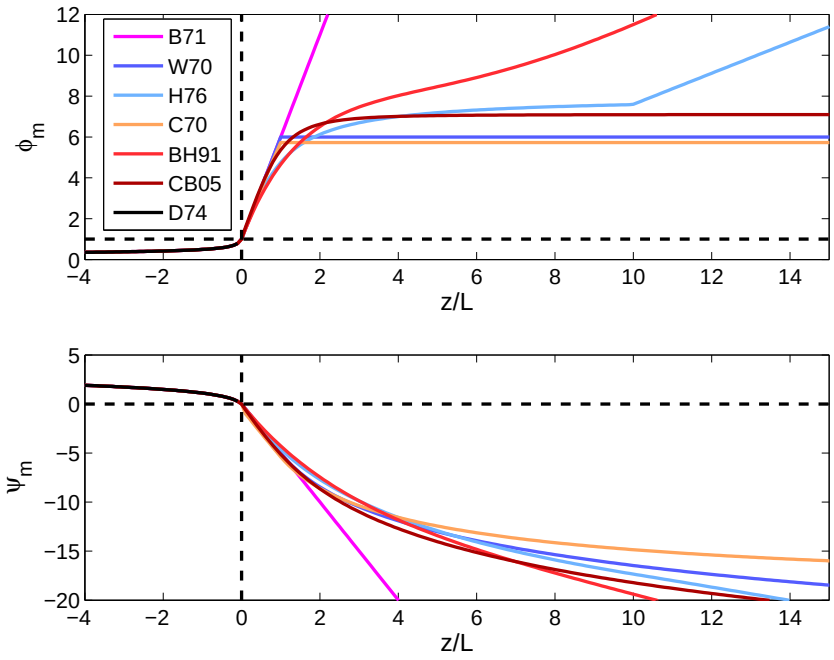

Figure 2.9: Different proposed forms of ϕ_m and ψ_m (Table 2.3) as functions of z/L

As shown in Fig. 2.9, the different forms of ϕ_m and ψ_m are nearly equivalent for $0 < z/L < 0.5$. Beyond this range, considerable divergence is observed. Some forms recover the 'z-less' limit at high values of z/L although with smaller slope than the standard linear form, while other formulations approach a constant value. This divergence can be explained in part by the weak and intermittent turbulence observed in such conditions and the increased influence of a range of local processes (e.g. gravity waves) particular to each measurement location (Mahrt, 1998). The divergence can also be explained in part by differences between studies in the way these functions are estimated (Van de Wiel et al., 2002).

We explore the sensitivity of the logarithmic wind speed profile to different forms of ψ_m for stable conditions at Cabauw (Fig. 2.10). Here we use the L_{20-10} bulk value and extrapolate 10-m wind speeds up to 200 m using Eq. 2.9 with $z_1 = 10$ m. As seen in the figure, the modelled profiles (apart from the Businger et al. (1971) model) are accurate in weakly stable conditions and up to 80 m in moderately stable conditions. The modelled profiles diverge above these altitudes with increasing stability,

especially the original Businger et al. (1971) formulation. Such divergence provides clear evidence of the non-universality of MOST under conditions of strong stability. In fact, different stability functions will be more accurate at different locations for $z/L > 0.5$. The Beljaars and Holtslag (1991) and Cheng and Brutsaert (2005) forms provide the most accurate results at Cabauw in very to extremely stable conditions. The performance of the Beljaars and Holtslag (1991) model is not surprising given that it was based on Cabauw observations. We observe further in Fig. 2.10 that the altitudes at which the Businger et al. (1971) profile begins to diverge from the observations corresponds reasonably well with the SL heights determined in Sect. 2.4.1 (i.e. 80 m, 50 m, 20 m, and < 10 m for weakly, moderately, very, and extremely stable conditions, respectively). Indeed, values of $z/L > 1$ are generally above the SL, and we note that the divergence of ϕ_m is strongly associated with the application of MOST above the SL.

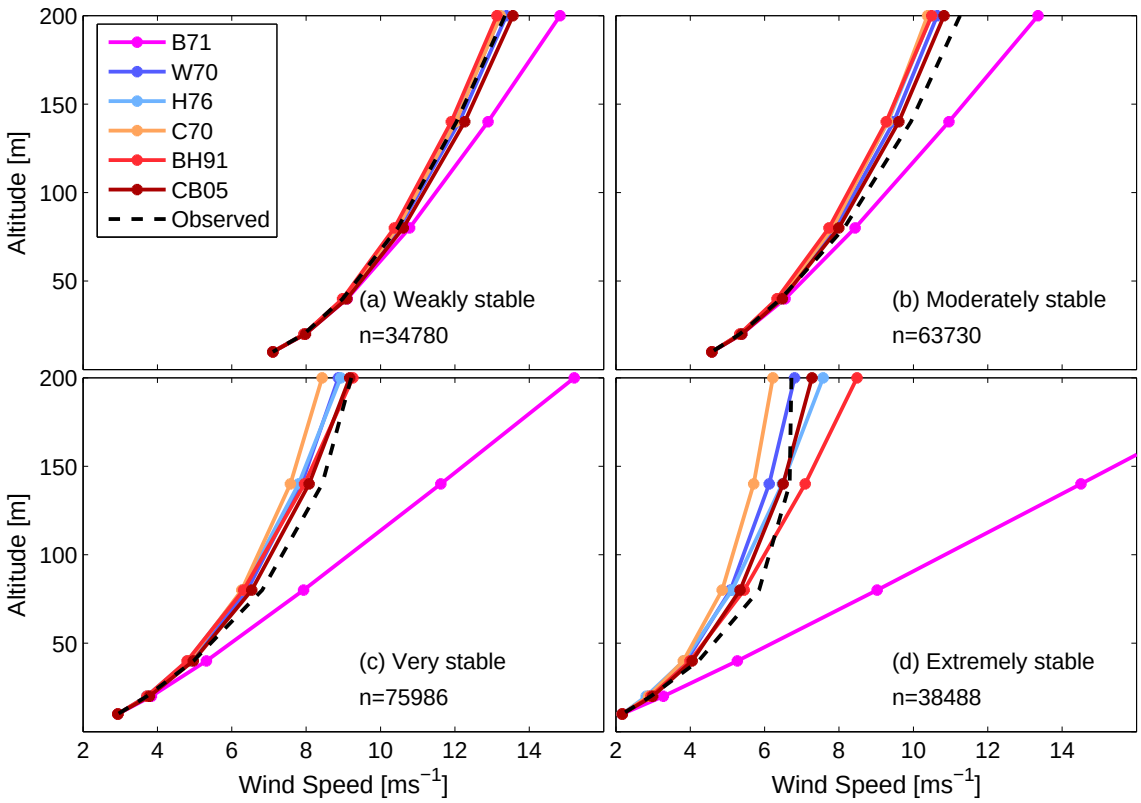

Figure 2.10: Extrapolation of 10-m wind speeds up to 200 m using the logarithmic wind speed profile for different formulations of ψ_m and different regimes of stable stratification.

2.5 Extending the range of application above the surface layer

In the previous section, we demonstrated the breakdown of MOST when applied above the SL. We now explore modifications of MOST that are intended to extend the range of applicability of the logarithmic wind speed model to the entire ABL.

2.5.1 Gryning model

The breakdown of MOST above the SL was discussed by Gryning et al. (2007), who proposed two modifications intended to extend the applicability of the logarithmic wind speed model across the entire ABL. These modifications have since been adopted in a number of studies (e.g. Gryning and Batchvarova, 2008; Pena et al., 2010; Sathe et al., 2011, 2012; Kumar and Sharan, 2012). The first modification replaces the surface value of the friction velocity (i.e. $u_{*,s}$) in Eq. 2.1 with an altitude-dependent profile, expressed as a linear function of $u_{*,s}$ and the ABL height, h_{ABL} (Panofsky, 1973),

$$u_*(z) = u_{*,s}\left(1 - \frac{z}{h_{ABL}}\right), \tag{2.15}$$

Gryning et al. (2007) used radiosonde observations to determine h_{ABL}, while Pena et al. (2010) used the parameterization suggested by Tennekes (1973),

$$h_{ABL} = C\frac{u_{*,s}}{f} \tag{2.16}$$

In Eq. 2.16, C is a piecewise constant function and f is the Coriolis parameter. Different values of C are used based on the surface Obukhov length (Pena et al., 2010). The second modification replaces the surface layer mixing length $l_m = \kappa z \phi_m^{-1}$ in Eq. 2.1 with a generalized form of the Blackadar (1962) mixing length,

$$l_m(z) = \kappa\left(\frac{\phi_m}{z} + \frac{1}{L_{MBL}} + \frac{1}{h_{ABL} - z}\right)^{-1} \tag{2.17}$$

The first term in Eq. 2.17 results in the standard MOST mixing length for small values

of z. The second term is a mid-boundary-layer mixing length (with $L_{MBL} < h_{ABL}$) that places an upper bound on the magnitude of l_m. The final term results in the mixing length decreasing to zero at the top of the ABL, above which turbulence should normally be negligible. Integrating Eq. 2.1 with these new parameterizations and using the Businger et al. (1971) form $\phi_m = 1 + \beta z/L$, Gryning et al. (2007) derive the following modified equation for stable conditions,

$$\bar{U}(z) = \frac{u_*}{\kappa}\left[\ln\left(\frac{z}{z_0}\right) + \beta\frac{z}{L}\left(1 - \frac{z}{2h_{ABL}}\right) + \frac{z}{L_{MBL}} - \frac{z^2}{2h_{ABL}L_{MBL}}\right]. \tag{2.18}$$

Generalizing the integration between heights z_2 and z_1 results in,

$$\bar{U}(z_2) = \bar{U}(z_1) + \frac{u_*}{\kappa} \left[\ln\left(\frac{z_2}{z_1}\right) + \beta\frac{(z_2 - z_1)}{L}\left(1 - \frac{(z_2 - z_1)}{2h_{ABL}}\right) + \frac{(z_2 - z_1)}{L_{MBL}} - \frac{(z_2^2 - z_1^2)}{2h_{ABL}L_{MBL}}\right]. \tag{2.19}$$

In Gryning et al. (2007), L_{MBL} is estimated by equating $\bar{U}$ at $z = h_{ABL}$ given by Eq. 2.18 with the geostrophic wind as expressed through the geostrophic drag law,

$$G = \frac{u_*}{\kappa}\sqrt{\left[\ln\left(\frac{u_*}{f z_0}\right) - A\right]^2 + B^2}. \tag{2.20}$$

where A and B are piecewise constant functions that depend on the surface Obukhov length (Pena et al., 2010). Results from Gryning et al. (2007) and subsequent studies (e.g. Pena et al., 2010; Emeis, 2013) have demonstrated the ability of the modified model to estimate wind speed profiles within the ABL that are more accurate compared to the standard MOST approach under all stabilities.

The assumptions of the Gryning model constrain its application under conditions of stable stratification. First, this approach assumes that turbulent fluxes decrease monotonically with altitude across the ABL (which may in fact not be the case under conditions of very strong stratification; Mahrt, 2014). Second, as demonstrated in Sect. 2.4.3, the Businger et al. (1971) form of ϕ_m breaks down above $z/L > 1$. Third, the Gryning model by construction applies to heights below h_{ABL}. Under strongly stable stratification, h_{ABL} is generally well below 200 m (Gryning et al. (2007) find an

average $h_{ABL} \approx 60$ m), and therefore the usefulness of the Gryning model at altitudes relevant to wind energy is limited. Fourth, the $1/(h_{ABL} - z)$ term is appropriate in unstable and neutral conditions in the presence of a capping inversion at the top of the ABL, but not appropriate in stable conditions in which the entire ABL is within the inversion. Finally, the L_{MBL} value (which typically ranges between 40 m and 150 m) is unable to capture the very low mixing lengths observed in very stable stratification. In stable conditions l_m can be significantly smaller above the SL, as low as even 1 m in extremely stable conditions (Stull, 1988). A more appropriate scaling of L_{MBL} may be a linear dependence on the surface Obukhov length (Delage, 1974; Stull, 1988) which would result in lower l_m values and would still result in an analytical expression for $\bar{U}(z)$ as in Eq. 2.19. Other limits for l_m under stable stratification include the Ozmidov length or buoyancy length scale (Stull, 1988), although neither of these result in an analytic expression for $\bar{U}(z)$.

2.5.2 Alternative model for stable conditions

To illustrate the sensitivity of modifications of MOST to their inherent assumptions, we introduce here an alternative to the Gryning model designed to be more applicable in stable conditions above the SL. First, we scale L_{MBL} linearly with G and limit the size of l_m by the surface Obukhov length (Delage, 1974; Weng and Taylor, 2003),

$$l_m(z) = \left(\frac{\phi_m(\frac{z}{L})}{\kappa z} + \frac{f}{aG} + \frac{1}{bL} \right)^{-1} \tag{2.21}$$

where a and b are constants. We adopt the value $a = 0.0027$ in Weng and Taylor (2003) and set $b = 1$. In addition, we allow for any form of ϕ_m to be used, particularly forms that are more appropriate for $z/L > 0.5$ than the Businger et al. (1971) form. This generalized approach to ϕ_m complicates the integration of the non-dimensional wind speed equation when the profile form of u_* (Eq. 2.15) is used, and results in a large number of terms in the logarithmic wind speed equation. To simplify the integration, we retain u_* as constant with altitude as in MOST. We recognize that this form of u_* is inappropriate up to 200 m in weakly to moderately stable conditions, but may be no less accurate than Eq. 2.15 in very stable conditions where surface decoupling and turbulence generation underneath an LLJ may result in turbulent flux profiles that do not decrease monotonically with altitude. Integrating Eq. 2.1 using these proposed modifications leads to,

$$\bar{U}(z_2) = \bar{U}(z_1) + \frac{u_*}{\kappa}\left[\ln\left(\frac{z_2}{z_1}\right) - \psi_m\left(\frac{z_2}{L}, \frac{z_1}{L}\right) + \kappa(z_2 - z_1)\left(\frac{f}{aG} + \frac{1}{bL}\right)\right] \quad (2.22)$$

2.5.3 Comparing different wind speed models

We have discussed several limitations of the logarithmic wind speed model, particularly under stable stratification, and have presented two distinct modifications to the model intended to improve extrapolation accuracy under such conditions. We now compare the performance of these different wind speed profile models. The input parameters needed to apply these modified wind profile models and the intended improvements over the standard flux-based MOST model are summarized in Table 2.4.

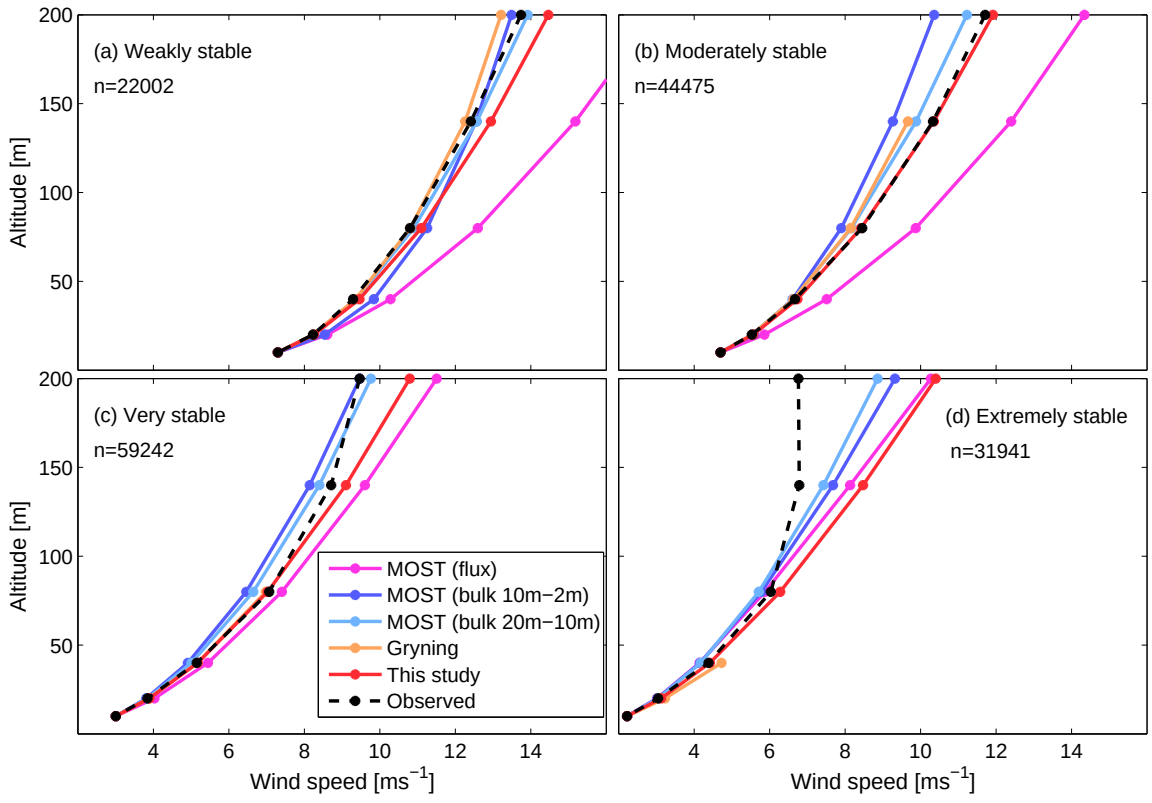

Figure 2.11: Modelled (Table 2.4) and observed mean wind speed profiles for the different stability classes.

We compare the wind profile models for weakly stable through extremely stable

Model	Input parameters	Description	Intended improvements
MOST (flux)	U_{10}, z_0, u_*, $(\overline{w'\theta'})$	10 m winds are vertically extrapolated using Eq. 2.6 using L values derived from 5 m fluxes and the 'Drag, 20m' formulation of z_0	N/A
MOST (bulk 10m-2m)	U_{10}, z_0, θ_2, θ_{10}	10 m winds are vertically extrapolated using Eq. 2.6 using L values derived from Ri_B between 10 m and 2 m and the 'land-use, mesocale' formulation of z_0	Corrects for high magnitudes of surface stability caused by the IBL at Cabauw
MOST (bulk 20m-10m)	U_{10}, U_{20}, θ_{10}, θ_{20}	10 m winds are vertically extrapolated using Eq. 2.9 using L values derived from Ri_B between 20 m and 10 m	In addition to the above, does not require the use of z_0
Gryning	U_{10}, U_{20}, θ_{10}, θ_{20}, G	10 m winds are vertically extrapolated using Eq. 2.19 using L values derived from Ri_B between 20 m and 10 m	In addition to all the above, accounts for decreasing turbulent fluxes with height using height-dependent mixing length and friction velocity formulations
This study	U_{10}, U_{20}, θ_{10}, θ_{20}, G	10 m winds are vertically extrapolated using Eq. 2.22 and L values derived from Ri_B between 20 m and 10 m	Similar intended improvements as in the Gryning model, but does not require h_{ABL} as a parameter and permits any form of ψ_m to be used

Table 2.4: Wind speed profile models considered in this analysis, along with required input parameters, description of model, and intended improvements over the standard flux-based MOST model.

stratification, the range across which MOST breaks down at higher altitudes. Each wind speed profile model uses different sets of observations, which are subject to data gaps that occur at different times and altitudes. To make meaningful comparisons between models, all profiles are computed for times when data are available for all models. Since the Gryning model is inapplicable above $z > h_{ABL}$, we limit the wind profile for this model up to 140 m in moderately stable conditions, 80 m in very stable conditions, and 40 m in extremely stable conditions, while the remaining wind profile models are extrapolated up to 200 m across all stability classes. For models that use z_0 as a lower boundary, the z_0 formulation is selected which results in the highest accuracy in the mean wind speed profile up to 80 m in weakly stable conditions, based on Figs. 2.4 and 2.6. We use the Beljaars and Holtslag (1991) form of ψ_m for each model (apart from the Gryning model which by construction uses the Businger et al. (1971) form).

In Fig. 2.11, observed and modelled mean wind speed profiles under different stability classes are compared. In general, higher mean wind speeds are observed in the lower stability ranges and lower mean wind speeds are observed in the higher stability ranges. In extremely stable conditions, a LLJ is observed on average at 140 m. The models under consideration are reasonably accurate up in weakly stable conditions, apart from the MOST (flux) model which overestimates wind speeds due to the influence of the IBL at Cabauw. The models begin to diverge above 40 m in moderately stable conditions. Most models tend to underestimate wind speeds in moderately stable conditions while the model proposed in this study is accurate on average. In very stable conditions, the MOST (flux) model is more accurate compared to its performance in the lower stability classes. This result can be attributed to a lower altitude and decreased influence of the IBL at higher stability. All models are accurate on average up to 80 m in extremely stable conditions (apart from the Gryning model which is limited to 40 m) but by construction are unable to account for the LLJ.

Box plots of the relative difference between modelled and observed winds (i.e. $(U_{mod} - U_{obs})/U_{obs}$) at different altitudes and stability classes are shown in Fig. 2.12. In general, the spread of the model predictions around the observed wind speeds increases with stability and altitude. As seen in Fig. 2.12, the MOST (bulk 20m-10m) model generally results in less spread than the other MOST approaches. We attribute this result to the use of z_0 in the other MOST approaches, which as discussed in Sect. 2.3.1 is difficult to quantify and has considerable influence on the wind speed profile.

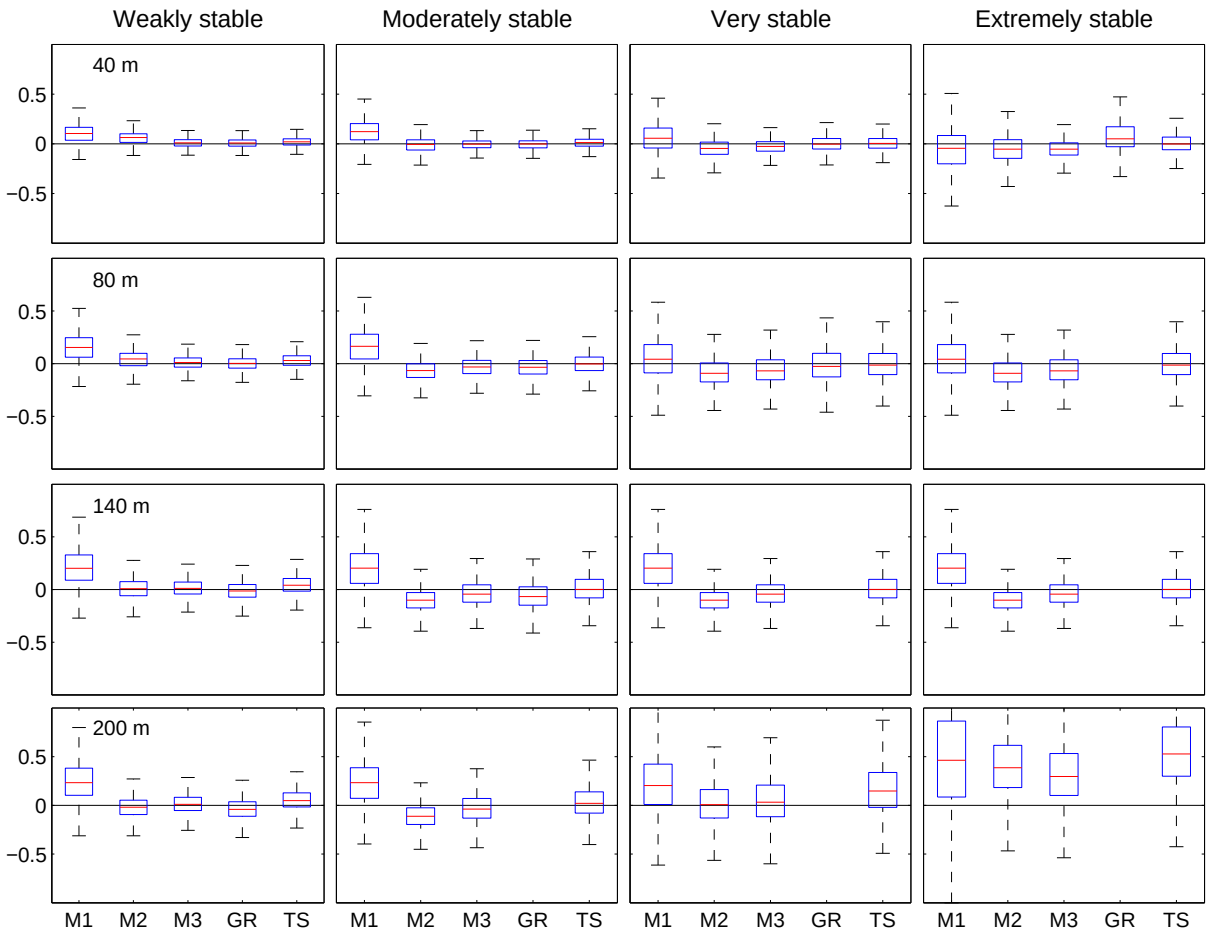

Figure 2.12: Box plots of the relative difference between modelled and observed winds (i.e. $(U_{mod} - U_{obs})/U_{obs}$) at different altitudes (columns) and stability classes (rows). The red lines show the mean values, blue boxes show the interquartile range, and black lines show the total range excluding outliers. Acronyms for the different models are as follows: M1 - MOST (flux), M2 - (bulk 10m-2m), M3 - (bulk 20m-10m), GR - Gryning, TS - this study.

However, the MOST (bulk 10m-2m) often shows less spread than MOST (bulk 20m-10m), particularly in the higher stability ranges. This result can be attributed to high sensitivity in the L_{20-10} values when U_{20} and U_{10} are small. The model proposed in this study generally has similar spread to MOST (bulk 20m-10m) across all altitudes and stability classes. The Gryning model shows large spread at 40 m in extremely stable conditions due to the breakdown of the Businger et al. (1971) formulation of ψ_m.

2.6 Discussion

This analysis has demonstrated in detail the limitations of similarity-based approaches to wind speed extrapolation up to altitudes relevant to wind energy production in stable conditions. The first limitation we considered related to the z_0 parameter. In general, the value of z_0 for a given wind direction will change with stratification and altitude, given the effects of IBLs in inhomogeneous terrain and the rotation of the wind vector with altitude. A robust characterization of surface roughness should involve measurements of the effective z_0 at different altitudes and different degrees of stability, but such a characterization is generally impractical and inconsistent with the simplicity of the logarithmic wind speed model. In addition, the numerous formulations of z_0 (which demonstrate a broad range of values for a given wind direction), as well as considerable ambiguity on which formulation is most appropriate in a given context, increases the uncertainty associated with z_0 for wind profile modelling. Given these limitations and considering the high sensitivity of the logarithmic wind speed model to z_0, it is not surprising that considerable spread in modelled wind speed profiles was found.

The specification of z_0 in the logarithmic wind speed model is required in atmospheric models in order to calculate turbulent fluxes between the surface and the lowest model height (i.e. 10 m). However, as demonstrated in this study, z_0 is not required when extrapolating near-surface wind speeds to higher altitudes. Rather, with a simple generalization (Eq. 2.9), a near-surface height (e.g. 10 m) can be used as the lower boundary condition provided wind speed measurements are made at this height. Through this approach, surface roughness is characterized indirectly through the near-surface stratification and shear. As shown in this study, this approach substantially reduced the spread of model results (Fig. 2.12). To our knowledge, the logarithmic wind speed model has only been associated with a lower boundary of z_0 in the literature, and the alternative approach proposed here has not been discussed. The extra difficulty and expense of having to measure wind speeds at some altitude above the surface (though generally done in pre-construction wind resource assessments) comes at the considerable benefit of not having to specify the poorly-constrained parameter z_0.

We further demonstrated that the flux-based near-surface measurements of the Obukhov length L are also not required for wind speed extrapolation, and we showed how using a bulk-derived L value based on wind speed and temperature measurements

between two altitudes can provide more accuracy as well as flexibility in the presence of IBLs. For example, if a pronounced IBL below 20 m is observed at a given site, bulk measurements of L can be made above this height (i.e. at 30 m and 40 m) which would be more representative of the flow aloft and would provide improved extrapolation accuracy. Moreover, this approach potentially reduces the cost of obtaining field observations, as wind speed and temperature measurement devices are generally less expensive than turbulent flux measurement devices (although measurements are required at a minimum of two altitudes). We note that the particular structure of the IBL at Cabauw is specific to the site, but a similar IBL structure may exist at many wind farm sites, which are often constructed in locally flat, open terrain. Despite the advantages of a bulk Obukhov length, this approach still assumed the validity of MOST within the altitude range in which the bulk values were measured, and therefore broke down under increasing stable stratification.

Indeed, many aspects of similarity theory were shown to break down in increasing stable stratification. This breakdown was associated with the divergence of different forms of ϕ_m beyond weakly stable conditions, and was evident in the modified model by Gryning et al. (2007) and the model proposed in this study. These models were specifically designed to extend the range of application of the logarithmic wind speed model above the SL, yet did not improve the accuracy of wind speed extrapolations. Rather, these modifications simply added more uncertainty given the range of additional parameters considered. Specifically, the use of h_{ABL} and L_{MBL} in the Gryning model, and the a and b coefficients in the alternative model we explored, are subject to a wide range of possible parameterizations and values (Stull, 1988). Indeed, a combination of inaccurate parameterizations may in certain cases still lead to an accurate mean wind speed profile. In this regard, some consideration of model spread (such as the box plot in Fig. 2.12) is crucial in distinguishing between valid parameterizations resulting in robust extrapolations and invalid parameterizations that appear on average to produce accurate results. The MOST (flux) model is a striking example. This model appeared accurate up to 80 m in extremely stable conditions (Fig. 2.11), but exhibited substantial spread (Fig. 2.12) that clearly highlighted the breakdown of the model. Generally, literature on models for wind speed extrapolation do not include measures of model spread. Inclusion of such measures in future studies of wind profile models will provide more transparency and allow more meaningful interpretation of model results.

Results shown in this study clearly demonstrate that, despite a wide range of in-

tended improvements, similarity-based wind speed profile models are limited in their application up to about 100 m with stratification no stronger than moderately stable. Above this altitude and for stronger stable stratification, the underlying assumptions of similarity theory break down, and logarithimic wind profiles are no longer representative of the flow up to altitudes relevant to wind energy production. As demonstrated in this study, the influence of the Coriolis force becomes non-negligible under such conditions, resulting in the rotation of the wind vector with altitude (and the associated maximum in the wind speed profile) and the development of time-dependent phenomena such as inertial oscillations and LLJs. Similarity-based models are by construction unable to account for such rotational and time-dependent influences. As turbine hub-heights now extend up to 125 m, and altitudes swept out by a turbine blade can now exceed 200 m, the Coriolis force must be considered for wind energy estimation for all degrees of stability except perhaps under strongly unstable conditions. More physically appropriate extrapolation models that account for the Coriolis force and are thus more applicable at these upper altitudes are required.

2.7 Conclusions

In this study, we have considered the limitations of similarity-based approaches to wind speed extrapolation and their breakdown under increasingly stable stratification. The models we have considered vary from traditional MOST using observed winds at 10 m and surface fluxes, to similarity-based formulations that account for gradients of turbulent fluxes across the ABL. Using 10 years of data from the 213 m tower at Cabauw, we demonstrated the sensitivity of the logarithmic wind speed model to a wide range of possible formulations of z_0 and the tendency of a surface flux-derived Obukhov length to overestimate the magnitude of stability aloft in the presence of IBLs. We then showed that z_0 is not required in the logarithmic wind speed model provided wind speed measurements are available at some lower altitude. We further demonstrated that using a bulk form of the Obukhov length measured between two near-surface altitudes provided significant improvements in wind speed extrapolation accuracy, compared to the standard surface flux-based approach. We then illustrated the breakdown of MOST above the SL, the height of which decreases substantially with increasing stratification. In particular, we associated the breakdown of MOST with the divergence of the stability function for $z/L > 0.5$, the rotation of the wind vector with altitude due to the Coriolis force, and the degree of surface decoupling

from winds aloft. Modifications to the logarithmic wind speed model proposed by Gryning et al. (2007) and alternative modifications introduced in this study were not found to improve extrapolation accuracy in higher stability classes. With increasing height and stable stratification, all models considered here became increasingly inaccurate. Similarity-based models cannot account for the increased role of the Coriolis force under weak turbulence, which results in the rotation of the wind vector with altitude and frequent LLJs. Given that modern hub-heights and altitudes swept out by a wind turbine blade extend well beyond the range of applicability of MOST in stable conditions, new extrapolation equations are required that are more applicable at these altitudes.

Chapter 3

Moving beyond Monin-Obukhov similarity theory in modelling wind speed profiles under stable stratification

The contents of this chapter are based on the following manuscript:

Optis, M., A. Monahan, and F.C. Bosveld (2014). 'Moving Beyond Monin-Obukhov Similarity Theory in Modelling Wind-Speed Profiles in the Lower Atmospheric Boundary Layer under Stable Stratification'. *Boundary-Layer Meteorol*, **153**, 497-514.

Note that F. Bosveld provided and helped to interpret some data used in this analysis, and also provided feedback on the manuscript. The analysis presented here was conducted by M. Optis.

3.1 Introduction

An accurate characterization of the near-surface wind-speed profile (up to altitudes of about 200 m) is important for a variety of wind energy applications, including wind energy resource assessment and forecasting, and estimating wind shear across turbine blades. For this purpose, the wind energy community uses a range of models of different degrees of complexity, including mesoscale or regional scale models (e.g. Weather Research and Forecasting model) and microscale models (e.g. Wind Atlas

Analysis and Application Program (WAsP)). However, such models can be computationally and financially expensive and may be unsuitable for situations in which quick and cost-effective methods for wind energy assessment are needed, such as the preliminary assessment of a wind energy resource from field data. For cases in which the measurement of near-surface wind speeds has been made (e.g. 10 m winds at nearby weather stations, 60 m winds at meteorological towers), the extrapolation of near-surface winds to hub-height using simple diagnostic models can often be a more practical and cost-effective approach.

The most established of these simple models fols from considering the vertical gradient of wind speed within the framework of Monin-Obukhov similarity theory (MOST; Monin and Obukhov, 1954), viz.

$$\phi_m\left(\frac{z}{L}\right) = \frac{\kappa z}{u_*}\frac{\partial \bar{U}}{\partial z}, \tag{3.1}$$

where ϕ_m is the non-dimensional wind shear, u_* is the friction velocity, $\bar{U}$ is the time-averaged wind speed, κ is the von Kármán constant (normally taken to be 0.4) and z is the height above the surface. The dimensional quantity L is the Obukhov length,

$$L = -\frac{u_*^3 \theta_s}{\kappa g(\overline{w'\theta'})_s}, \tag{3.2}$$

where g is the acceleration due to gravity, θ_s is the surface potential temperature, and $(\overline{w'\theta'})_s$ is the surface turbulent kinematic heat flux. Integrating Eq. 3.1 leads to

$$\bar{U}(z) = \frac{u_*}{\kappa}\left[\ln\left(\frac{z}{z_0}\right) - \psi_m\left(\frac{z}{L}, \frac{z_0}{L}\right)\right], \tag{3.3}$$

where ψ_m accounts for the influence of stability and is derived from ϕ_m,

$$\psi_m\left(\frac{z}{L}, \frac{z_0}{L}\right) = \int_{z_0/L}^{z/L} \frac{1-\phi_m(\zeta)}{\zeta}\,\mathrm{d}\zeta. \tag{3.4}$$

Although Eq. 3.3 is not strictly logarithmic when $\psi_m \neq 0$, we follow common practice in the literature and refer to the profile in Eq. 3.3 as the 'logarithmic wind-speed equation'. To derive Eq. 3.3, it is assumed that u_* and L are constant with altitude. This assumption limits the applicability of the logarithmic wind-speed profile to the

surface layer (ASL), the lowermost portion of the atmospheric boundary layer (ABL) (approximately the bottom $\approx$ 10 %) in which changes in the turbulent fluxes with altitude are small ($\approx$ 10 %) compared to their surface values. Furthermore, Eq. 3.3 considers only wind speed and not separate wind-vector components, and thus cannot model the rotation of the wind vector with altitude due to the Coriolis force. Within the surface layer, this rotation is generally negligible and Eq. 3.3 is normally found to be a good representation of the wind-speed profile (Lange and Focken, 2005; Emeis, 2013).

The height of the surface layer, h_{ASL}, is strongly influenced by stability. Under neutral and especially unstable conditions, vertical turbulent mixing is normally intense in the lower few hundred metres of the ABL, resulting in h_{ASL} as great as 200 m or more (Stull, 1988; Garratt, 1994). Under stable stratification, the suppression of vertical turbulent mixing results in a rapid decrease of turbulent fluxes with altitude from the near-surface shear layer. Consequently, the ASL depth is significantly lower, ranging from about 20-30 m under moderately stable conditions to 1-5 m under extremely stable conditions (Stull, 1988; Garratt, 1994). Under these conditions, and to the extent that the assumptions of MOST are still valid (Mahrt, 1998), the logarithmic wind-speed profile is valid only at very low altitudes.

Under conditions of extreme stability, turbulent fluxes become so weak and intermittent above a very shallow ASL that winds aloft can decouple from the surface. Under this regime of 'z-less stratification', the turbulent flux and intensity become localized and are no longer affected by the distance from the surface, making the surface-based mixing length $l_m = \kappa z \phi_m^{-1}$ assumed by MOST an inappropriate turbulent length scale (Nieuwstadt, 1984; Mahrt, 1999; Mahrt and Vickers, 2006; Sorbjan and Grachev, 2010). In this regime, the importance of physical mechanisms other than turbulence increases. Inertial oscillations in particular have considerable influence and often lead to the formation of low-level jets (LLJs) below 200 m (Baas et al., 2009; Van de Wiel et al., 2010; Banta et al., 2013). Baroclinicity can influence wind-speed shear and momentum mixing across all stabilities, while gravity waves become influential under extreme stability (Mahrt, 1999; Mahrt and Vickers, 2006).

Despite the limitations of the logarithmic wind-speed profile in stable conditions, it is still frequently used under these conditions for wind energy resource assessment and forecasting at altitudes within a few hundred metres of the surface. Over the last two decades, it has been used extensively in the field of wind energy meteorology (e.g. Troen and Petersen, 1989; Petersen et al., 1998; Burton et al., 2001; Lange

and Focken, 2005; Motta et al., 2005; van den Berg, 2008; Monteiro et al., 2009; Emeis, 2010, 2013; Giebel, 2011; Drechsel et al., 2012). For wind energy forecasting in particular, the logarithmic wind-speed profile has been used to interpolate wind speeds between two NWP model levels to hub-height, extrapolate observed wind speeds (e.g. tower measurements) to hub-height, or extrapolate the geostrophic winds to hub-height using the friction velocity computed from the geostrophic-drag law (Tennekes, 1973).

3.1.1 Intent and overview of study

The intent of this study is to assess the accuracy of several alternatives to MOST-based models in simulating the wind profile up to 200 m in stable stratification. We only consider equilibrium models in this present study, and therefore time-dependent phenomena such as LLJs cannot be modelled. The data sources used are described in Sect. 3.2, and the wind-speed profile models are described in Sect 3.3. In Sect. 3.4, methods used to determine model parameters are described, and results of the model comparison are shown in Sect. 3.5. A discussion is provided in Sect. 3.6, and conclusions in Sect. 3.7.

3.2 Data sources

This study makes use of data obtained from the Cabauw meteorological tower in the Netherlands, operated by the Royal Netherlands Meteorological Institute (KNMI). Measurements of meteorological variables at 10-min resolution were obtained from July 1 2007 to June 30 2008 (these data are available at http://www.cesar-database.nl). Wind speed and direction measurements are made at 10 m, 20 m, 40 m, 80 m, 140 m, and 200 m, and temperature measurements made at these altitudes as well as 2 m. Surface pressure measurements are also provided, which are used to calculate the potential temperature at different heights. Turbulent momentum and kinematic heat-flux measurements made at altitudes of 5 m, 60 m, 100 m and 180 m are provided by KNMI. Surface geostrophic wind components at 1-hr resolution derived from surface pressure measurements in the regional vicinity of Cabauw are provided by KNMI and are linearly interpolated to 10-min resolution. Observations for which 200 m wind speeds < 5 m s^{-1} are excluded from the analysis (representing 22 % of the data). Under these conditions, the flux-gradient relationships are known to perform poorly

(Mahrt, 1998). Furthermore, low wind-speed conditions are not of interest for wind energy applications (i.e. wind speeds are below the cut-in limit for a wind turbine and therefore no power is generated), so the accuracy of different wind-speed profile models under these conditions is not relevant in the present context.

3.3 Description of alternative wind speed profile models

Here, we introduce different wind-speed profile models considered in this analysis, as well as the data needed to use them for wind-speed extrapolation.

3.3.1 Local similarity

Local similarity (Nieuwstadt, 1984; Sorbjan, 1988; Sorbjan and Grachev, 2010) is an extension of MOST above the surface layer. Its basic premise is that non-dimensionalized turbulence statistics at a given altitude can be determined based on local observations in the same way that statistics for the ASL are based on surface observations in MOST. This concept is applied only in stable conditions, as turbulent transport in unstable conditions can be highly non-local. Sorbjan (1988) argued that the forms of the similarity functions for local similarity and MOST should be identical, so the wind-speed profile between two nearby altitudes can be expressed as

$$\bar{U}(z_2) = \bar{U}(z_1) + \frac{\sqrt{(\tau/\rho_0)_l}}{\kappa}\left[\ln\left(\frac{z_2}{z_1}\right) - \psi_m\left(\frac{z_2}{L_l}, \frac{z_1}{L_l}\right)\right], \tag{3.5}$$

with $z_2 > z_1$, and $(\tau/\rho_0)_l$ and L_l correspond to the local momentum flux and Obukhov length, respectively. As with MOST, local similarity is based on the assumption of continuous turbulence and becomes invalid for weak and intermittent turbulence (i.e. very stable conditions). Therefore, local similarity should be least accurate in the high stability regimes (though not as inaccurate as MOST). In this context, local similarity provides an upper limit to the accuracy of similarity-based logarithmic wind-speed profile modelling, and serves as a useful benchmark for comparing other wind-speed profile models.

3.3.2 Gryning model

Modifications to the logarithmic wind-speed profile applicable within the entire ABL were proposed by Gryning et al. (2007) and applied in a number of subsequent studies (e.g. Gryning and Batchvarova, 2008; Pena et al., 2010; Sathe et al., 2011, 2012; Kumar and Sharan, 2012). Gryning et al. (2007) proposed two key modifications: the first replaces u_* in Eq. 3.1 with an altitude-dependent turbulent momentum flux, expressed as a linear function of u_* and the ABL height, h_{ABL} (Panofsky, 1973),

$$\sqrt{\tau(z)/\rho_0} = u_* \left(1 - \frac{z}{h_{ABL}}\right). \tag{3.6}$$

The second modification replaces the surface-layer form $l_m = \kappa z$ in Eq. 3.1 with a generalized form of the Blackadar (1962) mixing length,

$$l_m(z) = \kappa \left(\frac{\phi_m(\frac{z}{L})}{z} + \frac{1}{L_{MBL}} + \frac{1}{h_{ABL} - z}\right)^{-1} \tag{3.7}$$

The first term in Eq. 3.7 results in the standard MOST mixing length for small values of z; the second term is a mid-boundary-layer mixing length (with $L_{MBL} < h_{ABL}$) that places an upper bound on the magnitude of l_m. This term is set as a constant or parametrized by other means (e.g. through the geostrophic drag law in Gryning et al. (2007)). The final term results in the mixing length decreasing to zero at the top of the ABL, above which turbulence should normally be negligible. Integrating the non-dimensional wind-speed shear equation with these new parametrizations and using the Businger et al. (1971) form $\phi_m = 1 + \beta z/L$ (with $\beta = 5$), Gryning et al. (2007) derive the following modified equation,

$$\bar{U}(z) = \frac{u_*}{\kappa}\left[\ln\left(\frac{z}{z_0}\right) + \beta\frac{z}{L}\left(1 - \frac{z}{2h_{ABL}}\right) + \frac{z}{L_{MBL}} - \frac{z^2}{2h_{ABL}L_{MBL}}\right]. \tag{3.8}$$

Results from Gryning et al. (2007) and subsequent studies (e.g. Pena et al., 2010; Emeis, 2013) have demonstrated the ability of the modified model to provide more accurate wind-speed profiles within the ABL under all stabilities compared to the standard MOST approach.

The assumptions of the Gryning model limit its application under conditions of

stable stratification. First, the model is by construction applicable at heights below h_{ABL}. Under stable conditions, h_{ABL} is relatively small and may not be well defined (e.g. Stull, 1988; Seidel et al., 2010). For very stable conditions, Gryning et al. (2007) find an average $h_{ABL} \approx 60$ m, and above $z = 60$ m the model cannot be applied. Second, although the proposed asymptotic formulation of l_m is appropriate for neutral and unstable conditions, it is unable to capture the very low mixing lengths observed in very stable stratification. The L_{MBL} value typically ranges between 40 m and 150 m. In stable conditions l_m can be significantly smaller above the ASL, as low as even 1 m in extremely stable conditions (Stull, 1988). A more appropriate scaling of L_{MBL} may be a linear dependence on the surface Obukhov length (Delage, 1974; Stull, 1988) which would result in lower l_m values and would still result in an analytical expression for $\bar{U}(z)$ as in Eq. 3.8. Other limits for l_m under stable stratification include the Osmodov length or buoyancy length scale (Stull, 1988), although neither of these result in an analytic expression for $\bar{U}(z)$. Finally, the Gryning model is still founded on similarity principles, and thus cannot model the rotation of the wind vector due to the increased influence of the Coriolis force in stable conditions.

3.3.3 Ekman layer and Two-layer models

Turbulent fluxes within the stable ABL are generally parametrized as diffusion processes (e.g. $\overline{u'w'} = -K_m \partial\bar{u}/\partial z$, with K_m the diffusivity coefficient). In general, K_m increases approximately linearly with height in the ASL, reaches a maximum above the surface layer and decreases asymptotically to zero at the top of the ABL. A common idealized approach is to approximate K_m as constant above the ASL (the so-called Ekman layer), which results in a 'two-layer' model in which K_m increases linearly in the ASL up to h_{ASL} and remains constant above. Within the Ekman layer, considering the balance between the pressure-gradient force, the Coriolis force and the turbulent momentum-flux divergence, and assuming stationarity, results in the well-known Ekman layer equations,

$$u(z) = u_G + (u_{BC} - u_G)\mathrm{e}^{-\gamma z_T}\cos(\gamma z_T) + (v_{BC} - v_G)\mathrm{e}^{-\gamma z_T}\sin(\gamma z_T), \tag{3.9a}$$

$$v(z) = v_G + (v_{BC} - v_G)\mathrm{e}^{-\gamma z_T}\cos(\gamma z_T) - (u_{BC} - u_G)\mathrm{e}^{-\gamma z_T}\sin(\gamma z_T) \tag{3.9b}$$

where u_G and v_G are the geostrophic wind vector components, u_{BC} and v_{BC} are the components of the wind vector at some specified lower boundary z_{BC} (for example, taken to be the surface where the flow vanishes), $\gamma = \sqrt{f/(2K_m)}$, and $z_T = z - z_{BC}$. The Ekman layer model can be used to describe the entire wind-vector profile (i.e. $z_{BC} = 0$) or can be used within a two-layer MOST-Ekman framework (i.e. $z_{BC} = h_{ASL}$). A hodograph representation of this two-layer model is shown in Fig. 3.1 Blackadar (1998). By accounting for the Coriolis force, the Ekman layer equations result in the rotation of the wind vector with altitude (the so-called Ekman spiral). The geometry of the Ekman spiral is such that a tangent at any point along the spiral in Fig. 3.1 makes a 45^o angle with the vector joining this point to the geostrophic wind vector (Blackadar, 1998), as shown in Fig. 3.1. Consequently, the angle α between the wind below $z = h_{ASL}$ and the geostrophic wind is between 0 and 45^o. The Ekman layer profile is then a special case of the two-layer model when $h_{ASL} = 0$ and $\alpha = 45^o$. Provided K_m is sufficiently small (in conditions of weak turbulence, such as under stable stratification), both the Ekman layer and two-layer models result in low altitude maxima in the wind-speed profile (evaluated to occur at $z = 2.28\gamma^{-1} + z_{BC}$). Furthermore, the Ekman layer equations are particularly appealing in cases of surface decoupling (i.e. very stable conditions), since the winds are not determined entirely by the near-surface wind.

The Ekman layer model has been used as an idealization in introductory studies of the ABL (e.g. Stull, 1988; Garratt, 1994; Blackadar, 1998; Etling, 2002; Emeis et al., 2007; Donda et al., 2013) as well as recent conceptual studies of stable ABL phenomena such as low-level jets (e.g. Van de Wiel et al., 2010; Baas et al., 2012). The two-layer model was discussed in Blackadar (1998) in the context of deriving the geostrophic-drag law. Emeis et al. (2007) and Emeis (2013) applied this two-layer model for wind-speed profile modelling up to hub-height in non-neutral conditions,

$$U(z) = \begin{cases} \frac{u_*}{\kappa}\left[\ln(z/z_0) - \psi_m(z/L, z_0/L)\right] & z < h_{ASL}, \\ G\left[\cos(\alpha) - \sin(\alpha)\right] & z = h_{ASL}, \\ G[1 - 2\sqrt{(}2)\mathrm{e}^{-\gamma(z-h_{ASL})}\sin(\alpha)\cos(\gamma(z-h_{ASL}) & \\ +\pi/4 - \alpha) + 2\mathrm{e}^{-2\gamma(z-h_{ASL})}\sin^2(\alpha)]^{1/2} & z > h_{ASL}, \end{cases} \tag{3.10}$$

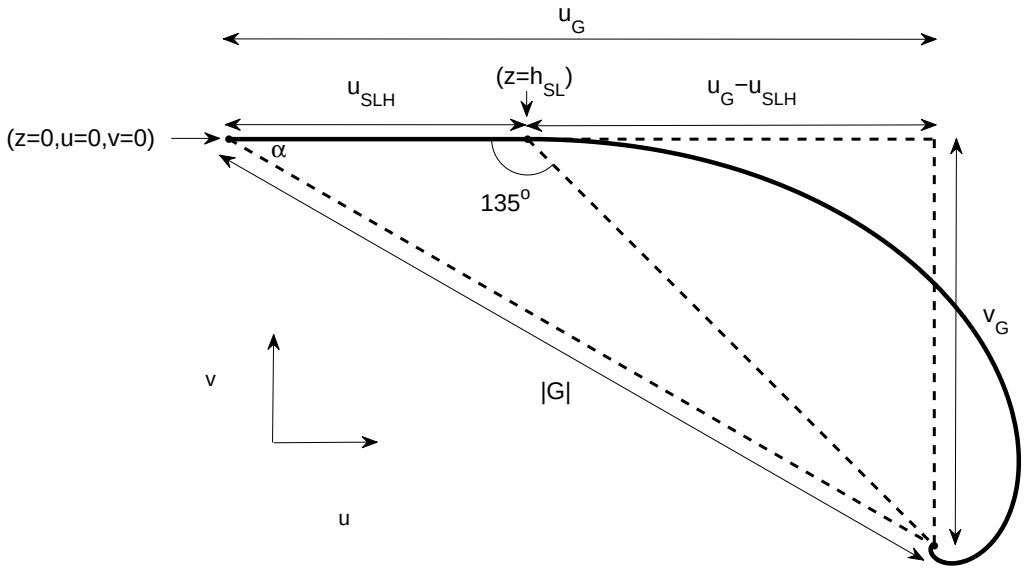

Figure 3.1: Wind hodograph of the two-layer model used in this analysis (adapted from Blackadar (1998)). The co-ordinate system is aligned with the ASL winds such that $v_{ASL} = 0$. The wind vector increases from (0, 0) at the surface to $(u_{SLH}, 0)$ at h_{ASL} with constant wind direction under a MOST-based logarithmic profile. Above h_{ASL}, the wind vector rotates along the Ekman spiral asymptoting to the geostrophic values u_G and v_G. The angle between the near-surface wind and the geostrophic wind vectors is denoted α. When $\alpha = 0^o$, the wind profile is described entirely by the MOST-based logarithmic profile. When $\alpha = 45^o$, the wind profile is described entirely by the Ekman layer model.

where G is the magnitude of the geostrophic wind vector. The expression for $U(z)$ for the case $z = h_{ASL}$ follows from Fig. 3.1, while the expression for $U(z)$ for the case $z > h_{ASL}$ follows from the Ekman layer equations (Eq. 3.9).

By equating the MOST-based and Ekman-based wind speeds and their vertical gradients at the interface h_{ASL}, Emeis (2013) derived two expressions relating the internal parameters of the model,

$$u_* = \frac{\kappa G\left(\cos(\alpha) - \sin(\alpha)\right)}{\ln(h_{ASL}/z_0) - \psi_m(h_{ASL}/L, z_0/L)}, \tag{3.11}$$

$$u_* = \frac{2G\gamma\kappa h_{ASL}\sin(\alpha)}{\phi_m(h_{ASL}/L)}. \tag{3.12}$$

In Emeis (2013), $h_{ASL} = 150$ m and $L = -200$ m were specified for daytime and $h_{ASL} = 30$ m and $L = 150$ m for nighttime conditions. Equations 3.11 and 3.12 were then solved for α and u_*, and the resulting mean wind-speed profiles were compared to those from MOST-based and Gryning et al. (2007) models over an urban area using 1 month of data. The results of this earlier study showed that the two-layer model provided the most accurate mean wind-speed profiles of all the models considered. While Emeis (2013) demonstrated the potential of this model, important issues were not addressed: the values of h_{ASL} and L were not justified, the sample size was relatively small (i.e. 1 month of data), and no indication of scatter in individual wind-speed profiles (e.g. standard deviation, root mean-squared error) was provided. The present study extends the earlier results of Emeis (2013).

3.4 Methods

Having described the different wind-profile models, we now describe the application of these models to the problem of wind-speed extrapolation. We consider model performance within different stability classes based on the bulk Richardson number determined between 200 m and the surface (Table 3.1),

$$Ri_B = \frac{g}{\theta_{avg}}\frac{z_{200}(\theta_{200} - \theta_{surf})}{U_{200}^2} \tag{3.13}$$

where θ_{avg} is the mean potential temperature across all measurement altitudes between 2 m and 200 m. Temperature measurements at 2 m are used for the surface values. The Beljaars and Holtslag (1991) functional forms for ψ_M and ψ_H (the similarity function for heat) in stable conditions are used throughout the analysis, as these forms were derived using Cabauw data,

$$\psi_m = -a\left(\frac{z}{L} - \frac{z_0}{L}\right) - b\left(\frac{z}{L} - \frac{c}{d}\right)\exp\left(-d\frac{z}{L}\right) + b\left(\frac{z_0}{L} - \frac{c}{d}\right)\exp\left(-d\frac{z_0}{L}\right), \tag{3.14}$$

$$\psi_h = -\left(1+\frac{2}{3}a\frac{z}{L}\right)^{3/2} + \left(1+\frac{2}{3}a\frac{z_0}{L}\right)^{3/2} - b\left(\frac{z}{L}-\frac{c}{d}\right)\exp\left(-d\frac{z}{L}\right) + b\left(\frac{z_0}{L}-\frac{c}{d}\right)\exp\left(-d\frac{z_0}{L}\right), \quad (3.15)$$

with $a = 1$, $b = 2/3$, $c = 5$, and $d = 0.35$. One exception is the Gryning model (Eq. 3.8), which by construction uses the simplified Businger et al. (1971) form of ϕ_m that keeps the number of terms of Eq. 3.8 to a minimum.

Stability class	Ri_B criteria	Occurrence (%)
Unstable	$Ri_B < 0$	15.1
Weakly stable	$0 < Ri_B < 0.05$	29.2
Moderately stable	$0.05 < Ri_B < 0.15$	23.3
Very stable	$0.15 < Ri_B < 0.5$	22.0
Extremely stable	$Ri_B > 0.5$	10.4

Table 3.1: Stability classes used throughout this analysis, based on Ri_B between 200 m and the surface

Both the input observational data as well as the methods used to determine internal parameters vary between models. A summary of observed and prescribed input parameters as well as internally computed parameters for each model is shown in Table 3.2. We now turn to more detailed descriptions of the methods used.

3.4.1 MOST (local z_0)

The immediate surroundings at Cabauw (within 200 m) are relatively flat while farther away from the tower (within 1-2 km) surface roughness increases significantly due to the presence of small towns and belts of trees (Verkaik and Holtslag, 2007). This effect produces internal boundary layers (IBLs) in the flow around Cabauw, and in particular results in lower than expected turbulent flux values near the surface compared to higher altitudes (a detailed discussion of IBL effects at Cabauw is provided in Verkaik and Holtslag (2007)). This effect is demonstrated in Fig. 3.2, in which mean turbulent flux profiles of momentum and heat at Cabauw are displayed along with the corresponding median local Obukhov length. The median is displayed to reduce the influence of very large values of L^{-1} when $u_* << 1$ m s^{-1}.

Model	Observed input parameters	Internally computed parameters
MOST (local z_0)	U_{10}, z_0, $Ri_{B,surf}$	L_{surf}, ψ_m
Local similarity	U_{10}, τ_5, τ_{60}, τ_{100}, τ_{180} L_{surf}, L_{60}, L_{100}, L_{180}	ψ_m
Gryning	U_{10}, z_0, $Ri_{B,surf}$, G	u_*, L_{surf}, h_{ABL}, ϕ_m, ψ_m
Ekman layer	U_{10}, τ_{100}, G	u_G, v_G, γ
Two-layer	U_{10}, $Ri_{B,surf}$, G	z_0, u_*, L_{surf}, h_{ASL}, α, u_G v_G, ϕ_m, ψ_m, γ
MOST (effective z_0)	U_{10}, $Ri_{B,surf}$, G	z_0, L_{surf}, ψ_m

Table 3.2: Summary of models considered in this analysis, including observed and prescribed input parameters as well as internally computed parameters. Numbered subscripts denote the height of the particular parameter.

As seen in Fig. 3.2 (a), the momentum fluxes do not decrease monotonically with altitude, as would be expected on average for horizontally homogeneous conditions. Rather, the fluxes at 5 m are lower than those at 60 m across all stability classes. The effect of IBLs at Cabauw is evident in the kinematic heat flux profile for unstable and weakly stable conditions (Fig. 3.2 (b)) but not for the other stability classes, which show a monotonic decrease in magnitude with altitude. The lower momentum flux near the surface results in lower magnitudes of the surface Obukhov length (Fig. 3.2 (c)). Consequently, the use of a surface flux-derived Obukhov length in the logarithmic wind-speed profile (Eq. 3.3) will overestimate stability aloft in stable conditions. To correct for the influence of IBLs in extrapolating wind speeds using Eq. 3.3, we iteratively solve for the 'bulk' Obukhov length at the surface, L_{surf}, using the surface bulk Richardson number, $Ri_{B,surf}$, measured between 10 m and z_0,

$$Ri_{B,surf} = \left(\frac{10}{L_{surf}}\right) \frac{\ln\left(\frac{10}{z_0}\right) - \psi_H\left(\frac{10}{L_{surf}}, \frac{z_0}{L_{surf}}\right)}{\left[\ln\left(\frac{10}{z_0}\right) - \psi_M\left(\frac{10}{L_{surf}}, \frac{z_0}{L_{surf}}\right)\right]^2} \tag{3.16}$$

where ψ_H is the similarity function for heat, and 2-m temperatures are used as surface values. Using this approach, the Obukhov length is effectively 'tuned' to be compatible with the particular z_0 used. Numerous methods exist for determining z_0 by wind direction, with a large range of values depending on the method as shown in Chapter 2. Different choices of z_0 result in substantially different extrapolated wind-speed

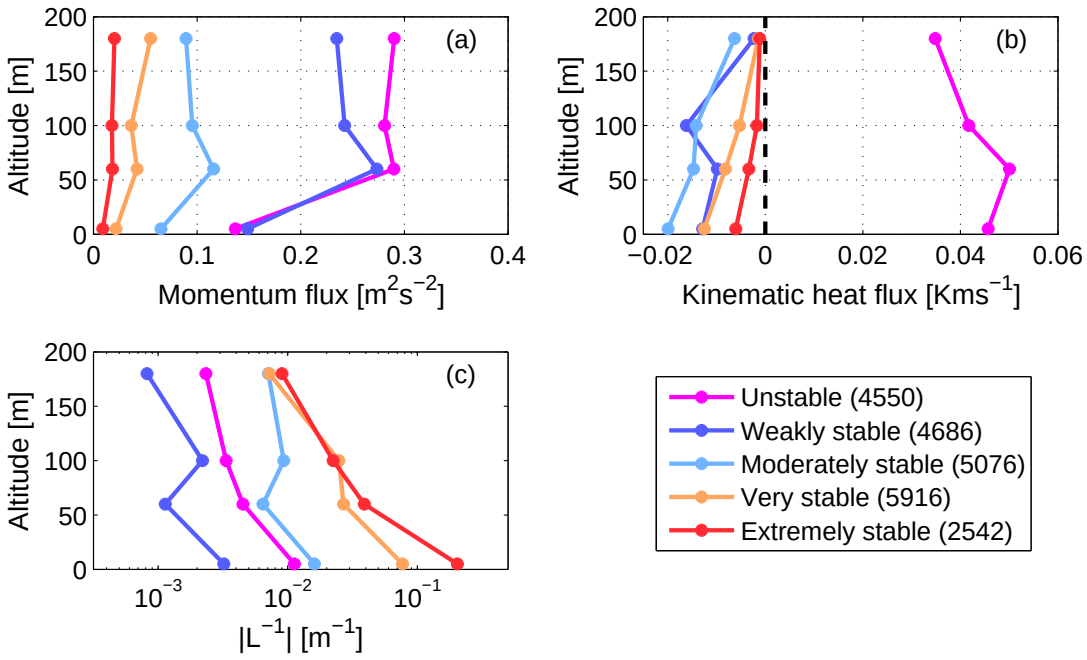

Figure 3.2: Vertical profiles of: (a) mean turbulent momentum flux, (b) mean turbulent kinematic heat flux, and (c) absolute values of the median L^{-1} for the stability classes described in Table 1.

profiles, and we found that using the 'Profile, 10-200 m' z_0 formulation provided accurate wind-speed profiles up to 80 m for the weakly stable case (i.e. conditions in which the assumptions of MOST are expected to be valid). These z_0 values are thus used in this analysis.

A comparison of the surface-flux measured L to the bulk-derived L_{surf} is shown in Fig. 3.3 for stable conditions. As shown therein, the bulk-derived approach generally results in larger values of L_{surf} (i.e. more neutral) compared to the surface-flux derived values, thus providing some correction for the influence of IBLs. Reasons for this correction were described in detail in Chapter 2. The populations of the two variables in Fig. 3.3 largely follow a line parallel to the 1:1 line and can therefore be connected by a multiplicative factor. An exception to this relationship occurs for low values of L_{surf} (i.e. very stable) in which the bulk-derived value is lower than the flux-measured value. This difference is due to the influence of the U_{10}^2 term in the denominator of Ri_B (Eq. 3.13) which becomes small in conditions of strong stratification and surface decoupling.

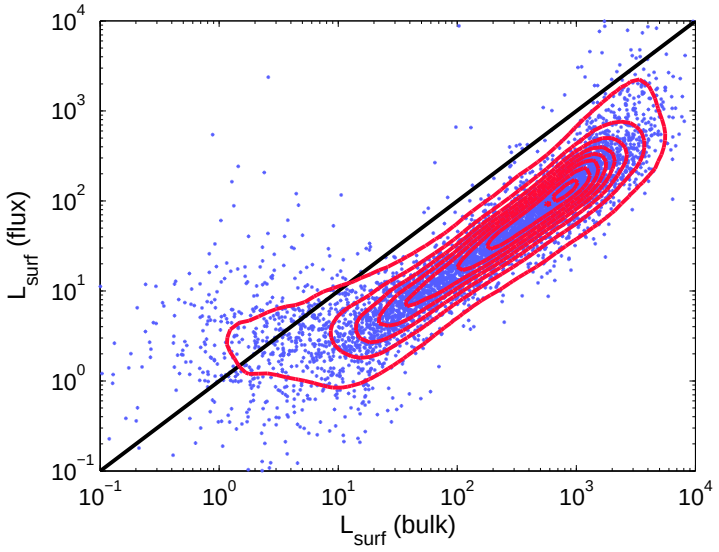

Figure 3.3: Scatter plot of surface flux-derived and bulk Richardson number-derived Obukhov lengths at 5 m. Also contoured are kernel density estimates of the joint probability density function (PDF) of the logarithm of these two variables.

This bulk-derived L_{surf} and the z_0 values based on local land-use maps are used to extrapolate 10-m wind speeds using MOST. Specifically, we extrapolate 10-m winds to a height z by taking the ratio of Eq. 3.3 at z and Eq. 3.3 at 10 m,

$$\bar{U}(z) = \bar{U}_{10} \frac{\left[\ln\left(\frac{z}{z_0}\right) - \psi_m\left(\frac{z}{L_{surf}}, \frac{z_0}{L_{surf}}\right)\right]}{\left[\ln\left(\frac{10}{z_0}\right) - \psi_m\left(\frac{10}{L_{surf}}, \frac{z_0}{L_{surf}}\right)\right]} \tag{3.17}$$

3.4.2 Local similarity

For the local similarity model, momentum fluxes and flux-derived Obukhov lengths measured at 5 m, 60 m, 100 m, and 180 m are linearly interpolated to the mid-points between wind measurement altitudes (i.e. 15 m, 30 m, 60 m, 100 m, and 170 m). Wind speeds at 20 m are calculated from 10-m wind speeds and 15-m fluxes, after which 40-m wind speeds are calculated from 20-m wind speeds and 30-m fluxes, and so on. For all cases, we use the Beljaars and Holtslag (1991) similarity function (Eq. 3.14) for locally stable conditions. For locally unstable conditions we use,

$$\psi_M(\zeta) = \frac{\pi}{2} - 2\arctan(x) + \log\frac{(1+x)^2(1+x^2)}{8}, \tag{3.18}$$

with $x = (1 - 16\zeta)^{1/4}$.

3.4.3 Gryning Model

For the Gryning model, the z_0 and L_{surf} values determined for MOST (local z_0) are used. The remaining parameters h_{ABL} and L_{MBL} are parametrized using the same approach in Pena et al. (2010); specifically, h_{ABL} takes the form (Tennekes, 1973),

$$h_{ABL} = C\frac{u_*}{f} \tag{3.19}$$

where C is a constant. Different values of C are used based on the surface Obukhov length (Pena et al., 2010). The L_{MBL} value is determined by equating the Gryning wind-speed profile (Eq. 3.8) at $z = h_{ABL}$ to the geostrophic wind as expressed by the geostrophic drag law,

$$G = \frac{u_*}{\kappa}\sqrt{\left[\ln\left(\frac{u_*}{f z_0}\right) - A\right]^2 + B^2}. \tag{3.20}$$

Different values of A and B are used based on the surface Obukhov length (Pena et al., 2010).

3.4.4 Ekman layer model

For the Ekman layer model, a bottom boundary condition of 10 m (i.e. $z_T = 10$ m, $u_{BC} = u_{10}$, $v_{BC} = v_{10}$ in Eq. 3.9) is used to be consistent with the other extrapolation approaches. Appropriate use of the Ekman layer model requires that the geostrophic wind is rotated 45^o to the surface wind vector (Fig. 3.1). Since the observed 10-m and geostrophic winds are not in fact generally separated by this angle, we define an 'effective' geostrophic wind vector with the same magnitude of the observed surface geostrophic wind vector but rotated appropriately. We parametrize the diffusivity coefficient K_m based on momentum flux measurements at 100 m (i.e. $K_m = C\tau/(\rho_o f)$, with C a constant), assuming that flux data at 100 m best represent atmospheric conditions in the bottom 200 m of the ABL. It was found that a value of $C = 4$ x 10^{-3} provided the most accurate wind profiles in the higher stability regimes (in which

the Ekman layer model is expected to be most valid) and is used in this analysis. The Ekman layer model breaks down when $G < U_{10}$, which occurs in 2.3 % of the data. These data are excluded from analysis.

3.4.5 Two-layer model

For the two-layer model, U_{10}, $Ri_{B,surf}$ and G are input parameters, while the remaining five parameters (z_0, u_*, L_{surf}, h_{ASL}, and α) are solved iteratively using the following system of equations: Eqs. 3.3 and 3.16 at 10 m, Eqs. 3.11 - 3.12, and a final equation describing h_{ASL} as a function of the other parameters. Zilitinkevich (1975) applied Rossby similarity theory in stable conditions to derive an expression for h_{ABL} as a function of the dimensionless parameter $\mu = u_*/(fL)$,

$$h_{ABL} = \frac{au_*}{f} F(\mu), \tag{3.21}$$

where a is a constant, au_*/f is the height of the ABL in neutral conditions, and $F(\mu)$ is a function that must be specified. We assume that h_{ASL} scales likewise in stable conditions and use the same functional form as in Zilitinkevich (1975). Numerical experiments carried out with a single-column momentum budget model assuming horizontal homogeneity and no advection suggest the following expression for h_{ASL},

$$h_{ASL} = \frac{bu_*}{f} F(\mu), \tag{3.22}$$

with $b = 0.0127$ and $F = (1 + 0.011\mu + 0.022\mu^2)^{-1/4}$. Probability density functions (PDFs) of h_{ASL} as determined from Eq. 3.22 and using the Cabauw data are shown in Fig. 3.4 for the different stability classes. In the weakly stable case, there is a broad range of h_{ASL} values extending up to roughly 120 m; low values correspond to weak winds and high values correspond to strong winds. In the extremely stable case the range is much narrower, with values extending up to roughly 40 m. The peak in the PDF at about 5 m corresponds to frequent periods of strongly stable stratification, for example during summer nights.

Having determined the complete set of two-layer model parameters, we first extrapolate the 10-m wind speeds up to h_{ASL} using the logarithmic wind-speed equation (Eq. 3.17). The wind speed at h_{ASL} then becomes the boundary condition for the

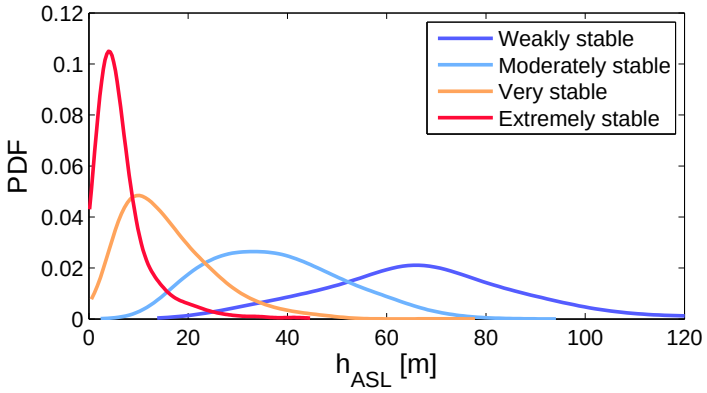

Figure 3.4: PDFs of h_{ASL} for different stability classes, as determined from Eq. 3.22

Ekman layer equations (Eq. 3.9) that are applied above h_{ASL}. The constant diffusivity coefficient K_m for the Ekman layer is determined using the MOST formulation evaluated at h_{ASL},

$$K_m(h_{ASL}) = \frac{u_* \kappa h_{ASL}}{\phi_m \left(\frac{h_{ASL}}{L_{surf}} \right)}. \tag{3.23}$$

As was done for the Ekman layer model, we determine an 'effective' geostrophic wind vector that has the same magnitude of the observed surface geostrophic wind and is rotated by the angle α (as determined from the two-layer system of equations) to the 10-m wind vector. Similar to the Ekman layer model, cases in which $G < U_{10}$ are excluded from analysis. For cases in which $h_{ASL} < 10$ m (18.8 % of the cases), the two-layer system effectively reduces to an Ekman layer model for a 10 m to 200 m extrapolation. For these cases, the MOST-derived form of K_m (Eq. 3.23) is not appropriate for modelling the flow aloft, and in particular results in excessively low values of K_m due to the large magnitude of the ϕ_m term. For these cases, a formulation for K_m is used based on u_* as determined from the two-layer system of equations. It was found that $K_m = 0.0017 u_*^2 / f$ provided the most accurate results in extremely stable conditions and is used here.

3.4.6 MOST (effective z_0)

The final model is equivalent to the MOST (local z_0) model but uses the z_0 and L_{surf} values determined from the two-layer system. We include this model to provide a

direct comparison of the MOST and two-layer models using the same parameters.

3.5 Results

We will now assess the performance of the different wind profile models described in the previous section under different stability conditions. Each wind-speed profile model uses different sets of data which are subject to data gaps that occur at different times and altitudes. To make meaningful comparisons between models, only time intervals for which the required observational data is available for all the models are considered. Since the Gryning model is invalid when $z > h_{ABL}$, we limit the Gryning wind profile up to 80 m in very stable conditions and up to 20 m in extremely stable conditions, while the remaining wind-profile models are extrapolated up to 200 m across all stability classes.

In Fig. 3.5, observed and modelled mean wind-speed profiles (normalized to 10 m winds) under different stability classes are compared. In general, lower wind-speed shear is observed in the low stability ranges and higher wind-speed shear is observed in the higher stability ranges. In the extremely stable range, the mean wind speeds at 140 m and 200 m are close in value, reflecting frequent cases of maxima in the wind speed profile below 200 m. Most models under consideration are accurate up to 200 m in the weakly stable case, except for the Ekman layer model which due to high values of K_m tends to underestimate wind speeds. The MOST models tend to underestimate wind speeds at the higher altitudes. There is considerably higher divergence in the modelled profiles in moderately stable conditions (Fig. 3.5 (b)). Both MOST models and the Gryning model underestimate wind speeds, while the local similarity model tends to slightly overestimate wind speeds. Both the Ekman layer and two-layer models are accurate at all altitudes. Similar results are found for very stable conditions (Fig. 3.5 (c)), apart from the local similarity model that tends to underestimate wind speeds at higher altitudes. The breakdown of MOST is evident in the extremely stable case (Fig. 3.5 (d)), in which both MOST models substantially overestimate wind speeds at higher altitudes. Local similarity is accurate up to 50 m but underestimates wind speeds at higher altitudes. The two-layer and Ekman layer models slightly overestimate wind speeds at lower altitudes and slightly underestimate wind speeds at higher altitudes, though both models still accurately account for the general shape of the observed wind-speed profile.

Box plots of the relative difference between modelled and observed winds (i.e.

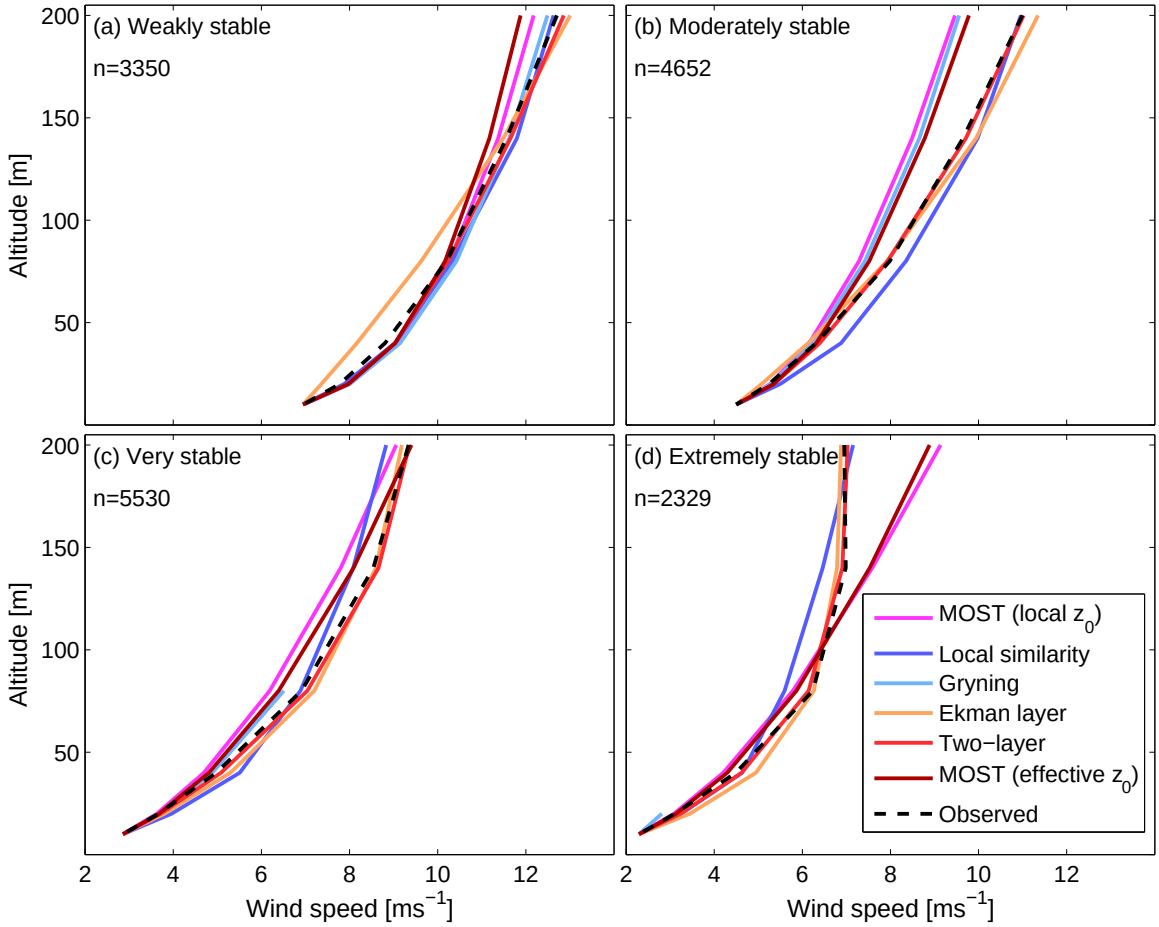

Figure 3.5: Modelled and observed mean wind-speed profiles for the different stability classes. The letter 'n' denotes the number of values included in the mean.

$(U_{mod} - U_{obs})/U_{obs})$ at different altitudes and stability classes are shown in Fig. 3.6. In general, the spread of the model predictions around the observed wind speeds increases with stability and altitude. At lower altitudes and low stability (i.e. upper-left quadrant in Fig. 3.6), the spread is relatively comparable between models, apart from the Ekman layer model which shows the highest spread. A similar trend is observed at lower altitudes and high stability (i.e. upper-right quadrant in Fig. 3.6), with the MOST (local z_0) model generally showing the least spread. At higher altitudes and low stability (i.e. lower-left quadrant in Fig. 3.6), the Ekman layer model shows the most spread while the other models have comparable spread. At higher altitudes and extreme stability, the MOST models show the most spread while the remaining

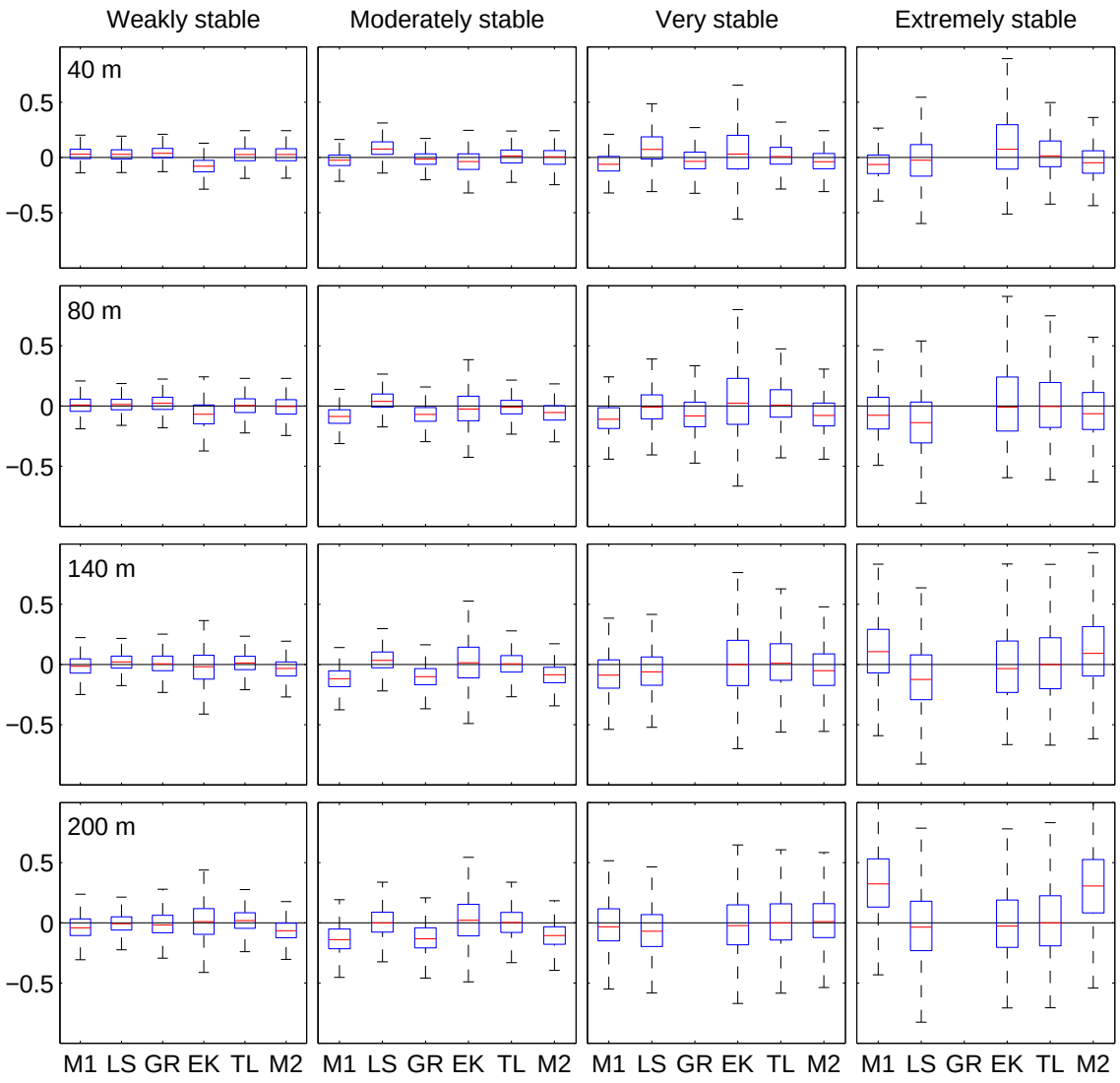

Figure 3.6: Box plots of the relative difference between modelled and observed winds (i.e. $(U_{mod} - U_{obs})/U_{obs}$) at different altitudes (rows) and stability classes (columns). The red lines show the mean values, blue boxes show the interquartile range, and black lines show the total range excluding outliers. Acronyms for the different models are as follows: M1 - MOST (local z_0), LS - local similarity, GR - Gryning, EK - Ekman layer, TL - two layer, M2 - MOST (effective z_0).

models show comparable spread.

Modelled and observed mean wind-speed profiles for cases in which an LLJ is observed are shown in Fig. 3.7. We identify an LLJ event when either the 10-min averaged 80 m or 140 m wind speeds are at least 10 % greater than the 200 m wind

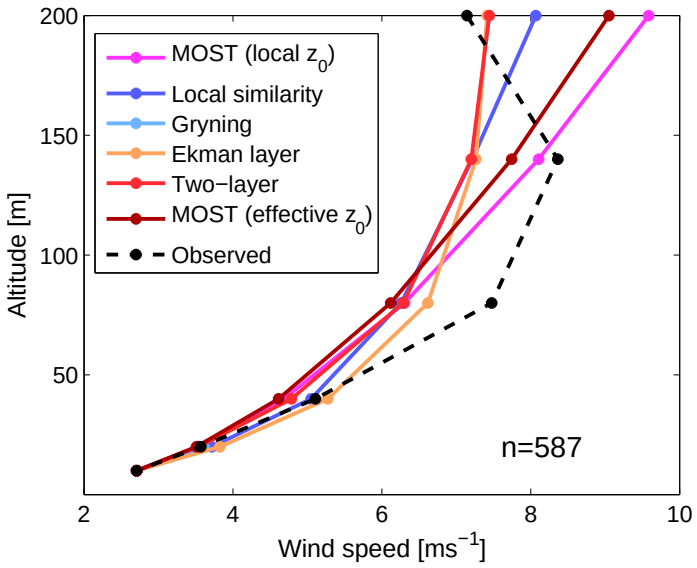

Figure 3.7: Modelled and observed mean wind-speed profiles for cases in which an LLJ is observed.

speed. As shown in Fig. 3.7, none of the models are able to accurately model the wind profile in the presence of pronounced LLJs. Similarity-based models are by construction unable to do so, as these cannot model a decrease in wind speed with altitude. The Ekman layer and two-layer models (which can model a decrease in wind speed with altitude) tend to underestimate wind shear and on average do not model a LLJ. Furthermore, both the Ekman layer and two-layer models are equilibrium models (i.e. no time dependence) whereas the LLJ is a time-dependent phenomenon, so the inability of these models to accurately account for the LLJ is expected.

3.6 Discussion

This analysis has demonstrated that the two-layer model results in wind-speed profiles that are of similar accuracy to other models in conditions of weakly stable stratification but become substantially better as the stability increases. Local similarity was accurate in all but the extremely stable regime and was the most data-intensive of all the models, requiring flux data at multiple altitudes. Such data are rarely available in the field, and thus the practical use of the local similarity model is limited. Though the Gryning model showed some improvement over the MOST (local z_0) model, its

limited altitude range of applicability limits its practical use in very to extremely stable conditions. The two-layer model required only a measure of the geostrophic wind (readily available through surface pressure observations) and a measure of surface stability. Among all the models, the two-layer model provided the best balance of low bias, low variance, and minimal input data for the entire stability range.

The different approaches in determining z_0 used in this analysis emphasize the role of z_0 more as a tunable boundary-condition parameter than a value with an unambiguous physical meaning. For the MOST (local z_0) model, we used z_0 values based on local land-use data to get accurate results for the wind profile at low altitudes. As a consequence, the model was inaccurate in the high stability ranges and at higher altitudes. Had we instead used regional z_0 values, accuracy at higher altitudes would have improved, but accuracy at lower altitudes would have decreased. For the two-layer model, z_0 values were solved within the system of equations with knowledge only of the 10-m wind speed, geostrophic wind speed and surface stability. No explicit relation between z_0 and wind direction was required, in contrast to conventional land-use based z_0 approaches (e.g. Verkaik and Holtslag, 2007).

Despite its improved accuracy relative to other models, the two-layer model remains a highly-idealized representation of lower-ABL physics. The forms $K_m = C\tau_{100}/(\rho_0 f)$ used for the Ekman layer model and $K_m = Cu_*^2/f$ used for the high stability limit of the two-layer model are rather simplified and contribute to the large scatter in model results, particularly in the higher stability regimes in which $u_*^2 << 1$ m^2 s^{-2}. More comprehensive forms of K_m (e.g. a function of $F(\mu)$ as in Rossby similarity theory) would likely lead to improved accuracy in the wind profiles. The limit of accuracy of the two-layer model under these improved parametrizations can be explored by comparing its results to a single-column momentum budget model which uses more comprehensive representations of ABL turbulence (though advection is still neglected). More detailed and physically-appropriate parametrizations for K_m should result in more accurate wind-speed profiles. Such a comparison will be the subject of future studies.

Another limitation of the two-layer and Ekman layer models was the frequent inconsistencies between surface pressure-derived geostrophic-wind data and tower data. For example, for unstable conditions with $U_{200} > 10$ m s^{-1} (for which h_{ASL} should be near or above 200 m), in 26.5 % of the observations the surface geostrophic-wind speed was less than the wind speed at 200 m. In this study, we assumed that the geostrophic winds were constant with altitude, neglecting the possibility of baroclinic

conditions in which geostrophic wind speeds at 200 m may have differed from those at the surface by several metres per second. The use of surface temperature measurements along with pressure measurements to get estimates of both the surface pressure-gradient force *and* the temperature gradient would allow for a baroclinic correction to these models. Alternatively, the use of pressure-level winds from global or regional models at appropriate altitudes would also provide a better representation of the geostrophic flow above the surface.

All models considered in this analysis are based on equilibrium or steady-state conditions. This is a reasonable approximation in the unstable, neutral and weakly stable ABLs in which the ABL adjustment timescales are short (on the order of an hour or less) (Mahrt, 2014). However, the steady-state assumption breaks down for the moderate to extremely stable ABLs. The formation and evolution of the low-level jet at sunset is one striking example. Over the course of the night, inertial oscillations can cause wind vectors aloft to oscillate around their equilibrium value with an amplitude equal to the degree of departure from equilibrium around the moment of surface decoupling (Van de Wiel et al., 2010). In some cases, the magnitude of the oscillation can be several metres per second. As shown in this study, the equilibrium two-layer model was not accurate in cases of LLJs. Time dependence can be incorporated into the two-layer approach by retaining the time dependence in the idealized force-balance equation (e.g. Van de Wiel et al., 2010). Future studies will assess the ability of the two-layer approach to accurately model the evolution of the LLJ under such conditions.

3.7 Conclusions

We have considered the accuracy of various wind-speed profile models up to 200 m in stable conditions using meteorological data from the 213 m tower at Cabauw. The logarithmic wind-speed profile (based on Monin-Obukhov similarity theory) was found to be reasonably accurate up to moderately stable conditions but became increasingly inaccurate for more stable stratification due to the surface layer becoming shallower. Local similarity-based profiles showed considerable improvement across all stability ranges, but were substantially more data-intensive. A fundamental limitation of any models based on similarity theory is that they cannot account for the influence of the Coriolis force under strong stability and weak turbulence. The Ekman layer model based on fluxes at 100 m was shown to be more accurate than similarity approaches

in the higher stability range. The two-layer MOST-Ekman model provided the best balance of low bias and variance for the entire stability range, and required only the geostrophic wind and surface bulk Richardson number as input parameters. These results present a viable case for the use of a two-layer model in wind energy resource assessment and forecasting. A comparison of the two-layer model to models using more physically appropriate and comprehensive turbulence parametrizations will be the subject of the next chapter.

Chapter 4

The extrapolation of near-surface wind speeds under stable stratification using an equilibrium-based single-column model approach

The contents of this chapter are based on the following paper:

Optis, M., A. Monahan (2015). 'The extrapolation of near-surface wind speeds under stable stratification using an equilibrium-based single-column model approach'. *Journal of Applied Meteorology and Climatology*, To be submitted.

4.1 Introduction

4.1.1 Idealized modelling of the stable boundary layer

The modelling of the stable boundary layer (SBL) continues to be a challenge (Mahrt, 2014) due to the presence of weak or almost collapsed turbulence and, consequently, the influence of a range of other processes (e.g. intermittent turbulence (Poulos et al., 2002), gravity waves (Mahrt, 1998), baroclinicity (Mahrt, 1998), surface heterogeneity (Verkaik and Holtslag, 2007), thin and 'upside-down' boundary layers (Mahrt

and Vickers, 2002), inertial oscillations (Baas et al., 2012), and low-level jets (LLJs) (Van de Wiel et al., 2010)). Research on the SBL has focused mainly on the representation of turbulence given the high sensitivity of atmospheric models to different parameterization schemes (ECMWF, 2006; Beljaars and Viterbo, 1999). Turbulence parameterizations are generally determined through a combination of field measurements (e.g. Beljaars and Holtslag 1991; Persson et al. 2002; Poulos et al. 2002) and modelling experiments (e.g. flux-gradient relationship analysis, 1D and 3D atmospheric models). Within the surface layer (SL), Monin-Obukhov similarity theory (MOST) is an accurate method to relate turbulent fluxes to properties of the mean flow (Monin and Obukhov, 1954). Above the SL in the SBL (where MOST does not apply), single-column models (SCMs) are often used to formulate or evaluate a turbulence parameterization scheme. These models are advantageous due to their low computational requirements and the flexibility in which processes and parameterizations are included (e.g. turbulence, radiation, entrainment, land surface characteristics, etc.). The complexity of an SCM can vary from models that incorporate the complete physics of a 3D model to highly idealized representations that consider only the momentum and temperature budgets.

There is a growing body of research using SCMs to study turbulence in the SBL (e.g. Cuxart et al. 2006; Edwards et al. 2006; Weng and Taylor 2006; Baas et al. 2010; Sterk et al. 2013; Bosveld et al. 2014b; Sorbjan 2014). The most comprehensive study has been the Global energy and water cycle experiment Atmospheric Boundary-Layer Study (GABLS), a series of comparisons between both operational and research-based atmospheric models focusing mainly on the representation of turbulence in the SBL (Holtslag, 2014). The first phase of the experiment (GABLS1) compared 19 SCMs to large-eddy simulations (LES) using a specified surface temperature cooling rate and constant geostrophic wind representing moderately stable conditions (Cuxart et al., 2006). The second phase (GABLS2) compared the representation of the diurnal cycle for 30 different SCMs using a prescribed geostrophic wind speed and surface temperature (Svensson et al., 2011). The third phase (GABLS3) focused on the representation of the diurnal cycle for 19 different SCMs using observations over a 24-hour period from the Cabauw meteorological tower in the Netherlands (Bosveld et al., 2014b). These studies demonstrated a broad range of results depending on the turbulence scheme, including large variations in the degree of turbulent mixing, surface wind speeds, temperature and turbulent fluxes, the onset of the evening and morning transitions, the evolution of the inertial oscillation, and the amplitude and

altitude of the LLJ. The tendency to over- or underestimate turbulent mixing was related mainly to the tunable constants used to determine mixing length and stability functions.

An accurate SCM simulation of the observed SBL is difficult due to the influence of 3D processes (e.g. momentum and temperature advection, baroclinic effects, internal boundary layers (IBLs)). To facilitate comparison between SCMs, Bosveld et al. (2014a) prescribed advective tendencies as piecewise constant functions as well as a geostrophic wind vector profile based on simulations from a mesoscale model. Baas et al. (2010) demonstrated that compositing SCM results over 7 LLJ events with comparable external forcings averaged-out the effects of advective tendencies, facilitating comparison with similarly composited observations.

4.1.2 Wind energy context

Turbulence parameterization in the SBL is of particular importance in the field of wind energy meteorology. The accurate modelling of the wind speed profile across altitudes swept out by a wind turbine blade (the 'wind power altitude range' between roughly 30-200 m) is important for preliminary resource assessments and forecasting of the wind resource. As wind power varies with the cube of wind speed, small errors in wind speed can lead to large errors in wind power. Conventional approaches to estimating wind speeds within the wind power altitude range have involved the extrapolation of near-surface (e.g. 10 m) wind speeds using simplified equilibrium (i.e. no time dependence) approaches such as the power law and logarithmic wind speed profile (Lange and Focken, 2005; Emeis, 2013). Such approaches have been shown to break down under stable stratification (demonstrated in in Chapter 2) and improved accuracy has been found by using idealized but more physically appropriate descriptions of SBL physics (e.g. two-layer MOST-Ekman model demonstrated in Chapter 3).

Time-evolving models have recently been adopted for wind resource assessment and forecasting, most notably the Weather and Research Forecasting (WRF) mesoscale model. The WRF model offers considerable flexibility given its ability to operate in both 3D and SCM modes, a broad range of available resolutions (e.g. horizontal range of about 0.5-100 km) and physics schemes (e.g. 7 boundary layer schemes with the ability to modify parameters), and the ability to use both idealized and observed external forcings (Skamarock et al., 2008). Several studies have used the 3D WRF

model for purposes ranging from mesoscale to microscale resource assessments, wind farm siting, predicting ramp events, and turbine spacing (e.g. Storm et al. 2009, 2010; Floors et al. 2013; Zhang et al. 2013; Nunalee and Basu 2014; Yang et al. 2014). Several studies have specifically focused on the sensitivity of wind power simulations to the choice of turbulence closure scheme (e.g Shimada et al. 2011; Carvalho et al. 2012, 2014; Deppe et al. 2013; Draxl et al. 2014; Marjanovic et al. 2014). These studies have shown large variability in near surface wind profiles dependent on the turbulence scheme. In general, turbulence schemes that incorporate non-local transport are most accurate in unstable conditions, and schemes biased towards low turbulence levels perform better in stable conditions. However, the relative performance of turbulence schemes tends to vary with location. To our knowledge, the SCM version of WRF has not been used for wind energy meteorology purposes. An SCM approach is potentially advantageous given the high computational requirements of a 3D model.

Another advantage of an SCM approach (in contrast to 3D models) is the ability to specify lower boundary conditions (e.g. wind speeds, temperature, turbulent fluxes, etc.) at a given altitude above the surface (e.g. 10 m) without needing to specify conditions at the surface itself. Such an approach is particularly appealing in the context of wind energy meteorology, as near-surface measurements of wind speeds are common in initial resource assessments. This approach in particular avoids the need to specify roughness lengths for momentum and temperature, which in Chapter 2 were shown to be poorly constrained parameters to which the wind profile is highly sensitive. Furthermore, lower boundary values of temperature or the turbulent temperature flux avoid the need to specify a SL scheme, generally required in atmopsheric models to determine turbulent fluxes at the surface. A lower boundary above the surface also helps to mitigate the influence of horizontal heterogeneity in surface roughness and the development of IBLs (see Chapter 2). To our knowledge, the use of an SCM with a lower boundary above the surface has not been explored in any context.

4.1.3 Motivation and intent of study

In Chapter 2, we demonstrated the breakdown of MOST (and various MOST-based improvements) for extrapolating wind speeds aloft in stable stratification. In Chapter 3, we demonstrated improved performance over MOST using a two-layer model. We

now consider the extent to which an SCM approach can provide improved accuracy compared to the two-layer model. The SCM considered in this study is highly idealized, including only the momentum and temperature budget equations and requiring the specification only of the geostrophic wind vector, the 10 m wind vector (lower bound) and the 5-m turbulent temperature flux. We consider composite results over a large (10 year) data set in order to mitigate the effects of advective tendencies (as in Baas et al. (2010)). We also consider a range of turbulence closure schemes identified in the GABLS3 study (Bosveld et al., 2014b; Kleczek et al., 2014). In Sect. 4.2 we describe the data sources. The model set-up including the different turbulence schemes considered is provided in Sect 4.3. In Sect. 4.4 we compare model results to observations over a range of stability classes. The influence of baroclinicity at Cabauw, methods to account for the resulting thermal wind, and the effect on the modelled wind profile are explored in Sect. 4.5. A discussion is provided in Sect. 4.6 and conclusions in Sect. 4.7.

4.2 Data sources

Data for this analysis were taken from a range of sources. Most of the data were obtained from the Cabauw meteorological tower in the Netherlands, operated by the Royal Netherlands Meteorological Institute (KNMI). Measurements of meteorological variables at 10-min resolution were obtained from January 1 2001 to December 31 2010 (these data are available at http://www.cesar-database.nl). Wind speed and direction measurements are available at 10 m, 20 m, 40 m, 80 m, 140 m, and 200 m, and temperature measurements are available at these altitudes as well as 2 m. Turbulent temperature flux data at 5 m at 10-min resolution were also provided. Surface pressure measurements at 10-min resolution were used to calculate the potential temperature at different heights. Turbulent momentum flux data at 10-min resolution were provided for the period July 2007 - June 2008 at altitudes of 5 m, 60 m, 100 m, and 180 m. Two different data sets were used to estimate the geostrophic wind. The first dataset was provided by KNMI and was derived from 1-h averaged surface pressure measurements from weather stations near Cabauw using a 2nd order polynomial fit. The second dataset was the 6-h averaged wind vector data at 800 hPa taken from the European Centre for Medium-Range Weather Forecasts (ECMWF) ERA-interim global atmospheric reanalysis (available at http://apps.ecmwf.int/datasets). These data were linearly interpolated horizontally to the location of Cabauw. To es-

timate the thermal wind, near-surface temperature measurements from 2001-2010 in 1-h averages were taken from nearby weather stations operated by KNMI (data are avaliable at http://www.knmi.nl/klimatologie/uurgegevens). All data used in this analysis were linearly interpolated to 10-min resolution unless otherwise indicated. We consider 10-min averaged data once every 30 minutes (e.g. 1200 UTC, 1230 UTC, 1300 UTC etc.) to reduce computational requirements while still obtaining a comprehensive sampling of conditions at Cabauw.

4.3 Model setup

4.3.1 SCM governing equations and turbulence schemes

We consider an idealized, horizontally homogeneous atmospheric boundary layer (ABL) with no radiative or moist processes, resulting in the following eddy-averaged equations,

$$\frac{\partial u}{\partial t} = f(v - v_G) - \frac{\partial(\overline{u'w'})}{\partial z} \tag{4.1a}$$

$$\frac{\partial v}{\partial t} = -f(u - u_G) - \frac{\partial(\overline{v'w'})}{\partial z} \tag{4.1b}$$

$$\frac{\partial \theta}{\partial t} = -\frac{\partial(\overline{\theta'w'})}{\partial z} \tag{4.1c}$$

where u and v are the horizontal components of the wind vector, θ is the potential temperature, f is the Coriolis parameter, u_G and v_G are the components of the geostrophic wind, $\overline{u'w'}$ and $\overline{v'w'}$ are the horizontal components of the vertical turbulent momentum flux per unit mass, $\overline{\theta'w'}$ is the vertical turbulent temperature flux, and z is the height above the surface. For simplicity, the air density is assumed to be constant. The turbulent fluxes in Eq. 4.1 are parameterized as diffusion processes,

$$\overline{u'w'} = -K_m \frac{\partial u}{\partial z} \tag{4.2a}$$

$$\overline{v'w'} = -K_m \frac{\partial v}{\partial z} \tag{4.2b}$$

$$\overline{\theta'w'} = -K_h \frac{\partial \theta}{\partial z} \tag{4.2c}$$

where K_m and K_h are respectively the eddy diffusivities of momentum and temperature, which can be specified through a range of turbulence closure schemes classified by the closure order (Stull, 1988; Cuxart et al., 2006). For first-order closure, the diffusivities are expressed as,

$$K_m = l_m^2 \frac{\partial U}{\partial z} f_m \tag{4.3a}$$

$$K_h = l_m l_h \frac{\partial U}{\partial z} f_h \tag{4.3b}$$

where l_m and l_h are the mixing lengths for momentum and heat, respectively, and $\partial U/\partial z = \sqrt{(\partial u/\partial z)^2 + (\partial v/\partial z)^2}$ is the magnitude of the wind shear. The stability functions f_m and f_h are usually expressed in terms of the local Richardson number but are sometimes expressed using the non-dimensional MOST functions for momentum and temperature (i.e. $f_m(Ri) = \phi_m^{-2}(z/L)$ and $f_h(Ri) = \phi_h^{-2}(z/L)$), where L is the Obukhov length. One commonly-used first-order parameterization that makes use of MOST-based stability functions is derived beginning with the key equations of MOST and the Panofsky (1973) altitude-dependent form of $\tau/\rho = \sqrt{(\overline{u'w'})^2 + (\overline{v'w'})^2}$,

$$l_m = \kappa z \tag{4.4a}$$

$$\frac{\partial U}{\partial z} = \frac{u_*}{l_m}\phi_m \tag{4.4b}$$

$$\sqrt{\frac{\tau(z)}{\rho}} = u_* \left(1 - \frac{z}{h_{ABL}}\right)^{\alpha} \tag{4.4c}$$

with κ the von Karman constant, u_* the surface friction velocity, $\tau(z)/\rho$ the momentum flux per unit mass at altitude z, h_{ABL} the ABL height, and α a tunable constant. Combining Eqs. 4.4(a)-(c) with Eqs. 4.3(a)-(b) results in the following expressions for the diffusivities:

$$K_m = \frac{\kappa z u_*}{\phi_m}(1 - \frac{z}{h})^{2\alpha} \tag{4.5a}$$

$$K_h = \frac{\kappa z u_*}{\phi_h}(1 - \frac{z}{h})^{2\alpha} \tag{4.5b}$$

In 1.5 order closure schemes, the diffusivities are expressed in terms of the turbu-

lent kinetic energy (TKE),

$$K_m = c_m l_m f_m \sqrt{E} \tag{4.6a}$$

$$K_h = c_h l_h f_h \sqrt{E} \tag{4.6b}$$

where c_m and c_h are constants, and E is the TKE determined through the prognostic TKE budget (where we neglect TKE transport from pressure perturbations),

$$\frac{\partial E}{\partial t} = -\overline{u'w'}\frac{\partial u}{\partial z} - \overline{v'w'}\frac{\partial v}{\partial z} + \frac{g}{\theta}\overline{\theta'w'} - \frac{\partial}{\partial z}\left(\overline{E'w'}\right) - \epsilon \tag{4.7}$$

where g is the acceleration due to gravity. In Eq. 4.7, $\overline{E'w'}$ is the vertical turbulent flux of TKE, often expressed as a diffusion process,

$$\overline{E'w'} = -K_e \frac{\partial E}{\partial z} \tag{4.8}$$

with K_e the TKE diffusivity. The term ϵ in Eq. 4.7 is the dissipation rate, which in 1.5 TKE closure is parameterized according to,

$$\epsilon = \frac{c_d E^{3/2}}{l_d} \tag{4.9}$$

where c_d is a constant and l_d is the dissipation length scale (Stull, 1988; Garratt, 1994). Higher-order closure schemes make use of one or more additional prognostic equations for variables such as ϵ, the mixing lengths, and the vertical turbulent fluxes. The Mellor and Yamada (1982) formulation is one such scheme in which prognostic equations for the turbulent fluxes are related algebraically resulting in simplified expressions (Tables 4.1 and 4.2).

We consider a range of turbulence closure schemes based on the GABLS3 study, in which Bosveld et al. (2014b) considered 19 different SCMs from various organizations and Kleczek et al. (2014) considered 7 turbulence schemes within the WRF model. Limiting the order of schemes to 1.5 TKE closure (but including Mellor-Yamada), we identify and select for consideration in this study a total of 8 different turbulence closure schemes considered in Bosveld et al. (2014b) and Kleczek et al. (2014). These schemes are summarized in Table 4.1 with complete parameterizations provided in Table 4.2.

For the YSU scheme, we specify h_{ABL} as the altitude at which the momentum

flux reaches 5% of its surface value. In addition, we specify the Beljaars and Holtslag (1991) form of ϕ_m in light of the breakdown of the Businger et al. (1971) form used in Hong and Pan (1996). To facilitate calculations for the MYJ scheme, we replace the usual form of the mixing length limit,

$$\lambda = \beta \frac{\int_0^{h_{ABL}} |z| q da}{\int_0^{h_{ABL}} q dz} \tag{4.10}$$

with $q = \sqrt{2E}$ and β a constant, with the form $\lambda = a u_*/f$. Both representations of λ scale with h_{ABL}, so the substitution is not expected to result in significant changes to model results. For the UKMO scheme, Smith (1990) uses a value of λ that scales with h_{ABL}, but no equation is provided. We therefore assume the form $\lambda = a u_*/f$.

4.3.2 SCM numerical scheme and boundary conditions

We use an equilibrium approach in this analysis as is common in other SCM studies of the SBL (e.g. Weng and Taylor 2003, 2006; Cuxart et al. 2006; Sorbjan 2012, 2014). Such an approach allows for a more meaningful comparison to equilibrium-based extrapolation models such as the logarithmic and two-layer models discussed in Chapters 2-3. Properties of the stable boundary layer are generally time-evolving, so an equilibrium approach may be of limited accuracy when compared to observations, particularly in higher stability regimes. Using observed external parameters at a given point in time (specifically the geostrophic wind, 10-m wind, and 5-m turbulent temperature flux), we begin from a neutral wind profile and integrate Eqs. 4.1 (a)-(c) forward in time while keeping the external parameters constant. The goal of this approach is to reach a 'quasi-equilibrium' state in which the vertical wind profile and the vertical potential temperature gradient become constant in time in the lower ABL (i.e. below roughly 500 m). The potential temperature in the lower ABL does not reach equilibrium due to continued surface cooling. Previous studies have found that a period of 9 h was sufficient to reach quasi-equilibrium in moderately stable conditions (Beare et al., 2006; Cuxart et al., 2006; Sorbjan, 2014). We adopt the same time period in this analysis. Under very stable stratification, quasi-equilibrium is generally not reached due to low turbulent mixing and the generation of inertial oscillations (Sorbjan, 2014).

The initial neutral profile is solved by assuming equilibrium (i.e. $\partial u/\partial t = \partial v/\partial t = 0$) in Eqs. 4.1(a)-(b) and then solving the resulting set of ordinary differential equa-

Name/Organization	Abbreviation	Acronym	Order	Reference
Yonsei University	YSU	Y	1	Hong and Pan (1996)
Royal Netherlands Meteorological Institute	RACMO	R	1.5	Unden (2002)
Mellor-Yamada-Janjic	MYJ	M	2	Galperin et al. (1988); Janjic (2002)
Quasi-Normal Scale Elimination	QNSE	Q	1.5	Sukoriansky (2008)
UK Met Office	UKMO	U	1	Smith (1990)
Wageningen University	WUR	W	1	Duynkerke (1991)
European Centre for Medium-Range Weather Forecasts	ECMWF	E	1	ECMWF (2006)
Environment Canada	ECAN	C	1.5	Belair et al. (1999)

Table 4.1: Turbulence closure schemes considered in this study.

Scheme	Diffusivity	Mixing length	Constants and stability functions
YSU	$K_m = l_m u_* \phi_m^{-1}(1 - z/h_{ABL})^2$ $K_h = Pr^{-1} K_m$	$l_m = \kappa z$	$Pr = 1$; $\zeta = z/L$ $\phi_m = 1 + a\zeta + b\zeta(1 + c - d\zeta)\exp(-d\zeta)$ a=1; b=2/3; c=5; d=0.35
RACMO	$K_{m,h} = l_{m,h}\sqrt{E}$; $K_e = 2K_m$	$l_{m,h}^{-1} = (c_n \kappa z)^{-1} + \lambda^{-1} + s_{m,h}^{-1}$ $s_{m,h} = c_{m,h}\sqrt{E} N^{-1}$ $l_d = l_m$	$\lambda = 75$m; $c_d = c_0^{-2}$; $c_0 = 3.3$ $c_m = 0.8$; $c_h = 0.2$; $c_n = c_0^{-1/2}$; $N^2 = \frac{g}{\theta}\frac{\partial \theta}{\partial z}$
MYJ	$K_{m,h,e} = l_m q S_{m,h,e}$ $q^2 = 2E$ $G_m = (l_m q^{-1} S)^2$ $G_h = -(l_m q^{-1} N)^2$ $S^2 = \left(\frac{\partial u}{\partial z}\right)^2 + \left(\frac{\partial u}{\partial z}\right)^2$	$l_m^{-1} = (\kappa z)^{-1} + \lambda^{-1}$ $\lambda = a u_* / f$ $l_d = l_m$	$c_d = B_1^{-1}$; $a = 0.0063$; $A_1 = 0.660$; $A_2 = 0.657$; $B_1 = 11.9$; $B_2 = 7.23$; $C_1 = 8.31e-4$ $S_m = A_1(1 - 3C_1 - 6A_1 B_1^{-1} - 3A_2 G_h[(B_2 - 3A_2)(1 - 6A_1 B_1^{-1}) - 3C_1(B_2 + 6A_1)])/[(1 - 3A_2 G_h(6A_1 + B_2))(1 - 9A_1 A_2 G_h)]$ $S_h = A_2[1 - 6A_1 B_1^{-1}]/[1 - 3A_2 G_h(6A_1 + B_2)]$
QNSE	$K_{m,h} = c_2 \alpha_{m,h} l_m \sqrt{E}$ $K_e = K_m$	$l_m^{-1} = (\kappa z)^{-1} + \lambda^{-1} + l_N^{-1}$ $\lambda = 0.0063 u_* f^{-1}$ $l_N = 0.75\sqrt{E} N^{-1}$; $l_d = l_m$	$\alpha_m = (1 + 8Ri^2)(1 + 2.3Ri + 35Ri^2)^{-1}$ $\alpha_h = (1.4 - 0.01Ri + 1.29Ri^2)(1 + 2.344Ri + 19.8Ri^2)^{-1}$ $c_d = c_2^3$; $c_2 = 0.55$
UKMO	$K_m = {l_M}^2 \frac{\partial U}{\partial z} f_m$ $K_h = K_m$	$l_m^{-1} = (\kappa z)^{-1} + \lambda^{-1}$ $\lambda = 0.0063 u_* f^{-1}$	$f_m = \begin{cases} (1 - 5Ri)^2 & \text{if } 0 < Ri \leq 0.05 \\ \frac{1.6875}{1 + 40Ri} & \text{if } Ri > 0.05 \end{cases}$
WUR	$K_{m,h} = {l_M}^2 \frac{\partial U}{\partial z} \phi_m^{-1} \phi_{m,h}^{-1}$	$l_m = \kappa z$	$\phi_{m,h} = 1 + \beta_{m,h}\zeta(1 + \beta_{m,h}\zeta a^{-1})^{a-1}$ $\beta_m = 5$; $\beta_h = 7.5$; $a = 0.8$; $\zeta = zL^{-1}$
ECMWF	$K_{m,h} = {l_M}^2 \frac{\partial U}{\partial z} f_{m,h}$	$l_m^{-1} = (\kappa z)^{-1} + \lambda^{-1}$ $\lambda = 150$m	$f_m = \left[1 + 2bRi(1 + dRi)^{-1/2}\right]^{-1}$ $f_h = \left[1 + 2bRi(1 + dRi)^{1/2}\right]^{-1}$ $b = 5$; $d = 1$
ECAN	$K_m = c_n l_m \sqrt{E}$ $K_h = K_e = K_m$	$l_m^{-1} = [(\kappa z)^{-1} + \lambda^{-1}] f_m^{-1}$ $\lambda = 200m$	$f_m = (1 + 12Ri)^{-2}$; $l_d = l_m$; $c_d = c_n^4$ $c_n = 0.516$

Table 4.2: Complete parameterizations of turbulence closure schemes considered in this study.

tions using a boundary-value problem (BVP) solver in the MATLAB software package ('bvp4c', described at http://www.mathworks.com/help/matlab/ref/bvp4c.html). For this calculation, we specify a first-order closure scheme with a mixing length of the form $l_m^{-1} = (\kappa z)^{-1} + \lambda^{-1}$, with $\lambda = 70$ m. We specify an initial logarithmically-scaled vertical grid with 200 vertical levels to provide high near-surface resolution and an upper-altitude limit based on the magnitude of the geostrophic wind (Table 4.3). The BVP solver determines an optimal descretization on which a solution can be obtained. This discretization remains logarithmically scaled and generally contains between 200-400 levels. From the initial neutral profile, Eqs. 4.1(a)-(c) are integrated forward in time using a partial differential equation solver in the MATLAB software package ('pdepe', described at http://www.mathworks.com/help/matlab/ref/pdepe.html). The discretization from the initial neutral profile remain constant throughout the integration. We assume an initial potential temperature of 295 K at all levels, noting that the value of temperature (in contrast to the temperature profile) is arbitrary and has negligible influence in the denominators of the gradient Richardson number (used to determine stability in first order closure), the buoyancy production term in the TKE budget, and the Brunt-Vaisala frequency, N (Table 4.2).

We specify the observed 10-m wind vector and the 5-m temperature flux as lower boundary conditions at 10 m, noting that the use of lower altitude fluxes will slightly overestimate the degree of stable stratification. For TKE-based closure, we adopt the approach in Weng and Taylor (2003) and Weng and Taylor (2006) and specify a lower boundary condition on the TKE by assuming the vertical turbulent flux of TKE is negligible near the surface compared to TKE production and dissipation (Stull, 1988). With this assumption, the TKE at 10-m is in equilibrium (i.e. $\partial E/\partial t = 0$) and using Eq. 4.7 is calculated as,

$$E = \left[\frac{l_d}{c_d}\left(-\overline{u'w'}\frac{\partial u}{\partial z} - \overline{v'w'}\frac{\partial v}{\partial z} + \frac{g}{\theta}\overline{\theta'w'}\right)\right]^{2/3} \tag{4.11}$$

The TKE value at the lower boundary is therefore calculated based on lower boundary flux values that are computed internally. For upper boundary conditions, we specify the geostrophic wind vector and a constant potential temperature of 295 K. For TKE-based closure, we specify an upper-boundary value of zero for the vertical turbulent TKE flux.

Geostrophic wind speed range	Upper boundary for SCM model (m)
$G < 8$ ms^{-1}	1500
8 ms^{-1} $\leq G <$ 13 ms^{-1}	2000
13 ms^{-1} $\leq G <$ 20 ms^{-1}	2500
$G > 20$ ms^{-1}	3000

Table 4.3: Upper boundaries for the SCM, based on the magnitude of the geostrophic wind, G.

4.3.3 Two-layer model setup

The two-layer model (described in Chapter 3) consists of a MOST-based logarithmic wind speed profile applied within the SL and the Ekman equations applied above. Required observational data include the 10 m wind speed, the bulk Richardson number between 10 m and the surface (with the assumption that 2-m temperatures are representative of surface values), and the magnitude of the geostrophic wind. The height of the SL is computed internally based on the non-dimensional parameter $u_* f^{-1} L^{-1}$. Note that the two-layer model is strictly a wind vector extrapolation model and does not account for temperature profiles.

4.4 Results

Throughout this analysis, we consider model performance within different stability classes based on the observed bulk Richardson number determined between 200 m and the surface (Table 4.4),

$$Ri_B = \frac{g}{\theta_{avg}} \frac{z_{200}(\theta_{200} - \theta_{surf})}{U_{200}^2} \tag{4.12}$$

where θ_{avg} is the average potential temperature in the lower 200 m. We exclude data where both the 200-m wind speed and the geostrophic wind speed are less than 5 ms^{-1}. Under such conditions, flux-gradient relationships are known to perform poorly (Mahrt, 1998). Furthermore, SCM breakdown (i.e. failure to reach equilibrium) is frequent under such conditions given the weak turbulence. Finally, low wind-speed conditions are not of interest for wind power applications, so the accuracy of different wind-speed profile models under these conditions is not relevant in the present context. To make meaningful comparisons between models, only the time

intervals for which results are available for all models (including the two-layer model) are included in this analysis.

Stability class	Ri_B range
Weakly stable	$0 < Ri_B < 0.05$
Moderately stable	$0.05 < Ri_B < 0.15$
Very stable	$0.15 < Ri_B < 0.5$
Extremely stable	$Ri_B > 0.5$

Table 4.4: Stability classes considered in this analysis, based on Ri_B.

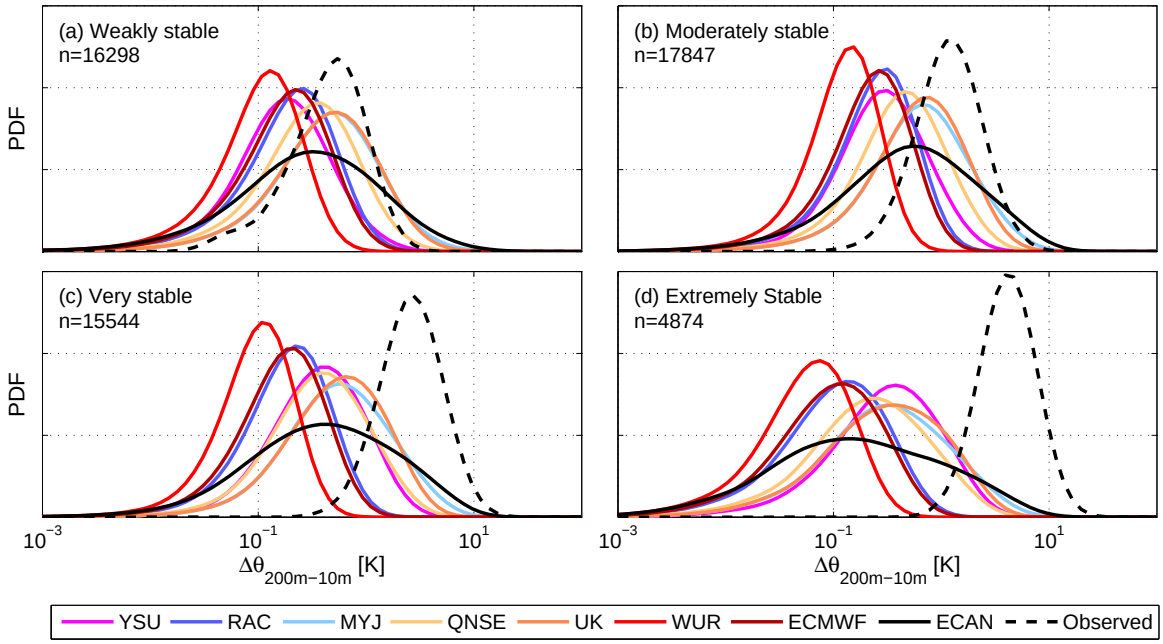

Figure 4.1: PDFs of modelled and observed $\Delta\theta_{200-10}$ for the different stability classes. The value 'n' denotes the number of datapoints used in calculating the mean.

In Fig. 4.1, we compare modelled and observed probability density functions (PDFs) of $\Delta\theta$ between 200-10 m (i.e. $\Delta\theta_{200-10}$) based on 10-min averaged temperature data. In general, all models tend to underestimate stratification (the bias for the MYJ and UKMO models in weakly stable conditions is difficult to distinguish given the logarithmic scaling of the x-axis). In weakly stable conditions (Fig. 4.1(a)), the MYJ, QNSE, and UKMO models (all with u_*-scaled λ values) provide the most accurate $\Delta\theta_{200-10}$ distributions. Conversely, the higher constant values of λ (i.e. 75 m

for RACMO, 150 m for ECMWF, no limit for WUR) are associated with greater tendencies to overestimate turbulent mixing and therefore underestimate stratification. The ECAN model - which uses the highest λ value (i.e. 200 m) but also uses a stability function biased towards low turbulence levels (Table 4.2) - demonstrates the broadest range of modelled stratifications. Figs. 4.1(b)-(d) demonstrate that as the observed stratification increases, the modelled stratifications tend to remain relatively unchanged. For several models, stratification is lowest in extremely stable conditions.

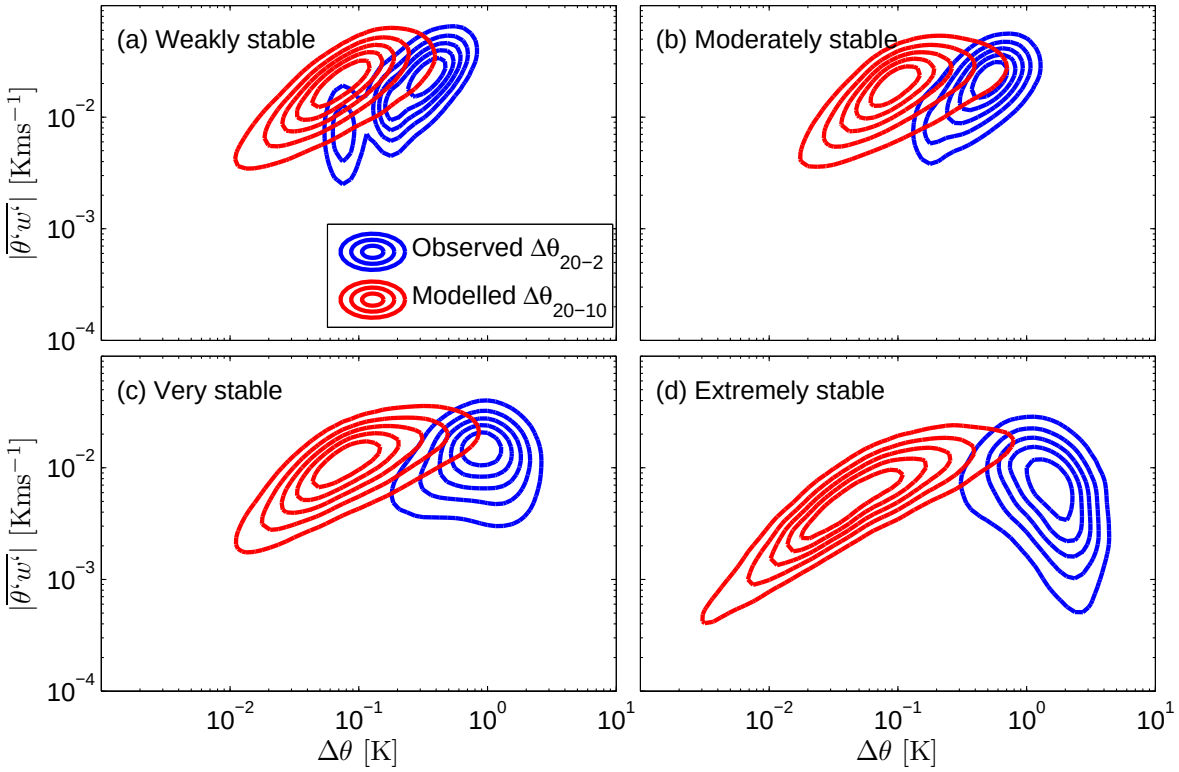

Figure 4.2: Joint PDFs of the observed 5-m turbulent temperature flux to both the observed and modelled (UKMO scheme) near-surface stratification for the different stability classes.

This bias towards low modelled stratifications can be related to the existence of two physically meaningful equilibrium solutions for the SBL for a fixed value of $\overline{\theta' w'}$ (van de Wiel et al., 2007; Gibbs et al., 2015). Specifically, a given value for $\overline{\theta' w'}$ can occur in relatively strong stratification (i.e. larger values of θ' and smaller values of w' leading to large values of $\Delta\theta$ across the ABL) and relatively weak stratification (i.e. smaller values of θ' and larger values of w' leading to small values of $\Delta\theta$ across

the ABL). We demonstrate the existence of these two equilibrium states in Fig. 4.2, showing joint PDFs of the magnitude of the observed 5-m turbulent temperature flux with both the observed and modelled (UKMO scheme) near-surface stratifications. We choose $\Delta\theta_{20-2}$ for the observed stratification and $\Delta\theta_{20-10}$ for the modelled stratification (noting that 10 m is the lowest model level). A larger altitude range for the observed stratification is used to reduce the number of inaccurate low $\Delta\theta$ values caused by temperature measurement uncertainty ($\pm$ 0.1 K). Note that the population centered around $\Delta\theta$ = 0.1 K in weakly stable conditions represents the lowest possible value for the observed $\Delta\theta$ due to measurement uncertainty. As seen in the figure, low magnitudes of the observed $\overline{\theta' w'}$ generally correspond to low values of the observed $\Delta\theta$ in weakly stable conditions but to high values of $\Delta\theta$ in extremely stable conditions. The highest values of the observed $\overline{\theta' w'}$ generally correspond to mid-range values of the observed $\Delta\theta$.

	Model breakdown frequency (% of cases)			
Turbulence scheme	WS	MS	VS	ES
YSU	28	17	15	15
RACMO	29	18	15	15
MYJ	42	38	41	48
QNSE	34	29	28	25
UKMO	28	17	15	15
WUR	29	18	15	15
ECMWF	30	18	15	15
ECAN	35	28	25	23

Table 4.5: Frequency of model breakdown by stability class for the different turbulence schemes. Acronyms correspond to the stability classes in Table 4.4.

van de Wiel et al. (2007) demonstrated that models are generally attracted towards the weakly stable equilibrium and away from the strongly stable equilibrium. Furthermore, if the value of $\overline{\theta' w'}$ exceeds a certain threshold relative to the turbulence, the model breaks down due to runaway surface cooling and the collapse of turbulence (van de Wiel et al., 2007; Van de Wiel et al., 2012a,b). The equilibrium SCM results found in this study are generally consistent with this behaviour. The proportional relationship across all stability classes between $\overline{\theta' w'}$ and the low modelled values of $\Delta\theta$ (Fig. 4.2) implies the model attraction towards the weakly stable solution. Furthermore, the equilibrium SCM frequently broke down (i.e. failed to reach equilibrium), as shown in Table 4.5 by turbulence scheme and stability class.

However, there are other reasons for this breakdown other than collapsed turbulence. First, the equilibrium SCM is sensitive to the height of the upper boundary. If the boundary is too low, the upper boundary values (e.g. zero turbulent flux of TKE) may produce discontinuities in the wind, temperature, and TKE profiles near the upper boundary, causing model breakdown. If the boundary is too high, large altitude ranges aloft can exist where gradients are small and the flux-gradient relationship breaks down (e.g. due to small values of $(\partial U/\partial z)^2$ in the denominator of the gradient Richardson number). Second, an imposed constant value for the 10-m wind speed over 9 h of ABL cooling may in some cases result in large and unrealistic wind shears near 10 m causing discontinuities in the wind and temperature profiles resulting in model breakdown. These two additional factors likely account for a large portion of the breakdown in weakly stable conditions (28-42 % of all cases) where the collapse of turbulence is expected to be infrequent. In extremely stable conditions (breakdown in 15-48 % of all cases), the collapse of turbulence is likely a greater contributing factor. Model breakdown is also more frequent for TKE-based closure schemes, likely attributed to the dependence of the TKE lower boundary value on the wind vector gradients at 10 m (Eq. 4.11), which as discussed above may demonstrate discontinuities due to the constant 10-m wind speed condition. Finally, turbulence schemes that are biased towards low turbulence levels (e.g. MYJ) break down more frequently, which can be attributed either to the collapse of turbulence or to the larger altitude range aloft demonstrating low wind speed gradients.

The mean vertical profiles of modelled and observed wind speed are shown in Fig. 4.3 for the different stability classes. Observed wind speeds tend to decrease with increasing stratification and demonstrate a LLJ below 200 m on average in extremely stable conditions. The different turbulence closure schemes result in a broad range of mean profiles across all stability classes. The modelled profiles all overestimate the wind speed in weakly stable conditions (Fig. 4.3(a)), and are more evenly distributed around the mean observed profile in the other stability classes. By comparing Fig. 4.1 and Fig. 4.3, it is evident that the tendency to underestimate stability (i.e. overestimate mixing) is associated with low wind speed shear below 200 m, as expected. Conversely, models that best represent the stratification demonstrate the highest wind speed shear below 200 m. The two-layer model shows strong agreement with the mean observed profiles for weakly to moderately stable conditions. This result was demonstrated in Chapter 3 and is not surprising given that the model parameters were tuned to the Cabauw data. In very to extremely stable conditions, the two-layer

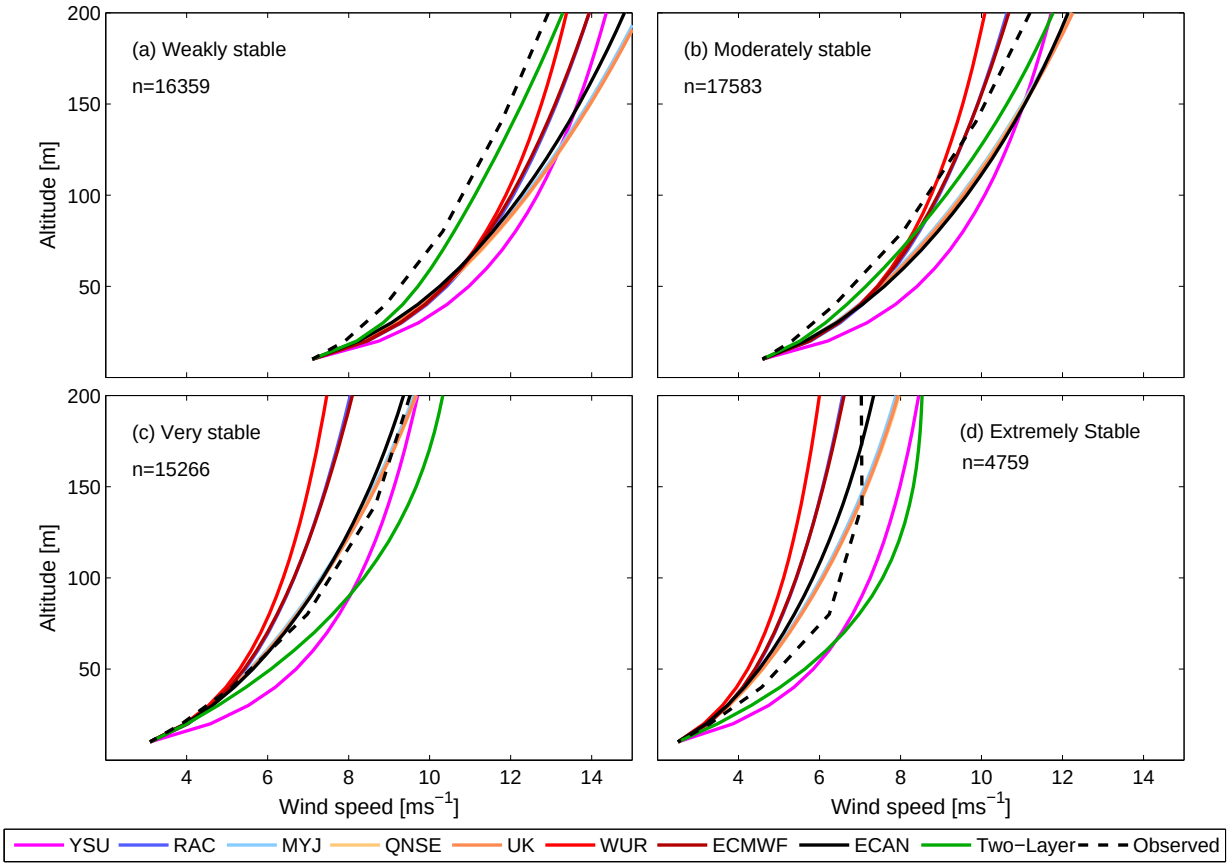

Figure 4.3: Mean vertical profiles of modelled and observed wind speeds for the different stability classes.

model overestimates wind speeds.

It is interesting to note that all modelled profiles in Fig. 4.3 overestimate wind speeds in the lower stability classes despite the tendency to underestimate stratification. We highlight this tendency in Fig. 4.4 where mean modelled and observed wind profiles are shown for weakly to moderately stable conditions but using higher resolution stability classes. We show results only for the UKMO model given that it best represented the stratification in Fig. 4.1. The tendency to overestimate wind speeds is highest at the lowest stratifications. With increasing stratification, the mean modelled profiles show stronger agreement with the observed profiles. The tendency to overestimate wind speeds and wind shear in weakly stable conditions is caused by the local IBL at Cabauw, as demonstrated in Chapter 2. The immediate surroundings at Cabauw (within 200 m) have relatively low roughness, while further from

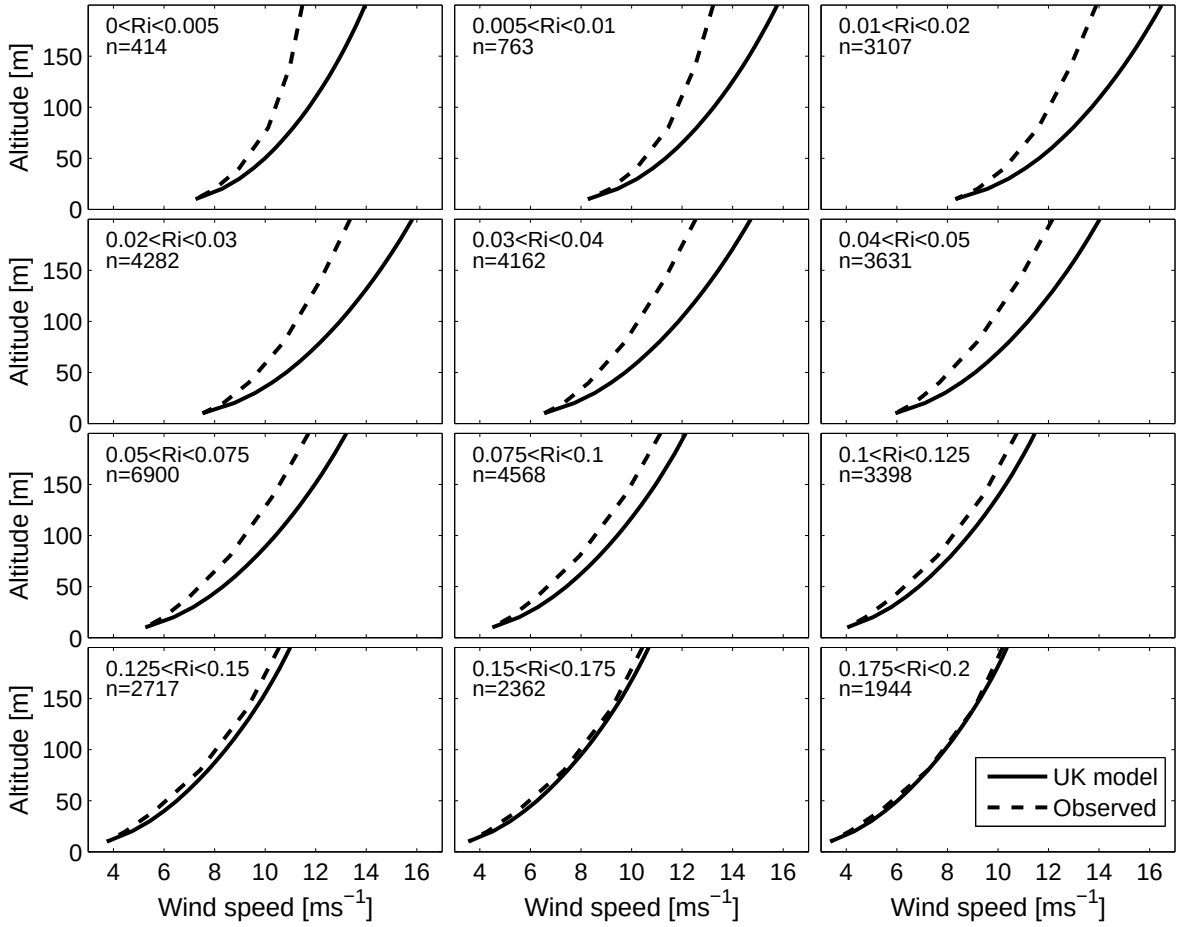

Figure 4.4: Same as Fig. 4.3 but using higher resolution stability classes and only the UKMO turbulence closure scheme.

the tower (within 1-2 km) roughness increases significantly due to the presence of small towns and belts of trees. Turbulence at 10 m (and therefore the wind speeds) in weakly stable conditions are representative of the low local roughness. At higher stratification, the height of the IBL is reduced and the 10-m wind speeds become more representative of regional roughness.

We explore the effect of the IBL on the SCM wind profile in Fig. 4.5 which shows observed and modelled mean momentum flux profiles and mean wind speeds for weakly stable conditions using data between July 1 2007 and June 30 2008 (for which turbulent flux profile observations are available). We use the UKMO turbulence scheme and consider 3 different lower boundary conditions: specified winds at 10m,

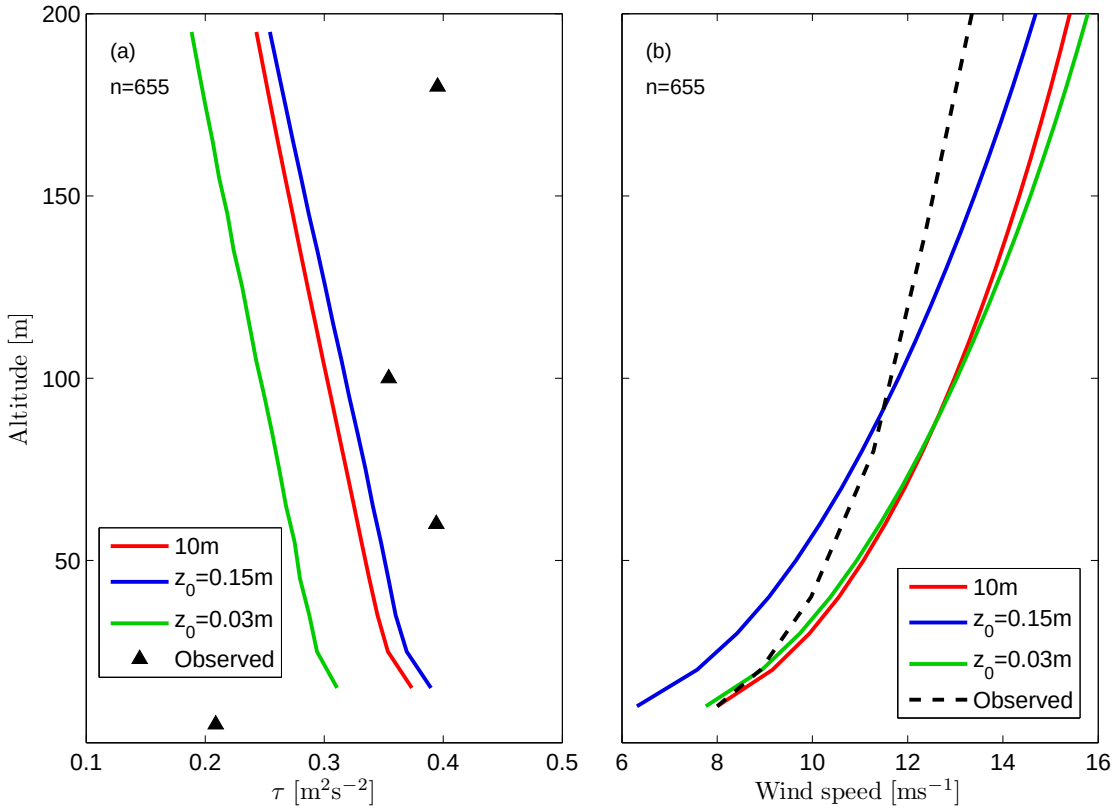

Figure 4.5: Influence of the local IBL at Cabauw for weakly stable conditions and considering different SCM lower boundary heights. We consider results over the period July 1 2007 to June 30 2008. The figure shows mean modelled and observed, (a) momentum flux profiles, and; (b) mean modelled and observed wind speed profiles.

specified surface roughness of $z_0 = 0.15$ m (representative of regional roughness), and $z_0 = 0.03$ m (representative of local roughness). Fig. 4.5(a) clearly demonstrates the IBL in the observed momentum flux profile (i.e. a local maximum at 60 m). Furthermore, the observed fluxes at 180 m are on average higher than those at 100 m, suggesting the existence of a regional high-roughness IBL at Cabauw. In contrast, the modelled profiles (which by construction do not account for IBLs) decrease monotonically with altitude. Different values for the lower boundary shift the modelled profiles (lower fluxes corresponding to lower surface roughness) while the momentum flux gradient is approximately the same between different models. These differences in the modelled and observed momentum flux profiles correspond to differences in the modelled and observed wind speed profiles (Fig. 4.5(b)). The negative modelled

momentum flux gradient (indicating downward transport of momentum) produces relatively high wind speeds above 100 m, while the approximately constant observed momentum flux gradient above 60 m (indicating weak transport of momentum) is associated with comparatively lower observed wind speeds above 100 m. The local IBL at Cabauw (generally above 10 m in weakly stable conditions) results in observed 10 m wind speeds that agree well with those modelled using the low local roughness value (i.e. $z_0 = 0.03$ m). Due to these influences, the use of 10-m wind speeds as a lower boundary results in considerable overestimates of wind shear and wind speeds up to 200 m. Higher values of z_0 result in lower modelled wind speeds on average although the wind speed gradient remains unchanged. Regardless of the lower boundary condition, the SCM (which assumes horizontal homogeneity) is unable to account for a wind profile structure fundamentally associated with horizontal inhomogeneities in the surface roughness.

Box plots of the relative error between modelled and observed winds at different altitudes and stability classes is shown in Fig. 4.6. In general, the spread of the error increases with stratification. Within individual stability classes, there is little variation in spread between the different SCM turbulence closure schemes. Models that use a u_*-scaled λ value (i.e. MYJ, QNSE, UKMO) tend to show slightly less spread than the other models. The two-layer model shows similar spread as the SCMs for weakly to moderately stable conditions, but noticeably higher spread in very to extremely stable conditions.

4.5 Accounting for baroclinicity in the geostrophic wind profile

As demonstrated in the previous section, the effect of the local IBL results in a strong tendency for the SCM (in which horizontal homogeneity was assumed) to overestimate wind speeds in weakly stable conditions. However, the local IBL may not be the only factor producing this bias. It is possible that the vertical structure of the geostrophic wind may be important. We assumed in the previous section that the geostrophic wind vector (calculated from surface pressure measurements) was constant with altitude. In general this is not the case, particularly at near-coastal sites where the land-sea temperature gradient results in baroclinic conditions and a non-zero thermal wind. Given the high sensitivity of the wind speed profile

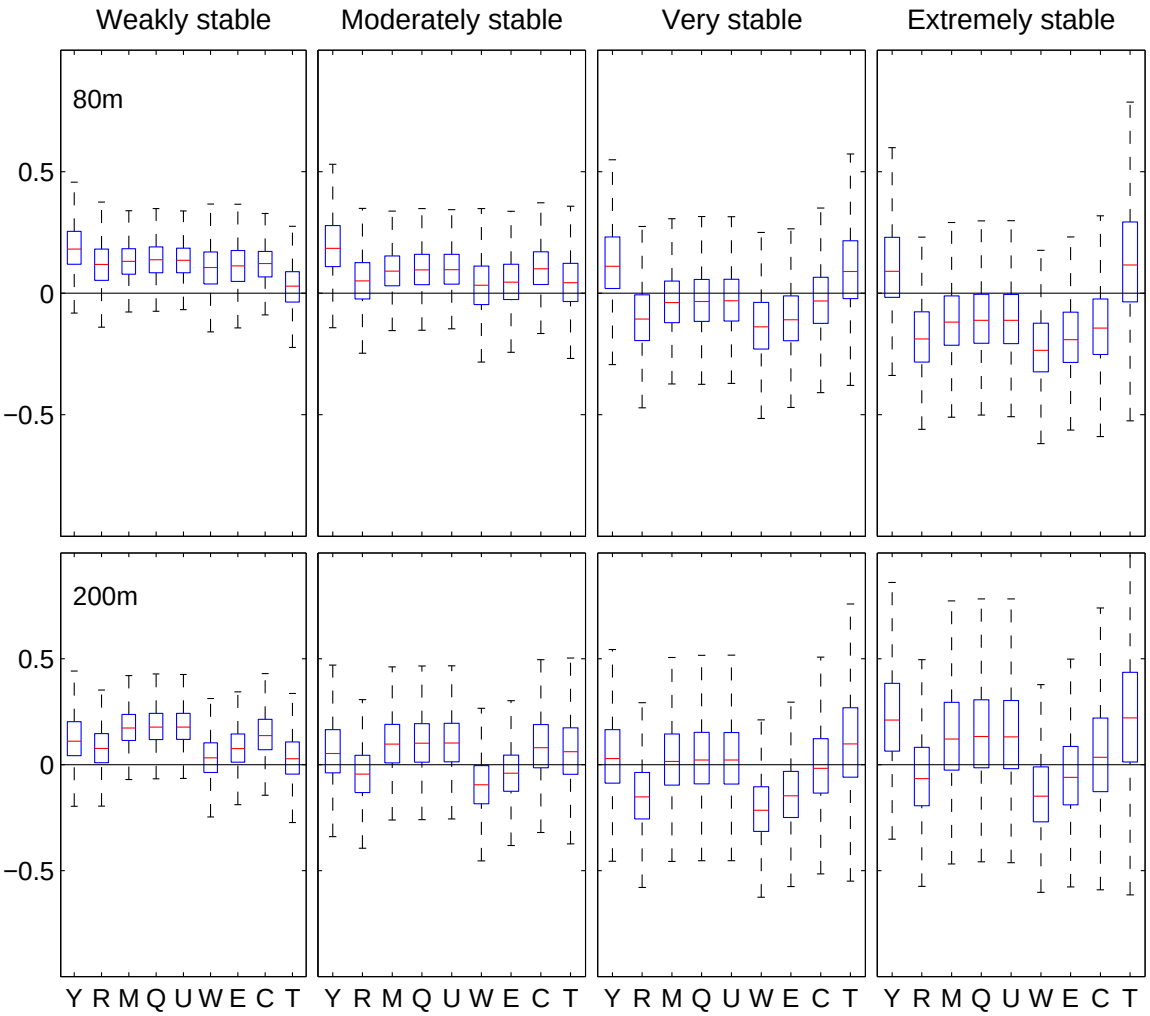

Figure 4.6: Box plots of the relative error between modelled and observed winds (i.e. $(U_{mod} - U_{obs})/U_{obs}$) for different altitudes (rows) and stability classes (columns). The red lines indicate the mean values, blue boxes indicate the interquartile range, and black dotted lines indicate the total range excluding outliers. Acronyms for the different SCM turbulence schemes are listed in Table 4.1 and the acronym T denotes the two-layer model.

throughout the ABL to small changes in the geostrophic wind (Baas et al., 2010; Bosveld et al., 2014a), an accurate representation of the geostrophic wind profile is important. In this section, we explore two different approaches to determining the geostrophic wind profile.

4.5.1 Horizontal temperature gradient approach

Figure 4.7: A map of weather stations operated by KNMI. Cabauw is circled in red, and the remaining weather stations considered in Sect. 4.5.1 are circled in blue. (*Courtesy of KNMI*)

Cabauw is approximately 50 km from the North Sea (Fig. 4.7) and is subject to mesoscale temperature gradients due to the land-sea temperature contrast (Tijm et al., 1999; Bosveld et al., 2014a). We demonstrate this temperature gradient and the resulting thermal wind in Fig. 4.8 for the different stability classes. Distributions of the differences in 2 m temperatures measured at Cabauw and at Hoek van Holland (located about 50 km west of Cabauw and along the coastline) are shown in Fig. 4.8(a). The temperature difference is generally negative due to a relatively warmer sea temperature in stable conditions. Furthermore, the difference is larger for higher stability classes (often more than 6 ^{o}K in extremely stable conditions), attributed to colder land temperatures in higher stability classes.

The mesoscale horizontal temperature gradient can be estimated at Cabauw by

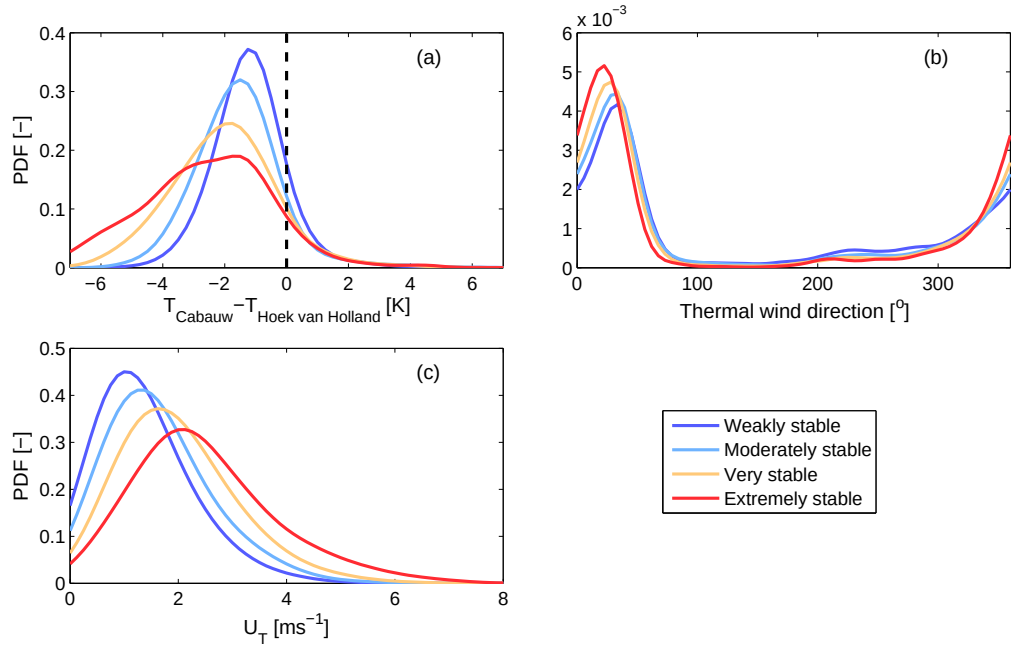

Figure 4.8: Characteristics of the thermal wind between 200 m and the surface by stability class, based on 1.5-m temperature measurements from 11 KNMI weather stations (Fig. 4.7). Shown in the figure are PDFs of: (a) ΔT between Cabauw and Hoek van Holland; (b) the direction of the thermal wind at Cabauw, and; (c) the magnitude of the thermal wind at Cabauw.

using near-surface temperature data from nearby weather stations. For this analysis we select 11 weather stations including Cabauw (Fig. 4.7; Cabauw circled in red, remaining stations circled in blue), selected based on the following criteria: the availability of data from 2001-2010, a distribution of locations covering all directions around Cabauw, a maximum distance of 150 km from Cabauw, and station altitudes below 15 m. Data from each weather station are measured at 1.5 m above the ground and in 1 h intervals. We perform a least-squares planar fit of the data to estimate mesoscale values of $\partial T/\partial x$ and $\partial T/\partial y$. Vertical gradients of the geostrophic wind vector at the surface at Cabauw are then calculated according to the approximate thermal wind balance,

$$\frac{\partial u_G}{\partial z} = -\frac{g}{f\theta_{2m}}\frac{\partial T}{\partial y} \tag{4.13a}$$

$$\frac{\partial v_G}{\partial z} = \frac{g}{f\theta_{2m}}\frac{\partial T}{\partial x} \tag{4.13b}$$

where θ_{2m} is the 2-m potential temperature at Cabauw. The thermal wind components u_T and v_T are calculated according to,

$$u_T = -\frac{R}{f}\frac{\partial T}{\partial y}\ln\left(\frac{p_z}{p_s}\right) \tag{4.14a}$$

$$v_T = \frac{R}{f}\frac{\partial T}{\partial x}\ln\left(\frac{p_z}{p_s}\right) \tag{4.14b}$$

where R is the gas constant, p_z is the pressure at altitude z, and p_s is the surface pressure. The pressure at altitude z is calculated using the vertical temperature gradient at Cabauw, the ideal gas law, and the assumption of hydrostatic equilibrium.

Using Eqn. 4.14, we calculate the thermal wind between the surface and 200 m. Distributions of the thermal wind direction are shown in Fig. 4.8(b) for the different stability classes. The thermal wind is predominately from the NNE for all stability classes, indicative of a temperature gradient towards the WNW and consistent with the expectation that $T_{land} < T_{sea}$. A slightly more northerly component to the thermal wind is observed with increasing stability. Distributions of the magnitude of the thermal wind are shown in Fig. 4.8(c). Magnitudes are higher in extremely stable conditions due to the stronger temperature gradients (Fig. 4.8(a)). The magnitudes in all cases are generally sufficient to have a non-negligible influence on the wind vector profile up to 200 m.

4.5.2 Synoptic interpolation approach

Temperature measurements from nearby weather stations may in general not be available for estimation of the thermal wind. An alternative measure of the thermal wind can be made by comparing the angle between the geostrophic wind vector aloft and that at the surface. For this analysis, we consider the 800 hPa (roughly 2000 m) wind vector from the ERA-interim model as an estimate of the geostrophic wind vector at 2000 m. The thermal wind between the surface and 2000 m is then calculated as the vector difference between the 2000 m and surface geostrophic winds. We consider only cases where both wind vectors have magnitudes greater than 5 ms^{-1} to exclude the high variability in the thermal wind direction during low wind speed events. Distributions of the resulting thermal wind direction are shown in Fig. 4.9(a) for the different stability classes. Compared to the surface-200 m thermal wind direction PDFs estimated in the previous section, the distributions in Fig. 4.9(a) demonstrate

a broader a range of values and in particular a larger representation of westerly thermal winds. This broader range is expected given that that the temperature gradient is not generally uniform with altitude between the surface and 2000 m. The westerly thermal winds may be attributed to the planetary scale north-south temperature gradient, expected to have some influence well above the surface. Distributions of the magnitude of the thermal wind are shown in Fig. 4.9(b). Differences in the magnitudes for different stability classes are much smaller than found for the surface-200 m estimates. Furthermore, the magnitudes are considerably higher than those found for the surface-200 m estimates, which is expected given the larger (by a factor of 10) altitude range.

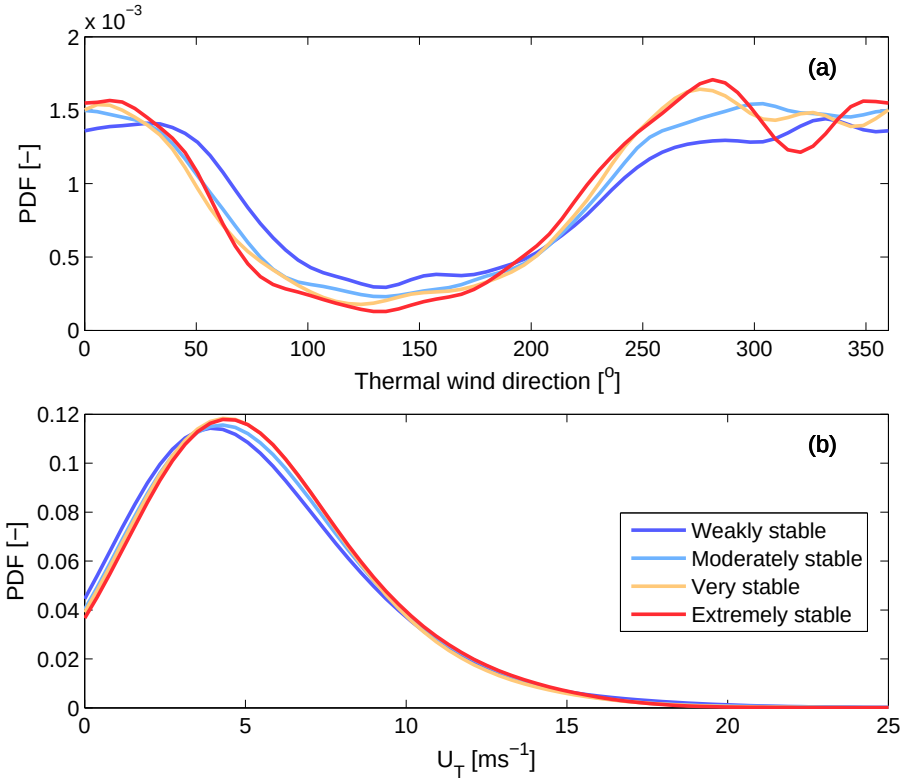

Figure 4.9: Characteristics of the thermal wind by stability class, calculated as the vector difference between the 800 hPa wind vector and the surface geostrophic wind vector. The summer case is shown in red, the winter case in blue. Shown in the figure are PDFs of: (a) the direction of the thermal wind; and (b) the magnitude of the thermal wind.

4.5.3 Applying the baroclinic correction to the wind speed profiles

Having demonstrated two reasonable and broadly consistent approximations of the thermal wind, we now examine the influence of the thermal wind on the wind speed profile up to 200 m at Cabauw.

We focus on the $0.075 < Ri_B < 0.15$ stability range in which the effect of the local IBL is reduced (Fig. 4.4) and the equilibrium approach remains a reasonable approximation. We consider all seasons and use only the UKMO turbulence closure scheme, which most accurately represented the stratification as well as the wind profile up to 200 m in the specified stability range. We conduct a sensitivity analysis on the wind speed profile below 200 m by considering a range of representations of the geostrophic wind vector profile. For the 'mesoscale temperature gradient' approach (G 500 and G 1000 in Table 4.6), an altitude limit must be specified under which the surface-derived $\partial u_G/\partial z$ and $\partial v_G/\partial z$ values (Eq. 4.13) at Cabauw should apply. Using a mesoscale model, Bosveld et al. (2014a) demonstrated considerable geostrophic wind shear at night up to 1000 m that was strongest at the surface. Based on their result, we consider two altitude limits in this analysis, 500 m and 1000 m, below which $\partial u_G/\partial z$ and $\partial v_G/\partial z$ are kept constant and above which these values are set to zero. For the 'synoptic interpolation approach' (Syn linear and Syn log in Table 4.6), we interpolate the surface geostrophic wind vector components to the 800 hPa wind vector components at 2000 m. Above 2000 m (where applicable), the geostrophic wind vector is kept constant at the 800 hPa values. We consider both linear and logarithmic interpolation, acknowledging that the thermal wind (and therefore the geostrophic wind shear) will be strongest closest to the surface.

Mean modelled and observed wind profiles are shown in Fig. 4.10 for different wind direction sectors (based on the observed 200 m wind direction). The influence of the thermal wind on the modelled wind profile is strongly dependent on wind direction. For the 'mesoscale temperature gradient' approach, the influence is largest in the SW sector and smallest in the NE sector. These results indicate a surface-200 m thermal wind from the NE on average and are consistent with results found in Fig. 4.8 for moderately stable conditions. For the 'synoptic interpolation approach', the influence is largest in the NE and SE sectors and negligible in the NW and SW sectors. These results indicate a surface-2000 m thermal wind from the west on average, broadly consistent with the results found in Fig. 4.9(a). We note that the 'Syn log' approach

Name	Abbreviation	Description
Const	C	Surface geostrophic wind vector is assumed constant with altitude (as in Sect. 4.4)
G 500	G1	$\partial u_G/\partial z$ and $\partial u_G/\partial z$ at the surface (based on temperature measurements from nearby weather stations) are assumed constant up to 500 m, and zero above.
G 1000	G2	Same as above, but up to 1000 m
Syn linear	S1	Surface geostrophic wind vectors at 10 m are linearly interpolated to the 800 hPa wind vectors at 2000 m
Syn log	S2	Same as above, but using logarithmic interpolation

Table 4.6: Different representations of the geostrophic wind vector profile considered in this analysis.

produces much larger (and generally unrealistic) corrections to the wind profile for the NE and SE directions compared to the other approaches.

Box plots of the relative error between modelled and observed winds at different altitudes and stability classes are shown in Fig. 4.11. In general, there is little variation in the spread between different models apart from the 'Syn log' model which shows substantial spread in the NE and SE sectors. The 'Syn linear' approach tends to show slightly less spread than the other models, while the 'G 1000' approach tends to show slightly more spread.

4.6 Discussion

To our knowledge, this is the first study to carry out an observationally-based assessment of SCM wind and temperature profiles using an equilibrium approach. In previous studies, equilibrium approaches have been employed for inter-model comparisons (Weng and Taylor, 2003; Cuxart et al., 2006) or for exploring general characteristics of the ABL (Weng and Taylor, 2006; Sorbjan, 2014) without comparison to atmospheric observations. Furthermore, to our knowledge this is the first SCM study to use an observational dataset sufficiently large (10 years) to obtain a comprehensive sampling of atmospheric conditions. Previous observation-based SCM studies have focused only on one or several case studies (Baas et al., 2010; Bosveld et al., 2014b).

Results from this study clearly demonstrate the limitations of an equilibrium-

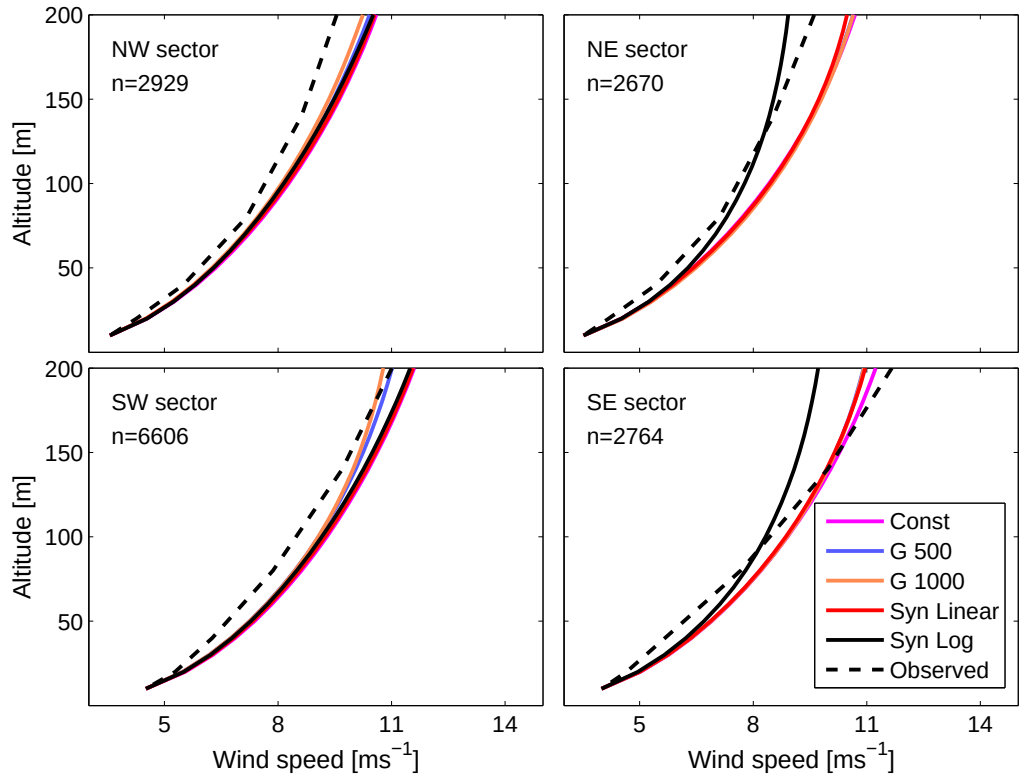

Figure 4.10: Mean modelled and observed wind speed profiles for different wind direction sectors. Different models account for different representations of the geostrophic wind profile (Table 4.6). The UKMO turbulence scheme is used and the $0.075 < Ri_B < 0.15$ stability range is considered.

based SCM in modelling the SBL under stable stratification. Specifically, the use of near-surface $\overline{\theta' w'}$ values as a lower boundary condition was found to be a crucial limitation. Two physically meaningful equilibrium values have been found to exist for a given $\overline{\theta' w'}$ value in stably stratified conditions (van de Wiel et al., 2007) - a relatively weak stratification solution and a relatively strong stratification solution. Both of these equilibriums were found to exist at Cabauw. However, as demonstrated in van de Wiel et al. (2007), a model generally either tends towards the weak stratification solution or breaks down due to the collapse of turbulence. This mechanism was clearly evident for the equilibrium SCM considered in this study. In addition, the equilibrium approach was limited in its ability to account for time-evolving phenomena such as the IO and LLJ in very to extremely stable conditions. Fundamentally, turbulent timescales are considerably higher in the SBL (minutes to hours) compared to the neutral or unstable ABLs (seconds to minutes). Therefore, the state of the

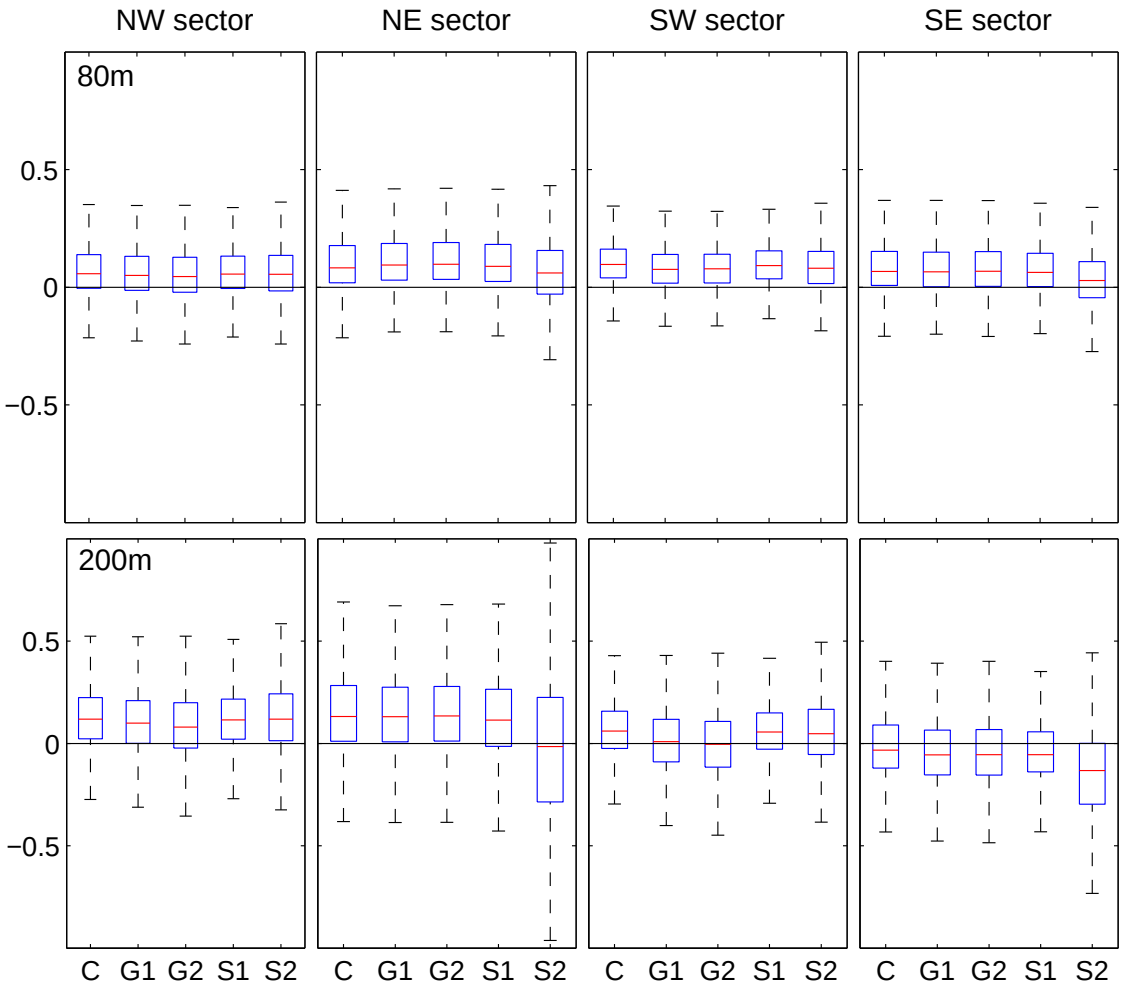

Figure 4.11: Box plots of the relative error between modelled and observed winds (i.e. $(U_{mod} - U_{obs})/U_{obs}$) for different altitudes (rows) and wind direction sectors (columns). Different models account for different representations of the geostrophic wind profile (Table 4.6). The UKMO turbulence scheme is used and the $0.075 < Ri_B < 0.15$ stability range is considered.

SBL (and particularly the extremely stable SBL) at a given point in time depends on the state of the SBL minutes to many hours previous. Though useful for exploring SBL properties and for intermodel comparisons within an idealized framework, the equilibrium approach is generally not able to provide an accurate simulation of the observed SBL.

The assumption of horizontal homogeneity also contributed to the bias between SCM results and observations. In particular, the local IBL at Cabauw resulted in a

strong tendency for the SCMs to overestimate wind speeds in weakly stable conditions. In contrast, the two-layer model was accurate in this stability class. This result can be attributed to the degree to which the two-layer model was tuned to the Cabauw data. As described in Chapter 3, the two-layer model uses a MOST-based stability function within the surface layer that was derived based on Cabauw data (Beljaars and Holtslag, 1991). Furthermore, in cases where the diagnosed surface layer height was less than 10 m (i.e. very to extremely stable conditions), the model reduced to an Ekman model and a parameterization of the diffusivity coefficient was selected that best matched the mean wind profile at Cabauw. Finally, surface stability was determined from the Richardson number calculated between 10 m and the surface, based on the assumption that 2-m temperatures were representative of surface values. This assumption tended to underestimate near-surface stability and often modelled neutral stratification in weakly to moderately stable conditions. This unintentional bias towards neutral conditions resulted in a wind profile that matched the observed IBL-influenced wind profile at Cabauw. In very to extremely stable conditions, the breakdown of the two-layer model was evident and the equilibrium SCM was more accurate.

As demonstrated in this and in previous studies, the modelled wind profiles are highly sensitive to the choice of turbulence closure scheme. Schemes with constant or no asymptotic mixing length limits resulted in the largest underestimates of stratification, while those schemes with asymptotic mixing length limits that scaled with the boundary layer height (i.e. $\lambda = au_*/f$) resulted in the most accurate representations of stratification. These latter schemes (i.e. MYJ, QNSE, UKMO) performed nearly identically in the modelling of wind profiles, despite using different levels of turbulence closure (order 2, 1.5, and first-order, respectively). The RACMO (order 1.5) and ECMWF (first-order) schemes also performed similarly though were less accurate than the MYJ, QNSE, and UKMO models. The accuracy of a given turbulence closure scheme depends fundamentally on an accurate representation of the diffusivity coefficients, as calculated using appropriate mixing length and stability function formulations. The results of this study suggest that higher-order (and more computationally expensive) turbulence schemes offers no more increased accuracy than computationally simpler first-order schemes for SCM modelling of winds and temperature below 200 m.

This analysis also demonstrated the influence of baroclinicity on the wind profile at a near-coastal site. Although the effects of baroclinicity at Cabauw during a

summer day have been well demonstrated (Tijm et al., 1999; Bosveld et al., 2014a), the effects in stable stratification have to our knowledge not been explored. We demonstrated that the land-sea temperature difference in stable stratification is often large and considered several representations of the geostrophic wind profile. Contrary to unstable conditions - where accounting for the thermal wind has been shown to have substantial influence on the wind profile below 200 m (Bosveld et al., 2014a) - the influence in stable stratification was shown here to be modest.

In general, an equilibrium-based SCM approach for modelling the wind profile is fundamentally limited. A natural question is whether an SCM that makes use of time-evolving observations will result in more accuracy across all stability classes. Such an approach has the added benefit of less computational cost compared to the equilibrium approach (which evolved for 9 h for each fixed point in time) and less likelihood of model breakdown since an equilibrium state is not required. Furthermore, such an approach would allow for a distinction between errors arising from the equilibrium assumption and that of horizontal homogeneity. By considering the time-evolving problem we can determine the overall utility of the single-column approach.

4.7 Conclusions

In this study, we used an idealized equilibrium SCM to extrapolate 10-m winds within the altitude range most relevant to wind energy. We explored the sensitivity of the wind profile to different turbulence closure schemes and to different estimates of the geostrophic wind vector profile accounting for baroclinic conditions. We compared model results to 10 years of 10-min averaged observations at the 213 m Cabauw tower in the Netherlands. Results from this study demonstrated several limitations to the equilibrium approach. First, the existence of two physically meaningful equilibrium solutions for a given value of the surface turbulent temperature flux (used as a lower boundary in the SCM) generally resulted in either a tendency to underestimate stratification or the breakdown of the model due to runaway cooling and collapsed turbulence. Second, the equilibrium approach was by design unable to accurately account for time-evolving phenomena such as the inertial oscillation and low-level jet. We further demonstrated in this study no clear association between the accuracy of the wind profile and the order of turbulence closure. Rather, the accuracy of the diffusivity coefficient (calculated using appropriate mixing length and stability function formulations) varied across all orders of turbulence closure and had predom-

inant influence on wind profile accuracy. Baroclinic influences due to the land-sea temperature gradient were shown to have only modest influence on the wind speed profile below 200 m for moderately stable conditions. The IBL at Cabauw resulted in a strong tendency for the SCM to overestimate wind speeds in weakly to moderately stable conditions. In very stable conditions (where the IBL influence was low), SCM accuracy was improved. Despite these limitations, the equilibrium SCM was found to outperform a highly-tuned two-layer logarithmic-Ekman model. Results from this study indicate the need to assess the role of time dependence relative to the other limitations of the equilibrium SCM approach.

Chapter 5

A comparison of equilibrium and time-evolving approaches to modelling the wind profile up to hub-height under stable stratification

The contents of this chapter are based on the following paper:

Optis, M., A. Monahan (2015). 'A comparison of equilibrium and time-evolving approaches to modelling the wind profile up to hub-height under stable stratification'. *Journal of Applied Meteorology and Climatology*, To be submitted.

5.1 Introduction

The modelling of the stable boundary layer (SBL) continues to be a challenge (Mahrt, 2014)) due to the presence of weak or almost collapsed turbulence and, consequently, the influence of a range of other processes (e.g. intermittent turbulence (Poulos et al., 2002), gravity waves (Mahrt, 1998), baroclinicity (Mahrt, 1998), surface heterogeneity (Verkaik and Holtslag, 2007), thin and 'upside-down' boundary layers (Mahrt and Vickers, 2002), inertial oscillations (IOs) (Baas et al., 2012), and low-level jets (LLJs) (Van de Wiel et al., 2010)). Research on the SBL has focused mainly on

the representation of turbulence given the high sensitivity of atmospheric models to different parameterization schemes (ECMWF, 2006; Beljaars and Viterbo, 1999). Single-column models (SCMs) are a tool often used to formulate or evaluate turbulence parameterization schemes within the atmospheric boundary layer (ABL). These models are advantageous due to their low computational requirements, flexibility in determining which processes and parameterizations are included (e.g. turbulence, radiation, entrainment, land surface characteristics, etc.), and the ability to specify a lower boundary above the surface (Chapter 4). The complexity of an SCM can vary from models that incorporate the complete physics of a 3D model to highly idealized representations that consider only the momentum and temperature budgets.

SCMs are often used within an equilibrium framework to study SBL characteristics up to moderately stable conditions. Specifically, the SCM is initialized from neutral stratification and then evolves over a 9-12 h period with imposed external forcings (e.g. geostrophic wind speed, surface cooling rate). The intent of this approach is for the SBL to reach a 'quasi-equilibrium' state in which the wind profile and potential temperature gradient become constant in time (although the potential temperature itself decreases due to continued surface cooling). The structure of the SBL (e.g. boundary layer height, vertical profiles, surface turbulence, etc.) and relationships between parameters (e.g. flux-gradient relationships) can then be evaluated from the quasi-equilibrium state. This approach has been used in a number of studies to explore SBL characteristics (e.g. Weng and Taylor 2006; Sterk et al. 2013; Sorbjan 2012, 2014) and to compare different turbulence parameterizations (e.g. Weng and Taylor 2003; Cuxart et al. 2006; Edwards et al. 2006). In Chapter 4, we identified several limitations of the equilibrium approach. First, the only suitable observed parameter available within an equilibrium framework to account for surface cooling was the turbulent temperature flux. It has been shown that two physically meaningful solutions exist for a given value of the temperature flux - a relatively weak stratification solution and a relatively strong stratification solution (van de Wiel et al., 2007; Gibbs et al., 2015). It was demonstrated in Chapter 4 that the equilibrium SCM either is attracted towards the weak stratification solution (thereby frequently underestimating stratification) or broke down due to runaway surface cooling and the collapse of turbulence as well as other factors. Second, the equilibrium approach did not accurately account for the observed IO and the LLJ evolution, since these processes depended on the time-evolving state of the SBL and in particular the degree of departure of the wind profile at the time of sunset to its equilibrium profile

during the night (Van de Wiel et al., 2010). Focusing on the time evolution of the SCM overcomes the limitations of the equilibrium approach. Time-evolving temperature measurements (readily available at multiple altitudes) can be used to account for stability (thereby avoiding the two solution ambiguity problem), while IOs and LLJs are more robustly modelled within a time-evolving framework. Time-evolving SCMs have been used recently to model the evolution of the LLJ and to assess SCM sensitivity to variations in model parameterizations (e.g. Baas et al. 2010; Bosveld et al. 2014b). Baas et al. (2010) in particular explored the sensitivity of an SCM to changes in the geostrophic forcing, turbulence schemes, baroclinicity, and advective tendencies.

Accurate SCM simulations of the observed SBL are challenging due to the influence of 3D processes (e.g. momentum and temperature advection, baroclinic effects, internal boundary layers (IBLs)). Horizontal homogeneity is generally assumed in the construction of a SCM although 3D processes can be parameterized. For example, (Bosveld et al., 2014a) used piecewise constant functions to model momentum, temperature, and moisture advection and specified a geostrophic wind profile to account for baroclinicity. The influence of advective tendencies can be mitigated by compositing SCM results from a larger data set, provided these tendencies are sufficiently variable to cancel out on average. Baas et al. (2010) demonstrated that compositing SCM results over 8 LLJ events with comparable external forcings averaged out the effects of advective tendencies, facilitating comparison with similarly composited observations.

The existence of IBLs also limits the accuracy of a 1D model. For example, low local roughness within 200 m of the Cabauw meteorological tower in the Netherlands combined with higher regional roughness results in a local IBL extending up to about 20 m in near-neutral conditions (Holtslag, 1982; Verkaik and Holtslag, 2007). The extrapolation of 10 m wind speeds (within the IBL) aloft implicitly assumes horizontally homogeneous low roughness conditions, resulting in a strong tendency to overestimate wind speeds (demonstrated in Chapters 2-4). The influence of IBLs can be mitigated by using a lower boundary above the IBL or by using a surface-based lower boundary and specifying a roughness length (z_0) that more closely represents the surface roughness of the upstream region of interest (e.g. the use of mesoscale roughness values for studying the wind profile up to heights of 500 m, as in Baas et al. (2010) and Bosveld et al. (2014a)). However, the specification of z_0 is not straightforward as it is a poorly constrained parameter to which the wind profile is generally

highly sensitive (Chapter 2).

The influence of 3D processes can be accounted for by using a 3D atmospheric model. Mesoscale models generally have horizontal resolutions around 1-2 km and can in principle account for 3D processes on these and larger length scales. Processes on smaller length scales (e.g. IBL development at Cabauw) are not expected to be accurately resolved by a mesoscale model with such resolution. Higher resolutions in 3D models are possible (e.g. microscale models) but require even greater computational cost and detailed surface roughness characteristics to account for microscale features such as the IBL at Cabauw.

Given its low computational requirements and its ability to make use of local observations, the SCM is an appealing alternative to a 3D model. The appeal is particularly strong in the context of wind energy meteorology, where accurate modelling of the wind speed profile up to about 200 m is important for wind resource assessment and forecasting. Used for such purposes, the SCM provides a middle ground between the use of conventional and highly simplified wind speed extrapolation equations and the use of computationally costly but more physically robust 3D atmospheric models. Extrapolation equations range from those that take no account of atmospheric physics (e.g. power law profile), through those that provide a limited account of atmospheric turbulence (e.g. logarithmic wind speed profile), to those that account for more detailed forcings including the pressure-gradient force and the Coriolis force (e.g two-layer logarithmic-Ekman model in Chapter 3). We have demonstrated the breakdown of the logarithmic wind speed profile beyond weakly stable conditions (Chapter 2) and have demonstrated considerable improvements in mean wind profile accuracy for all stratifications by using a two-layer logarithmic-Ekman model (Chapter 3). Although accurate on average, the two-layer model demonstrated large spread in the wind speed error in very to extremely stable conditions, attributed in part to the inability to account for time-evolving processes such as the IO and LLJ. The use of 3D mesoscale models such as the Weather and Research Forecasting (WRF) model (which account for time-evolving processes) is becoming increasingly common for purposes ranging from wind resource assessments, wind farm siting, and predicting ramp events (e.g. Storm et al. 2009, 2010; Floors et al. 2013; Zhang et al. 2013; Nunalee and Basu 2014; Yang et al. 2014). To our knowledge, a detailed comparison of equilibrium and time-evolving approaches to wind profile modelling over a large composite dataset has not been investigated, nor has a comparison of 1D and 3D models been carried out.

5.1.1 Intent of study

The intent of this study is to compare the relative performances of an equilibrium SCM, a time-evolving SCM, and a time-evolving WRF model in the representation of the wind profile under stable stratification. Data obtained from the Cabauw meteorological tower in the Netherlands over a 10-year period are used to drive the models and to assess the accuracy of model performance. In Sect. 5.2 we describe the data sources. The SCM set-up including the different turbulence schemes considered is provided in Sect. 5.3 along with a description of the WRF model set-up. In Sect. 5.4 we compare SCM and WRF model performance for the LLJ case studies, considering a range of turbulence parameterization schemes for the SCM. We then assess the time-evolving SCM performance using different heights above the surface as the lower boundary and compare results to the LLJ case studies. In Sect. 5.5, we compare model performance using composite results obtained over the 10-year period and for different stability classes. A discussion is provided in Sect. 5.6 and conclusions in Sect. 5.7.

5.2 Data sources

Most observational data used in this study are obtained from the Cabauw meteorological tower in the Netherlands, operated by the Royal Netherlands Meteorological Institute (KNMI). Measurements of meteorological variables at 10-min resolution were obtained from January 1 2001 to December 31 2010 (these data are available at http://www.cesar-database.nl). Wind speed and direction measurements are made at 10 m, 20 m, 40 m, 80 m, 140 m, and 200 m, and temperature measurements are made at these altitudes as well as 2 m. Surface pressure measurements at 10-min resolution are also provided, which are used to calculate the potential temperature at different heights. Turbulent momentum flux data at 10-min resolution are provided by KNMI for the period July 2007 - June 2008 at altitudes of 5 m, 60 m, 100 m, and 180 m. Surface geostrophic wind data also provided by KNMI are derived from 1 h surface pressure measurements from weather stations near Cabauw using a second-order polynomial fit. We use 6-h averaged wind vector data at 800 hPa taken from the European Centre for Medium-Range Weather Forecasts (ECMWF) ERA-interim global atmospheric reanalysis as an estimate for the geostrophic wind aloft (available at http://apps.ecmwf.int/datasets). These data are linearly interpolated horizontally

to the Cabauw coordinates. Data sources for the WRF model are described in Sect. 5.3. All data used in this analysis are interpolated to 10-min resolution.

5.3 Model setup

5.3.1 SCM governing equations and turbulence schemes

We consider an idealized, horizontally homogeneous atmospheric boundary layer (ABL) with no radiative or moist processes, resulting in the following eddy-averaged equations,

$$\frac{\partial u}{\partial t} = f(v - v_G) - \frac{\partial(\overline{u'w'})}{\partial z} \tag{5.1a}$$

$$\frac{\partial v}{\partial t} = -f(u - u_G) - \frac{\partial(\overline{v'w'})}{\partial z} \tag{5.1b}$$

$$\frac{\partial \theta}{\partial t} = -\frac{\partial(\overline{\theta'w'})}{\partial z} - S_c \tag{5.1c}$$

where u and v are the horizontal components of the wind vector, θ is the potential temperature, t is time, f is the Coriolis parameter, $\overline{u'w'}$ and $\overline{v'w'}$ are the horizontal components of the vertical turbulent momentum flux per unit mass, $\overline{\theta'w'}$ is the vertical turbulent temperature flux, and z is the height above the surface. For simplicity, the air density is assumed to be constant. The components of the geostrophic wind (u_G and v_G) at an altitude z are determined from a linear interpolation of the surface-pressure derived values at the surface to the 800 hPa ERA-interim wind vector at the top of the domain (2000 m). The term S_c is a specified constant cooling rate decreasing linearly from 0.1 Kh^{-1} at the top of the domain to zero at the surface:

$$S_c = C\frac{z}{z_{max}} \tag{5.2}$$

with $C = 2.77 \times 10^{-5}$ Ks^{-1} and z_{max} the top of the domain. Using this formulation, the lower ABL temperature is controlled predominately by the observed lower boundary temperature values while the upper ABL (which under stable stratification is decoupled from the lower ABL) cools at a rate consistent with upper-ABL observations (Stull, 1988).

The turbulent fluxes in Eq. 5.1 are parameterized as diffusion processes,

$$\overline{u'w'} = -K_m \frac{\partial u}{\partial z} \tag{5.3a}$$

$$\overline{v'w'} = -K_m \frac{\partial v}{\partial z} \tag{5.3b}$$

$$\overline{\theta'w'} = -K_h \frac{\partial \theta}{\partial z} \tag{5.3c}$$

where K_m and K_h are the eddy diffusivities of momentum and temperature, respectively, which can be specified through a range of turbulence closure schemes (Stull, 1988; Cuxart et al., 2006). For first-order closure, the diffusivities are expressed as,

$$K_m = l_m^2 \frac{\partial U}{\partial z} f_m \tag{5.4a}$$

$$K_h = l_m l_h \frac{\partial U}{\partial z} f_h \tag{5.4b}$$

where l_m and l_h are the mixing lengths for momentum and heat, respectively, and $\partial U/\partial z = \sqrt{(\partial u/\partial z)^2 + (\partial v/\partial z)^2}$ is the magnitude of the wind shear. The stability functions f_m and f_h are usually expressed in terms of the local Richardson number but are sometimes expressed using the non-dimensional Monin-Obukhov similarity theory (MOST) functions for momentum and temperature (i.e. $f_m(Ri) = \phi_m^{-2}(z/L)$ and $f_h(Ri) = \phi_h^{-2}(z/L)$).

One commonly used first-order parameterization that makes use of MOST-based stability functions is derived beginning with the key equations of MOST and the Panofsky (1973) altitude-dependent form of $\tau/\rho = \sqrt{(\overline{u'w'})^2 + (\overline{v'w'})^2}$,

$$l_m = \kappa z \tag{5.5a}$$

$$\frac{\partial U}{\partial z} = \frac{u_*}{l_m} \phi_m \tag{5.5b}$$

$$\sqrt{\frac{\tau(z)}{\rho}} = u_* \left(1 - \frac{z}{h_{ABL}}\right)^{\alpha} \tag{5.5c}$$

with κ the von Karman constant, u_* the surface friction velocity, h_{ABL} the ABL height, and α a tunable constant. Combining Eqs. 5.5(a)-(c) with Eqs. 5.4(a)-(b)

results in the following expressions for the diffusivities:

$$K_m = \frac{\kappa z u_*}{\phi_m}(1 - \frac{z}{h})^{2\alpha} \tag{5.6a}$$

$$K_h = \frac{\kappa z u_*}{\phi_h}(1 - \frac{z}{h})^{2\alpha} \tag{5.6b}$$

In 1.5 order closure, the diffusivities are expressed in terms of the turbulent kinetic energy (TKE),

$$K_m = c_m l_m f_m \sqrt{E} \tag{5.7a}$$

$$K_h = c_h l_h f_h \sqrt{E} \tag{5.7b}$$

where c_m and c_h are constants, and E is the TKE determined through its prognostic budget (where we neglect TKE transport from pressure perturbations),

$$\frac{\partial E}{\partial t} = -\overline{u'w'}\frac{\partial u}{\partial z} - \overline{v'w'}\frac{\partial v}{\partial z} + \frac{g}{\theta}\overline{\theta'w'} - \frac{\partial}{\partial z}\left(\overline{E'w'}\right) - \epsilon \tag{5.8}$$

where $\overline{E'w'}$ is the vertical turbulent flux of TKE, generally expressed as a diffusion process,

$$\overline{E'w'} = -K_e \frac{\partial E}{\partial z} \tag{5.9}$$

with K_e the TKE diffusivity. The term ϵ in Eq. 5.8 is the dissipation rate, which in 1.5 TKE closure is parameterized according to,

$$\epsilon = \frac{c_d E^{3/2}}{l_d} \tag{5.10}$$

where c_d is a constant and l_d is the dissipation length scale. Higher-order closure schemes make use of one or more additional prognostic equations for variables such as ϵ, the mixing lengths, and the vertical turbulent fluxes. The Mellor and Yamada (1982) formulation is one such scheme in which prognostic equations for the turbulent fluxes are related algebraically resulting in simplified expressions (see Table 5.2).

The broad range of turbulence closure schemes that exist in the literature differ in how the diffusivity coefficients K_m and K_h and related variables (e.g. f_m, l_m, ϵ) are parameterized. We consider a range of turbulence closure schemes investigated in

Bosveld et al. (2014b) and Kleczek et al. (2014). Limiting the complexity of schemes to no higher than level 1.5 TKE closure (but including Mellor-Yamada), we identify a total of 8 different turbulence closure schemes considered between these two studies. In Chapter 4, we identified several of these schemes that did not perform well in stable stratification: the Yonsei University (YSU) and Wageningen University schemes both considerably underestimated stratification while the Environment Canada scheme showed large spread in model results. These schemes are excluded from the present analysis. The remaining schemes are considered in this analysis for the time-evolving SCM, and are listed in Table 5.1 with complete parameterizations provided in Table 5.2. In Chapter 4, we found the UKMO turbulence scheme to be the most accurate relative to the other turbulence schemes for use in an equilibrium SCM. We therefore only consider the UKMO scheme for use in the equilibrium SCM in this study. Note that we include the YSU scheme in Table 5.2 as it is used in the WRF simulations in this study.

To facilitate calculations for the MYJ scheme, we replace the usual form of the mixing length limit,

$$\lambda = \beta \frac{\int_0^{h_{ABL}} |z| q da}{\int_0^{h_{ABL}} q dz} \tag{5.11}$$

where $q = \sqrt{2E}$ and β is a constant, with the form $\lambda = a u_*/f$. Both representations of λ scale with h_{ABL}, so the substitution is not expected to result in significant changes to model results. For the UKMO scheme, Smith (1990) uses a value of λ that scales with h_{ABL}, but no equation is provided. We therefore assume the form $\lambda = a u_*/f$.

5.3.2 Time-evolving SCM numerical scheme and boundary conditions

For the LLJ case studies, the time-evolving SCM is initialized from a neutral profile beginning at 1200 UTC (as in Baas et al. (2010) and Bosveld et al. (2014a)) to allow sufficient time for model spin-up. The neutral profile is determined by assuming equilibrium (i.e. $\partial u/\partial t = \partial v/\partial t = 0$) in Eqs. 5.1(a)-(b) and then solving the resulting set of ordinary differential equations using a boundary-value problem (BVP) solver in the MATLAB software package ('bvp4c', described at http://www.mathworks.com/help/matlab/ref/bvp4c.html). For this calculation, we specify a first-order closure scheme with a mixing length of the form $l_m^{-1} = (\kappa z)^{-1} + \lambda^{-1}$, with $\lambda = 70$ m. We specify an initial logarithmically-scaled vertical grid with 200 vertical levels to provide high

Name/Organization	Abbreviation	Order	Reference
Royal Netherlands Meteorological Institute	RACMO	1.5	Unden (2002)
Mellor-Yamada-Janjic	MYJ	2	Galperin et al. (1988); Janjic (2002)
Quasi-Normal Scale Elimination	QNSE	1.5	Sukoriansky (2008)
UK Met Office	UKMO	1	Smith (1990)
European Centre for Medium-Range Weather Forecasts	ECMWF	1	ECMWF (2006)
Yonsei University	YSU	1	Hong and Pan (1996)

Table 5.1: Turbulence closure schemes considered in this study.

Scheme	Diffusivity	Mixing length	Constants and stability functions
YSU	$K_m = l_m u_* \phi_m^{-1}(1 - z/h_{ABL})^2$ $K_h = Pr^{-1} K_m$	$l_m = \kappa z$	$Pr = \phi_h \phi_m^{-1} + 0.78\kappa$; $\zeta = z/L$ $\phi_m = \phi_h = 1 + 5\zeta$
RACMO	$K_{m,h} = l_{m,h}\sqrt{E}$; $K_e = 2K_m$	$l_{m,h}^{-1} = (c_n \kappa z)^{-1} + \lambda^{-1} + s_{m,h}^{-1}$ $s_{m,h} = c_{m,h}\sqrt{E} N^{-1}$ $l_d = l_m$	$\lambda = 75$m; $c_d = c_0^{-2}$; $c_0 = 3.3$ $c_m = 0.8$; $c_h = 0.2$; $c_n = c_0^{-1/2}$; $N^2 = \frac{g}{\theta}\frac{\partial \theta}{\partial z}$
MYJ	$K_{m,h,e} = l_m q S_{m,h,e}$ $q^2 = 2E$ $G_m = (l_m q^{-1} S)^2$ $G_h = -(l_m q^{-1} N)^2$ $S^2 = \left(\frac{\partial u}{\partial z}\right)^2 + \left(\frac{\partial u}{\partial z}\right)^2$	$l_m^{-1} = (\kappa z)^{-1} + \lambda^{-1}$ $\lambda = a u_* / f$ $l_d = l_m$	$c_d = B_1^{-1}$; $a = 0.0063$; $A_1 = 0.660$; $A_2 = 0.657$; $B_1 = 11.9$; $B_2 = 7.23$; $C_1 = 8.31e-4$ $S_m = A_1(1-3C_1-6A_1B_1^{-1}-3A_2G_h[(B_2–3A_2)(1-6A_1B_1^{-1}) - 3C_1(B_2+6A_1)])/[(1 - 3A_2G_h(6A_1 + B_2))(1 - 9A_1A_2G_h)]$ $S_h = A_2[1 - 6A_1B_1^{-1}]/[1 - 3A_2G_h(6A_1 + B_2)]$
QNSE	$K_{m,h} = c_2 \alpha_{m,h} l_m \sqrt{E}$ $K_e = K_m$	$l_m^{-1} = (\kappa z)^{-1} + \lambda^{-1} + l_N^{-1}$ $\lambda = 0.0063 u_* f^{-1}$ $l_N = 0.75\sqrt{E} N^{-1}$; $l_d = l_m$;	$\alpha_m = (1 + 8Ri^2)(1 + 2.3Ri + 35Ri^2)^{-1}$ $\alpha_h = (1.4 - 0.01Ri + 1.29Ri^2)(1 + 2.344Ri + 19.8Ri^2)^{-1}$ $c_d = c_2^3$; $c_2 = 0.55$
UKMO	$K_m = {l_M}^2 \frac{\partial U}{\partial z} f_m$ $K_h = K_m$	$l_m^{-1} = (\kappa z)^{-1} + \lambda^{-1}$ $\lambda = 0.0063 u_* f^{-1}$	$f_m = \begin{cases} 1 - 10Ri(1 + 0.4(-Ri)^{-0.5}) & \text{if } Ri < 0 \\ (1 - 5Ri)^2 & \text{if } 0 < Ri \leq 0.05 \\ \frac{1.6875}{1+40Ri} & \text{if } Ri > 0.05 \end{cases}$ $f_h = \begin{cases} 1 - 10Ri(1 + 2.5(-Ri)^{-0.5}) & \text{if } Ri < 0 \\ f_m & \text{if } Ri > 0 \end{cases}$
ECMWF	$K_{m,h} = {l_M}^2 \frac{\partial U}{\partial z} f_{m,h}$	$l_m^{-1} = (\kappa z)^{-1} + \lambda^{-1}$ $\lambda = 150$m	$f_m = \left[1 + 2bRi(1 + dRi)^{-1/2}\right]^{-1}$ $f_h = \left[1 + 2bRi(1 + dRi)^{1/2}\right]^{-1}$ $b = 5$; $d = 1$

Table 5.2: Complete parameterizations of turbulence closure schemes considered in this study.

near-surface resolution and an upper-altitude limit of 2000 m. The BVP solver then determines an optimal discretization on which a solution can be obtained. This discretization remains approximately uniform in logarithmic scale and generally contains between 200-400 levels. From the initial neutral profile, Eqs. 5.1(a)-(c) are integrated forward in time using a partial differential equation solver in the MATLAB software package ('pdepe', described at http://www.mathworks.com/help/matlab/ref/pdepe.html). The discretization from the initial neutral profile remains constant throughout the integration. For the 10-year composite analysis, the data are partitioned into 3-month datasets. We begin each dataset from a neutral profile as described above and neglect results obtained from the first 24 h of each 3-month simulation to account for model spin-up time. Note that less spin-up time is required for the LLJ case studies since the ABL quickly evolves from a neutral to an unstable state at 1200 UTC due to intense turbulent mixing.

We specify as lower boundary conditions the observed wind vector and temperature values at a specified altitude. For TKE-based closure, we adopt the approach in Weng and Taylor (2003) and Weng and Taylor (2006) and specify a lower boundary condition on the TKE by assuming the vertical turbulent flux of TKE is negligible near the surface compared to TKE production and dissipation (Stull, 1988). With this assumption, the TKE at 10 m is in equilibrium (i.e. $\partial E/\partial t = 0$) and using Eq. 5.8 is calculated as,

$$E = \left[\frac{l_d}{c_d}\left(-\overline{u'w'}\frac{\partial u}{\partial z} - \overline{v'w'}\frac{\partial v}{\partial z} + \frac{g}{\theta}\overline{\theta'w'}\right)\right]^{2/3} \tag{5.12}$$

We specify the 800 hPA winds from ERA-interim and a zero turbulent temperature flux as upper boundary conditions. For TKE-based closure, we specify an upper-boundary condition of zero for the vertical turbulent TKE flux.

5.3.3 Equilibrium SCM

Using observed external parameters at a given point in time (specifically the surface geostrophic wind, 10-m wind, and 5-m turbulent temperature flux), we begin from a neutral wind profile and integrate Eqs. 5.1 (a)-(c) forward in time while keeping the external parameters constant. We integrate for a period of 9 h to reach quasi-equilibrium, consistent with approaches used in other equilibrium SCM studies (Beare et al., 2006; Cuxart et al., 2006; Sorbjan, 2014). Methods used to solve for the neutral

profile and integrate Eqs. 5.1(a)-(c) are the same as described in the previous section. We assume an initial potential temperature of 295 K at all levels, noting that the value of temperature (in contrast to the temperature profile) is arbitrary and has negligible influence on model results.

We specify the 10-m wind vector and the 5-m temperature flux as lower boundary conditions at 10 m. For TKE-based closure, we calculate the TKE at 10 m using Eq. 5.12. For upper boundary conditions, we specify the surface geostrophic wind vector and a constant potential temperature of 295 K. For TKE-based closure, we specify an upper-boundary value of zero for the vertical turbulent TKE flux.

5.3.4 WRF model

Jimenez (2015) used the WRF mesoscale model (version 2.1.2) to obtain 10-m averaged wind vector and temperature profile data at the Cabauw site for the 2001-2010 period. These model results were provided for use in this study. The model is configured with four domains using two-way nesting (37x37 54 km horizontal resolution for the outer domain; 49x49 18 km for the first inner domain; 70x70 6 km for the second inner domain; 91x97 2 km for the innermost domain). There are 31 terrain-following hydrostatic pressure levels with the upper level at 50 hPa. The model includes parameterizations for longwave and shortwave radiation, cumulus clouds, and the land surface. The YSU turbulence parameterization scheme is used (Table 5.2). Initial and boundary conditions were obtained from the ECMWF reanalysis. A detailed discussion of the model and its configuration is presented in Jimenez et al. (2010).

5.4 LLJ case study results

We begin with considering model performance over the 8 LLJ case studies investigated by Baas et al. (2010), selected due to their relatively idealized conditions. Specifically, the case studies all occur in late spring or summer, and demonstrate clear sky conditions, strong surface cooling at night, reasonably constant geostrophic forcing from the south-east, and reasonably smooth rotation of the IO (indicative of minimal advective tendencies).

To facilitate the comparison of model results and observations, we apply the following smoothing function a total of 5 times to the time series data presented in this section,

$$X(t) = \frac{1}{4}X(t-1) + \frac{1}{2}X(t) + \frac{1}{4}X(t+1) \tag{5.13}$$

where $X(t)$ is the data at time t, and $X(t-1)$ and $X(t+1)$ are the data at the previous and following time steps.

5.4.1 Sensitivity to turbulence schemes

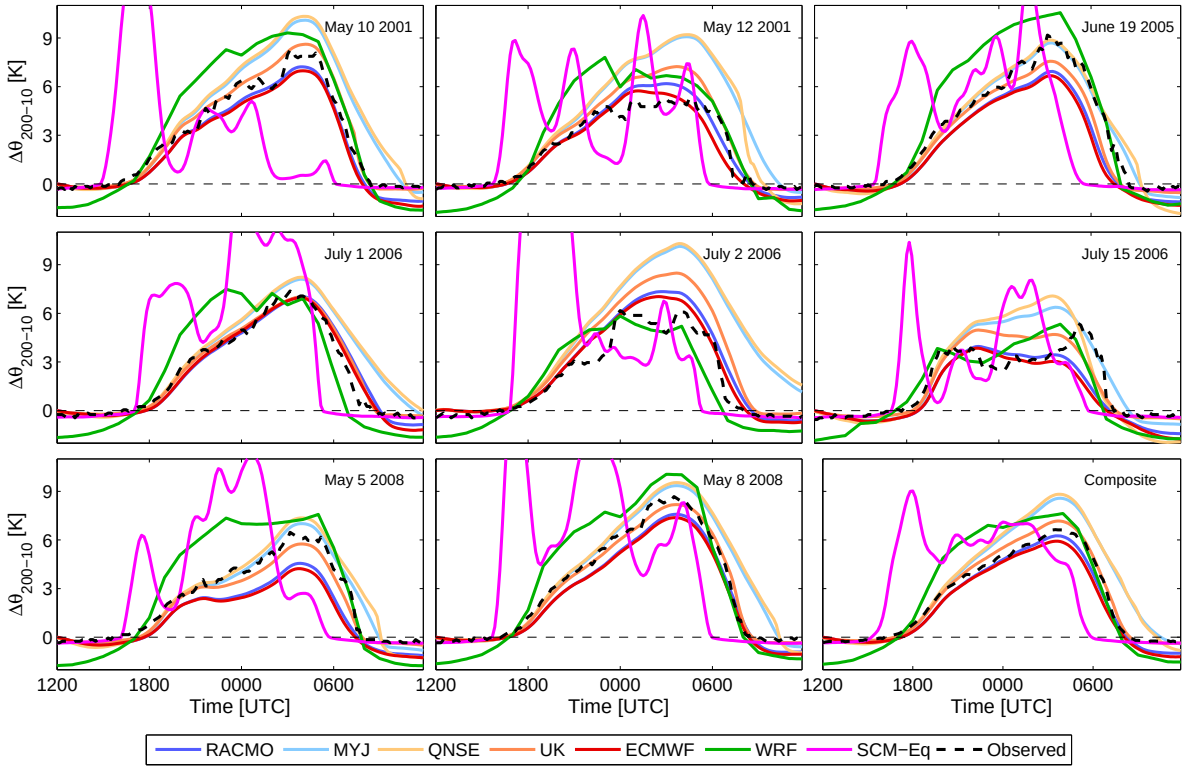

Figure 5.1: Evolution of the modelled and observed $\Delta\theta_{200-10}$ for the different LLJ case studies. The time-evolving SCM using different turbulence closure schemes, the WRF model, and the equilibrium SCM (denoted SCM-Eq) are considered.

The evolution of the modelled and observed potential temperature difference between 200-10 m ($\Delta\theta_{200-10}$) for the different case studies, as well as the averaged composite results, are shown in Fig. 5.1. In all cases, the lower 200 m of the ABL is weakly unstable from 1200 UTC up to around 1500-1700 UTC. The stable boundary layer then develops at about 1800 UTC reaching a peak generally around 0400 UTC. The transition back to unstable conditions occurs between 0700-0900 UTC.

Fluctuations of the observed $\Delta\theta_{200-10}$ over 1-2 h timescales in the individual case studies (possibly caused by advective tendencies, intermittent turbulence, etc.) are largely averaged out in the composite case. The different models demonstrate a range of modelled stratifications. For the time-evolving SCM, the RACMO and ECMWF schemes tend to slightly underestimate $\Delta\theta_{200-10}$ during the stable regime and tend to overestimate $|\Delta\theta_{200-10}|$ after sunrise. We attribute this result to the fact that the RACMO and ECMWF schemes (as used in this study) do not incorporate a stability function for unstable conditions. The strength of turbulent mixing for these schemes is limited to that attainable in neutral conditions, and the resulting inability to sufficiently transport warmer surface air aloft results in the $|\Delta\theta_{200-10}|$ bias. The UKMO scheme shows good agreement with observations apart from a slight tendency to overestimate $\Delta\theta_{200-10}$ from the late evening up to the peak stratification. The inclusion of a stability function for unstable conditions for the UKMO scheme allows for an accurate representation of the stratification during the day. The MYJ and QNSE schemes overestimate stratification from early evening onwards and model the sunrise transition on average 2-3 h later than the observed transition time. We attribute this delay to the increased time required to break up the intense stratification up to 200 m. The WRF model is generally less accurate in modelling the stratification compared to the time-evolving SCMs. Specifically, the WRF model tends to substantially overestimate $|\Delta\theta_{200-10}|$ at all times of day apart from the 2-3 h period before the sunrise transition. This tendency may be attributed to insufficient turbulent mixing in the WRF model for both unstable and stable conditions. The equilibrium SCM accurately accounts for the stratification during the day but shows poor accuracy at night. Specifically, large spikes in $\Delta\theta_{200-10}$ are common, corresponding to large magnitudes of the 5-m $\overline{\theta' w'}$ values particularly common around the sunset transition. Furthermore, the modelled sunset and sunrise transitions occur immediately following the change of sign of $\overline{\theta' w'}$ at 5 m, earlier than the observed transitions by about 2-3 h.

The evolution of the modelled and observed 200-m wind speeds (U_{200}) for the different case studies, as well as the averaged composite results, are shown in Fig. 5.2. Hodographs of the 200 m wind vector are shown in Fig. 5.3 along with the composite hodograph determined using the approach in Baas et al. (2010). The observed 200-m wind speeds increase in magnitude at around 1600-1800 UTC consistent with the onset of stable stratification and reduced surface coupling. The peak in the wind speed occurs around 2200-0000 UTC due to the formation of a LLJ near 200 m (Baas

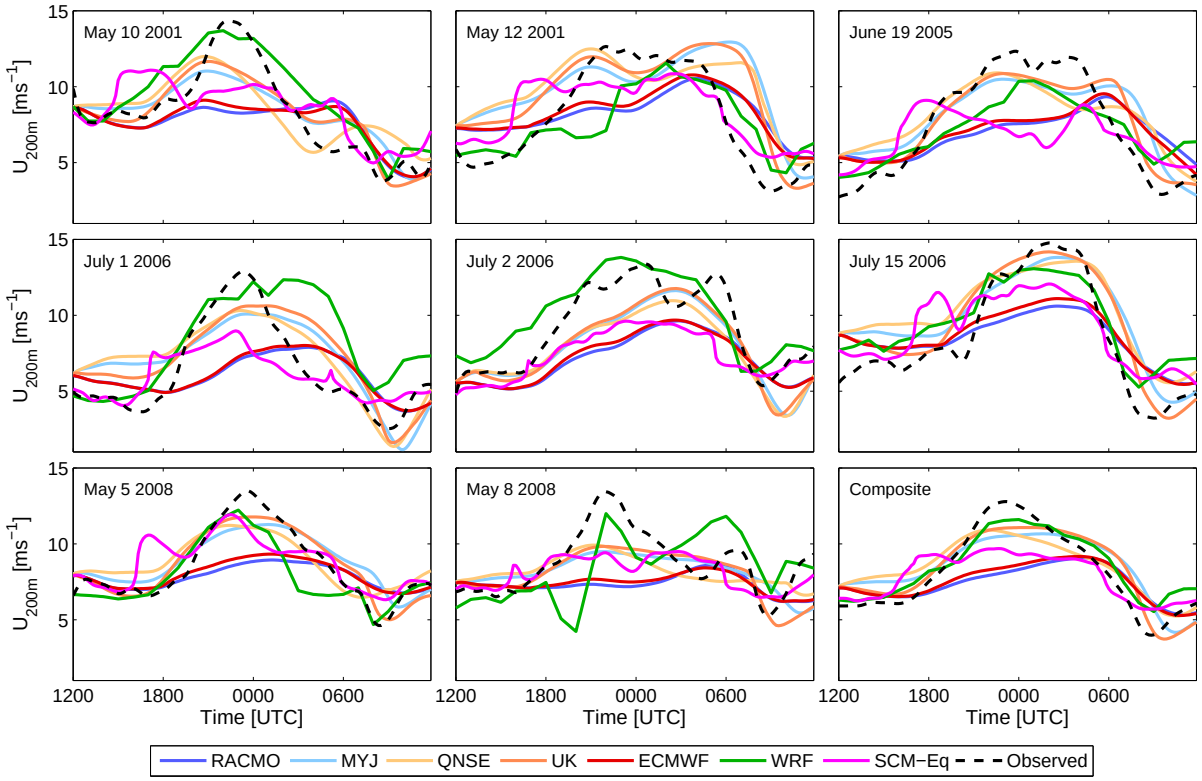

Figure 5.2: Same as Fig. 5.1 but showing the 200-m wind speeds.

et al., 2010). The wind speed then decreases and reaches a minimum at the sunrise transition. As demonstrated in Figs. 5.2 - 5.3, the evolution of U_{200} over the course of the night is strongly associated with the evolution of the IO. Fluctuations of the observed U_{200} over 1-2 h timescales in the individual case studies (possibly caused by advective tendencies, intermittent turbulence, etc) are largely averaged out in the composite case. The time-evolving SCM and the WRF model generally show reasonable agreement with the observations (apart from the RACMO and ECMWF schemes), although both schemes underestimate the magnitude of the IO and consequently the peak wind speed. The observed wind speeds tend to decrease after the peak sooner than the modelled wind speeds. Baas et al. (2010) attributed this result to a consistent pattern in momentum advection observed over the case studies, which they speculated were caused by a combination of sea, lowland, and mountain range effects. Compared to the time-evolving SCM, the WRF model shows results of similar quality for the composite case but much different results in the individual case studies. The WRF model is more accurate in some cases relative to the SCMs,

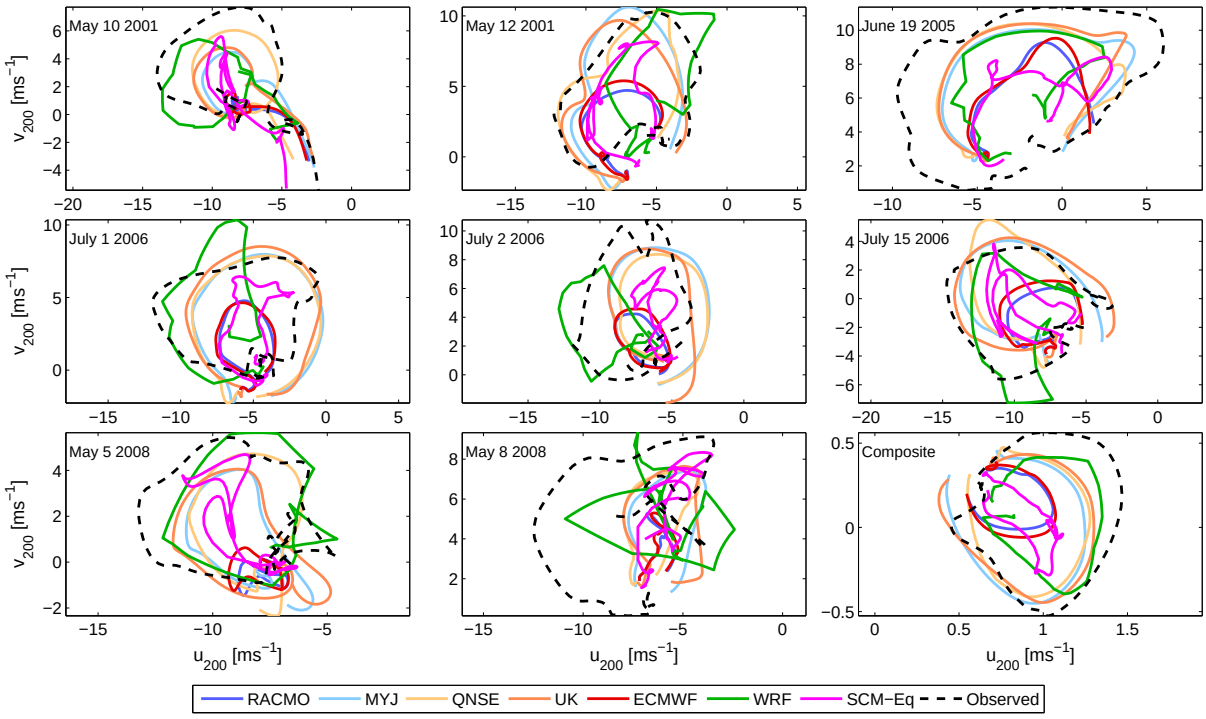

Figure 5.3: Same as Fig. 5.1 but showing hodographs of the 200-m wind vector.

and other times is less accurate. This result is not surprising given that, in contrast to the SCMs, the WRF model is not driven by local observations and can in principle account for 3D processes such as momentum advection. The equilibrium SCM generally shows poor agreement with observations. The increase in wind speed at night is underestimated and occurs about 2 h earlier than the observed increase. Furthermore, there is no clear IO development. This result is not surprising given that the equilibrium SCM is not time-evolving, and is by construction unable to account for the IO. Despite these limitations, the equilibrium SCM is about as accurate as the time-evolving RACMO and ECMWF SCMs.

5.4.2 SCM sensitivity to changes in the lower boundary height

We will now explore the sensitivity of the time-evolving SCM to two different representations of the lower boundary. The first representation uses the roughness length z_0 as the height of the lower boundary, with $u_{LB} = 0$, $v_{LB} = 0$ and the 2 m temperature values acting as boundary conditions. We consider 3 values of z_0. The first

value ($z_0 = 0.15$ m) used in Bosveld et al. (2014a) is intended to be representative of mesoscale roughness. The other z_0 representations are an order of magnitude above and below the mesoscale value (i.e. $z_0 = 0.015$ m and $z_0 = 1.5$ m). We select this broad range due to the fact that z_0 is a poorly constrained parameter that can vary by an order of magnitude depending on the method used to determine its value (Chapter 2). The second representation of the lower boundary uses altitudes above the surface, with the wind vector and temperature at that altitude as boundary conditions. We consider 3 different heights above the surface (10 m, 40 m, and 80 m) to determine to what extent the use of higher altitudes improves the accuracy of the modelled wind speeds aloft. We consider in this analysis only the composite results averaged over the 8 LLJ case studies and consider only the UKMO turbulence scheme given its good performance relative to other schemes demonstrated in the previous section.

Observed and modelled wind speeds at 80 m (i.e. U_{80}) are shown in Fig. 5.4(a). Higher values of z_0 lead to lower values of U_{80} throughout the day and earlier minimum wind speeds at the sunset transition, both of which can be attributed to increased turbulent mixing. The observed U_{80} is generally well represented with the $z_0 = 0.15$ m formulation, supporting the fact that mesoscale roughness features are influencing the winds and turbulence at 80 m. The use of observed wind speeds at altitudes above the surface generally results in improved representations of U_{80} compared to the z_0 approaches, particularly at the sunrise minimum (the 80-m SCM case is of course exact).

Observed and modelled turbulent momentum fluxes at 100 m (i.e. τ_{100}) are shown in Fig. 5.4(b) averaged over the May 5 2008 and May 8 2008 case studies (for which observed momentum flux data at 100 m was available). All models generally underestimate τ_{100} during the day, which can be explained by the fact that the SCM does not incorporate non-local transport and will therefore tend to underestimate τ_{100} in very unstable conditions. Higher values of z_0 lead to higher values of τ_{100} as expected, while higher altitudes for the lower boundary tend to produce larger values of τ_{100} during the day. This result is also expected given that wind speeds at higher altitudes are more representative of mesoscale roughness and less influenced by the IBL. During the night, the models tend to overestimate turbulent mixing and the $z_0 = 0.015$ m lower boundary is generally most accurate. These results suggest a tendency for the UKMO scheme to overestimate turbulent mixing at night for these 2 case studies, consistent with the tendency to underestimate stratification (Fig. 5.1). The 80-m SCM approach mitigates this tendency and reasonably accounts for the low

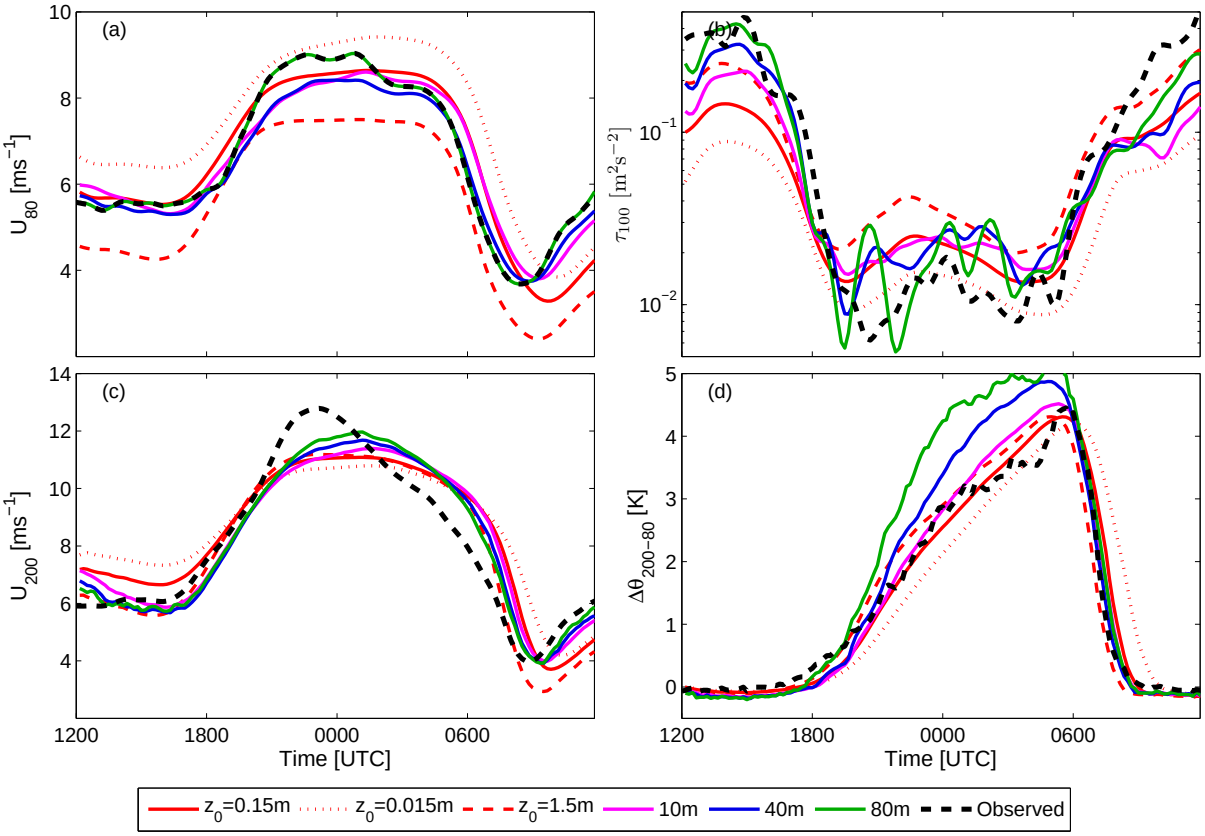

Figure 5.4: Time-evolving SCM results averaged over the LLJ case studies and considering different lower boundary heights. The figures shows the time evolution of: (a) the 80-m wind speed, (b) the 100-m turbulent momentum flux, (c) the 200-m wind speed, and (d) $\Delta\theta_{200-80}$.

τ_{100} values despite large variability.

The 200 m wind speeds are shown in Fig. 5.4(c). Higher values of z_0 result in lower wind speeds during the day as expected, but result in larger wind speeds during the night and a larger magnitude IO (although the differences at night are rather negligible). We attribute this reversal to the fact that the magnitude of the IO depends on the degree of departure of the wind profile around sunset to its equilibrium profile at night. Higher values of z_0 result in a more turbulent ABL at sunset, and therefore the departure from the nocturnal equilibrium profile is larger compared to smaller z_0 values. The observed U_{200} during the day generally falls between that estimated using $z_0 = 0.15$ m and $z_0 = 1.5$ m (apart from the time after sunrise), which suggests a higher regional roughness affecting the winds and turbulence at 200 m than

represented by $z_0 = 0.15$ m that is generally cited (e.g. Holtslag 1982; Verkaik and Holtslag 2007; Bosveld et al. 2014a). Higher altitudes for the lower boundary result in moderate improvements in modelling U_{200} and in particular better representation of the LLJ magnitude. These results demonstrate that the use of observed wind speeds at 10 m and above as a lower boundary improves the simulation at transition times, mitigating excessive or insufficient turbulent mixing produced using a no-slip boundary condition at z_0.

Finally, observed and modelled $\Delta\theta_{200-80}$ values are shown in Fig. 5.4(d). Higher z_0 values result in faster erosion of stable stratification as expected due to increased turbulent mixing. Interestingly, the use of higher altitudes for the lower boundary results in increased tendencies to overestimate stratification. The reasons for this effect are unclear.

Overall, the use of lower boundaries above the roughness length tends to improve modelling of wind speeds aloft, and in particular tends to mitigate the effects of excessive or insufficient turbulent mixing. The 10-m SCM approach was slightly less accurate in modelling the 200 m wind speeds compared to the 80-m SCM approach but better accounted for stratification. The higher performance of the 10-m SCM approach is an interesting and valuable results given that winds and temperature are more easily measured at this altitude than aloft.

5.5 10-year dataset results

Having compared the equilibrium SCM, the time-evolving SCM, and the WRF model for the LLJ case studies, we now consider their performance over the entire 10-year dataset. For the time-evolving SCM calculations, we use the UKMO turbulence closure scheme which was shown to be the most accurate for the LLJ case studies. The UKMO scheme also has the added benefit of being a simpler first-order closure scheme and therefore allows faster computation over the large data set compared to a prognostic TKE scheme. For the time-evolving SCM, we only carry out computations with specified winds at a given altitude (10 m, 40 m, and 80 m; denoted respectively SCM-10, SCM-40, and SCM-80) based on the improved performance over surface roughness approaches demonstrated in the previous section. We assess model performance within different stability classes based on the observed bulk Richardson

number determined between 200 m and the surface (Table 5.3),

$$Ri_B = \frac{g}{\theta_{avg}} \frac{z_{200}(\theta_{200} - \theta_{surf})}{U_{200}^2} \tag{5.14}$$

where θ_{avg} is the average potential temperature in the lower 200 m. We exclude data where the 200-m wind speed is less than 5 ms^{-1}. Under such conditions, flux-gradient relationships are known to perform poorly (Mahrt, 1998). Furthermore, equilibrium SCM breakdown is frequent under such conditions given the weak turbulence, as shown in Chapter 4. Finally, low wind-speed conditions are not of interest for wind power applications, so the accuracy of different wind-speed profile models under these conditions is not relevant in the present context. To make meaningful comparisons between models, the statistics describing model performance in this section include only the time intervals for which results are available for all models.

Stability class	Ri_B range
Weakly stable	$0 < Ri_B < 0.05$
Moderately stable	$0.05 < Ri_B < 0.15$
Very stable	$0.15 < Ri_B < 0.5$
Extremely stable	$Ri_B > 0.5$

Table 5.3: Stability classes considered in this analysis, based on Ri_B.

Mean wind speed profiles are shown in Fig. 5.5. With increasing stratification, the observed wind speeds decrease on average and demonstrate a mean LLJ around 140 m in extremely stable conditions. In general, the time-evolving models show reasonable agreement with the mean observations while the equilibrium SCM is less accurate. In weakly stable conditions, the WRF model shows good agreement with observations while the equilibrium and time-evolving SCMs all overestimate the wind speed due to the influence of the IBL. This effect is mitigated but not eliminated in the time-evolving SCM by using higher-altitude lower boundaries. These results indicate stronger than expected mixing in weakly stable conditions above 80 m which was also demonstrated in Chapter 4. In moderately stable conditions, the influence of the IBL is reduced and the SCMs show much better agreement with observations. The WRF model is accurate above 100 m but overestimates wind speeds below this altitude, likely caused by excessive turbulent mixing at low altitudes due to the inability of WRF to resolve the IBL. In very stable conditions, all models are accurate (apart from the WRF model below 50 m). In extremely stable conditions, none of the models are

able to account for the mean LLJ. However, the time-evolving SCM and WRF model show good agreement with observations up to about 140 m and overestimate wind speeds above this altitude. The equilibrium SCM (denoted SCM-Eq) underestimates wind speeds up to 140 m and overestimates wind speeds above this altitude.

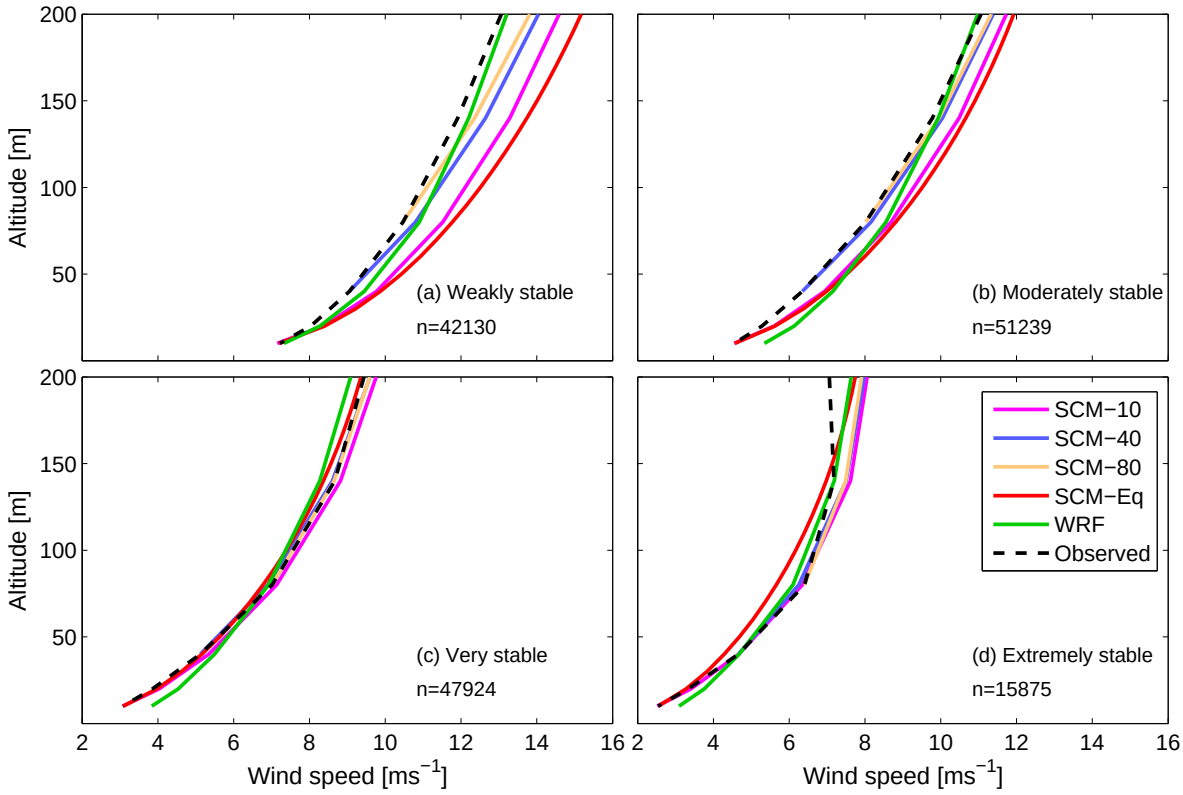

Figure 5.5: Mean modelled and observed wind speed profiles for the different stability classes for the 10-year data set. The letter 'n' denotes the number of values included in the mean.

Box plots of the relative difference between modelled and observed wind speeds at 200 m are shown in Fig. 5.6 for the different stability classes. In general, the spread between observed and modelled wind speeds increases with stratification. Overall, the equilibrium SCM demonstrates the least spread across all stability classes, particularly in weakly and extremely stable conditions. For the time-evolving SCM, less spread is produced when higher-altitude lower boundaries are used. The WRF model generally shows spread similar to that found for the time-evolving SCM. The lower spread found for the equilibrium SCM is a surprising result, given the poor performance of the equilibrium SCM in the LLJ case studies. Time-evolving models are expected

in principle to perform better than an equilibrium model in stable stratification, particularly in very to extremely stable conditions where accounting for the time-evolving IO and LLJ are important.

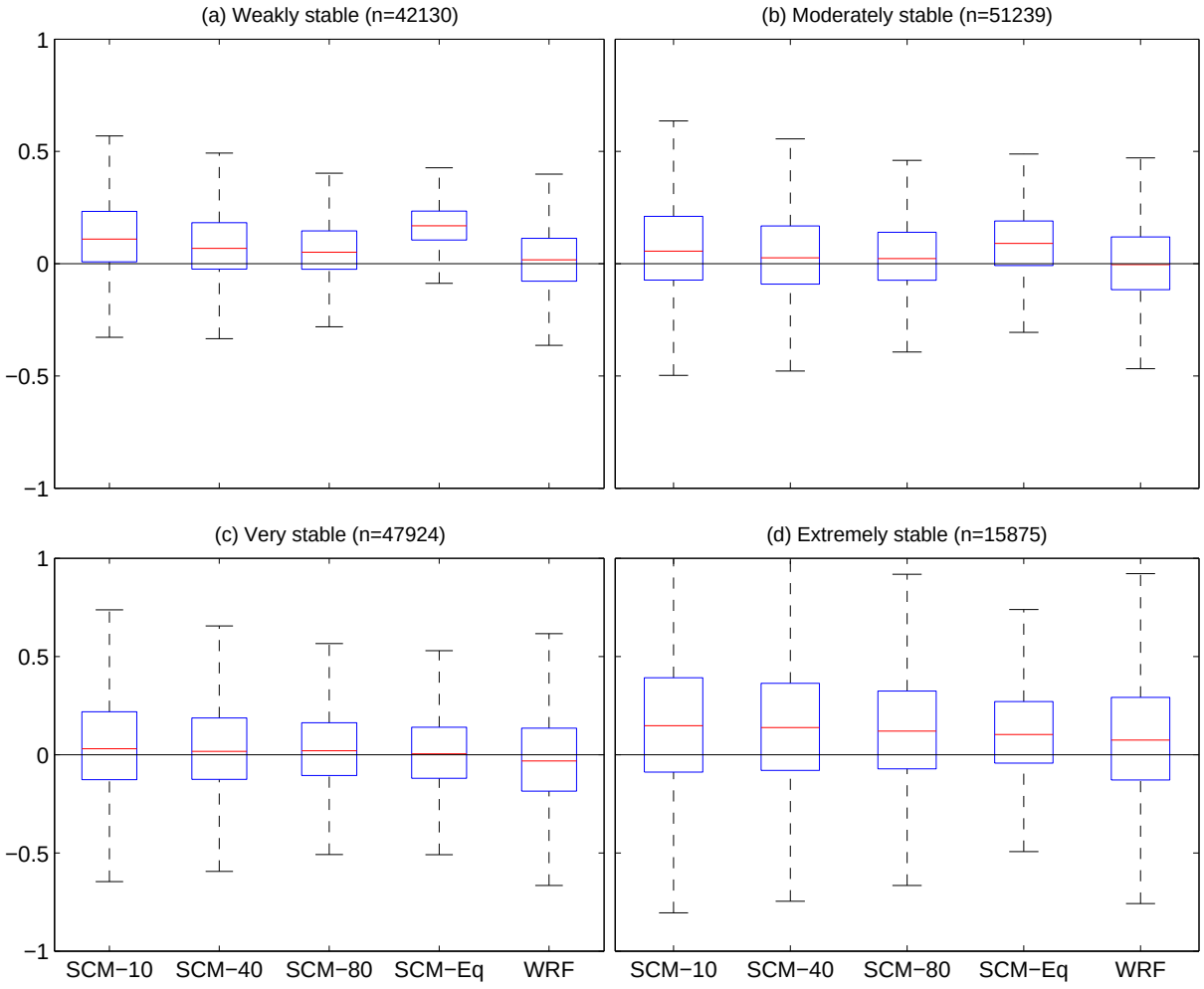

Figure 5.6: Box plots of the relative difference between modelled and observed winds (i.e. $(U_{mod}-U_{obs})/U_{obs}$) at 200-m for the different stability classes. The red lines show the mean values, blue boxes show the interquartile range, and black dotted lines show the total range excluding outliers.

The difference in spreads in Fig. 5.6 for the different models can be attributed in part to how well the different models account for stratification. In Fig. 5.7 we show joint PDFs of the difference in the modelled and observed $\Delta\theta_{200-10}$ values (i.e. $\Delta\theta_{mod} - \Delta\theta_{obs}$) with the difference in the modelled and observed wind speeds at

200 m (i.e. ΔU_{200}) for the different models and stability classes. Note that we do not consider the time-evolving SCM-40 and SCM-80 in this analysis. In general, the spreads in wind speed error and stratification error both increase in higher stability classes. Several PDFs demonstrate a correlation between ΔU_{200} and $\Delta\theta_{mod} - \Delta\theta_{obs}$: the time-evolving SCM from weakly to very stable conditions, and the equilibrium SCM from moderately to very stable conditions. If this correlation arises because the stratification error causes the error in the wind profile, or if they have a common cause, it is expected that improved modelling of the stratification in these cases would lead to some reduction in the mean 200-m wind speed error. In extremely stable conditions, no clear relationship between ΔU_{200} and $\Delta\theta_{mod} - \Delta\theta_{obs}$ is found for any of the models. In this regime, wind speed error can be attributed to other factors as discussed in the Introduction (e.g. gravity waves, intermittent turbulence, etc.). We also note the tendency of the equilibrium SCM to underestimate stratification in higher stability classes, reasons for which were described in Chapter 4 and are also discussed in Sect. 5.6. Overall, the performance of the time-evolving SCM (which demonstrates the most association between wind speed and stratification error) would be most improved from a better accounting of the modelled stratification. Conversely, it appears that such a change would have little effect on the performance of WRF.

The large spread in stratification error found for the time-evolving SCM can be attributed in large part to its inability to account for horizontally-driven temperature changes in the ABL (e.g. warm or cold fronts, temperature advection). We demonstrate this fact in Figs. 5.8 - 5.9 using 3-week time periods in both winter and late spring. For the winter case (Fig. 5.8) there is evidence of warm-air temperature advection from the North Sea causing the 200-m temperature to increase at night while the 10-m temperature decreases due to surface cooling (e.g. January 2 and January 5). By construction, the time-evolving SCM - driven by the lower boundary wind and temperature observations - attributes changes in temperature to vertical processes (i.e. surface heating or cooling). As a result, the time-evolving SCM simulates unstable conditions when the 10-m temperatures are increasing (e.g. January 5-9) and is unable to account for the diverging temperatures at the surface and aloft due to temperature advection. Overall, the time-evolving SCM poorly accounts for stratification over the 3-week period. The equilibrium SCM shows little to no improvement in the modelled stratification, but more importantly demonstrates frequent model breakdown (reasons for which were described in Chapter 4). The WRF model - which can account for horizontally-driven temperature changes - shows

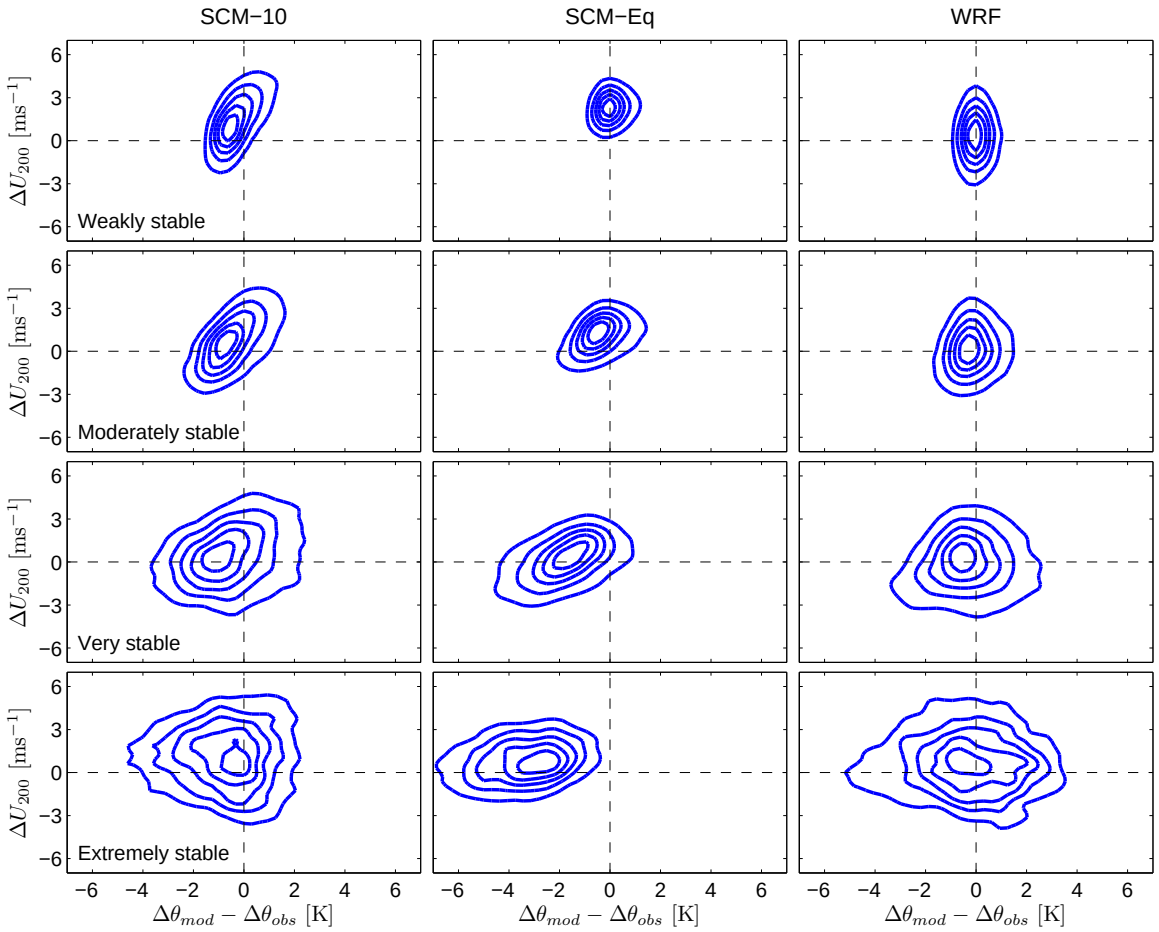

Figure 5.7: Joint PDFs of the difference in modelled and observed stratifications between 200-10 m and the difference in modelled and observed wind speeds at 200 m. We consider the time-evolving SCM with a 10 m lower boundary, the equilibrium SCM, and the WRF model in the different stability classes.

much better agreement with the observed stratification over the 3-week period.

For the late spring case (Fig. 5.9), the observed 200-m and 10-m temperatures show a clear diurnal pattern: the temperatures at 10 m and 200 m are similar during the day while the 10-m temperature decreases more rapidly than the 200-m temperature during the night. Within the 3-week period, there are periods of both net cooling and heating over timescales of several days. When temperatures in the lower ABL are decreasing (e.g. April 29 onwards), the time-evolving SCM tends to overestimate stratification which can persist for several days. The equilibrium SCM breaks

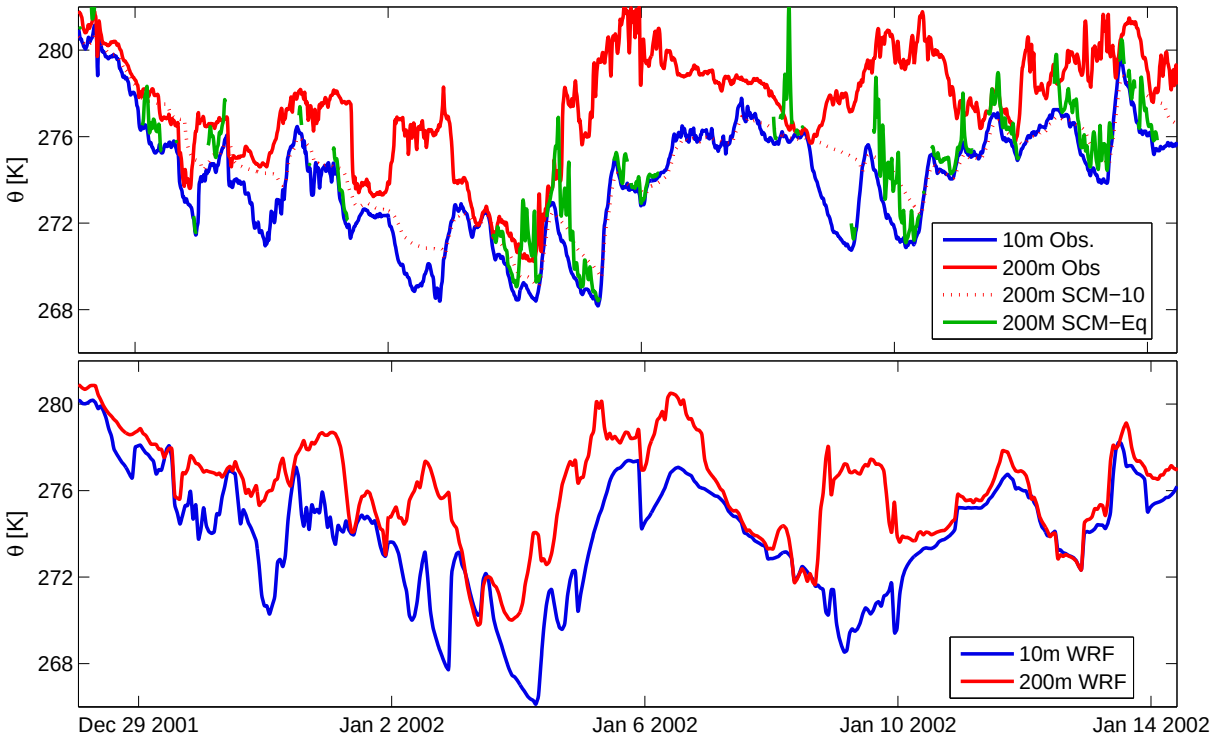

Figure 5.8: Evolution of the modelled and observed θ values at 200 m and 10 m for a specified time period in winter. In the upper panel, observed values are shown in solid red (200 m) and blue (10 m), time-evolving SCM results at 200 m are shown in dotted red, and equilibrium SCM results at 200 m are shown in solid green. In the lower panel, WRF model results are shown in red (200 m) and blue (10 m).

down often over this period, highlighting its limited usefulness. The WRF model is generally very accurate in capturing the evolving stratification for the spring case. We note that the use of lower boundaries at 40 m or 80 m for the time-evolving SCM can mitigate the influence of temperature advection, but results in only modest improvements in the modelled stratification.

5.6 Discussion

The equilibrium SCM was shown in this analysis (and in Chapter 4) to be of very limited value and applicability in wind profile modelling due to frequent model breakdown, its bias towards low stratification, and its inability to accurately account for

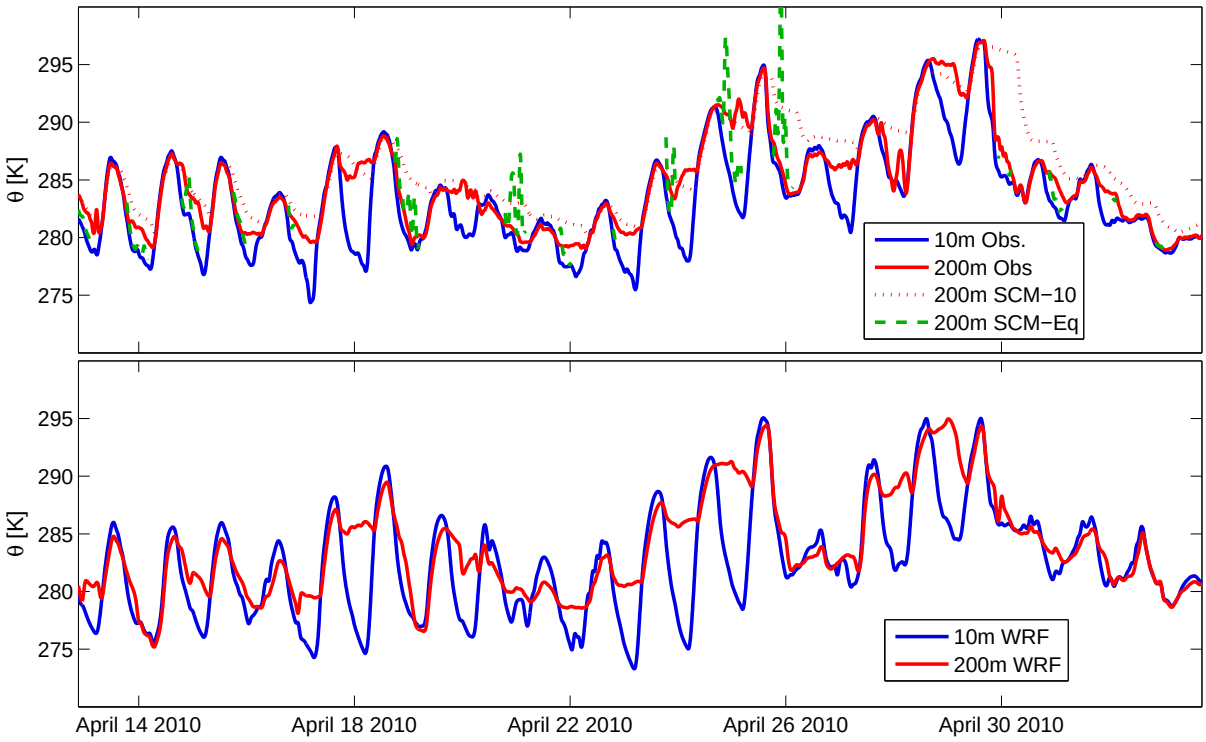

Figure 5.9: Same as Fig. 5.8 but for a spring case.

fundamentally time-evolving processes such as the IO and LLJ. Despite these serious limitations, the equilibrium SCM demonstrated less spread in the wind speed error compared to the time-evolving SCM over the 10-year dataset. This result can likely be attributed to the different lower boundary conditions used in the SCMs and their relative sensitivities to horizontally-driven temperature changes in the ABL. Consider an idealized example where a uniform temperature change is observed at all altitudes resulting in no change in the observed stratification. The near-surface $\overline{\theta' w'}$ value (as used in the equilibrium SCM) would remain constant during such a process, as would a modelled wind profile based on this value. Conversely, a model driven by lower boundary temperature values (i.e. the time-evolving SCM) would simulate the development of stable stratification when the ABL temperature decreases and unstable stratification when the ABL temperature increases, resulting in some degree of bias in the modelled wind profile. This simple example demonstrates considerable value in the inclusion of some observed measure of stability in the SCM model. The use of $\overline{\theta' w'}$ as a measure of stability is problematic as it often results in model breakdown or

model attraction towards the more weakly stable of two physically meaningful solutions (van de Wiel et al., 2007). Conversely, the use of temperature measurements at two altitudes provides an unambiguous account of stability (Gibbs et al., 2015). The extent to which the time-evolving SCM can be improved by including temperature measurements at two near-surface altitudes (e.g. 10 m and 20 m) would be a useful next step in this research. We note, however, that such an approach would likely not improve model performance in cases where differential temperature changes at the surface and aloft are observed (i.e. diverging 10-m and 200-m temperatures in Fig. 5.8).

The presence of a local IBL is an important factor for wind profile predictions accounting only for processes in the vertical. The presence of such IBLs structure is not unique to Cabauw, but would exist in other locations with a low local roughness but higher regional roughness. In this study, SCM performance was improved by using a higher-altitude lower boundary where wind speeds and turbulence were less influenced by the local IBL. The use of higher altitude measurements is not necessarily a practical difficulty: tower measurements up to 100 m are common during wind resource assessments in complex terrain, and in the context of forecasting, wind and temperature measurements are generally made at hub-height on a wind turbine nacelle. The standard approach to mitigate the effect of IBLs is to use a surface lower boundary with a higher z_0 value to account for regional roughness. However, as demonstrated in this study, the specification of z_0 is ambiguous in inhomogeneous terrain given that the value resulting in the most accurate simulation of turbulence aloft can change significantly over the course of the day. Another approach to account for the IBL would be to add a parameterization to the SCM to model the influence of the IBL. However, such an approach is not straightforward as it would need to take into account wind direction and stratification, and would be fundamentally tuned to a particular site with likely limited application at a different location.

Overall, the time-evolving SCM performed well in the idealized LLJ case studies in which the influence of 3D processes was minimized, but showed comparatively less skill over the 10-year data set where 3D processes were generally more influential. Fundamentally, a 1D-approach is inherently limited in its ability to account for 3D processes. Yet despite these limitations and its simplified physics, the time-evolving SCM was generally found to be equally as accurate as a 3D mesoscale model over the 10-year data set, and more accurate over the LLJ case studies. Furthermore, the SCM required only a small fraction of the computational cost of the WRF model and

only a minimal amount of local (and easily attainable) observational data. This result clearly highlights the value of local observations in estimating a local wind profile. As a next step, it would be useful to extend this analysis to a range of locations (e.g. complex terrain, offshore, northern climates, etc.) to further assess the robustness of an SCM approach relative to a mesoscale model.

Regarding the performance of the WRF model, we note that the YSU turbulence scheme used in the model (based on Monin-Obukhov similarity theory and modified for application to the entire ABL) has been shown to be the least accurate of the WRF turbulence parameterizations for stable conditions (Draxl et al. 2014). It is possible that a more accurate turbulence scheme (e.g. MYJ) would improve the performance of WRF in this analysis.

In this and the previous chapters, we have provided a detailed analysis of different approaches to modelling the wind profile up to 200 m under stable stratification. Overall, the time-evolving SCM model has been found to perform the best (considering both accuracy and robustness) compared to a range of equilibrium approaches (i.e. MOST (and its various modifications), two-layer model, equilibrium SCM) as well as a time-evolving 3D model, while offering the best balance of observational data requirements, physical applicability, and computational requirements. Simplified equilibrium-based analytic models required some measure of stability (i.e. turbulent flux observations, wind and temperature measurements at two different altitudes) and were shown to break down in strongly stable conditions. The 3D WRF model required much more data compared to the other models (i.e. synoptic boundary conditions, surface characteristics) but did not make use of local observations and had high computational cost. The SCM was found to provide a viable middle ground between these two approaches, providing accuracy as high or better than the analytic or mesoscale models (and with considerable room for improvement), while requiring a modest amount of computing power and minimal and easily attainable local observations.

5.7 Conclusions

In this study, we compared three different approaches to modelling the wind profile from 10 m to 200 m, and compared model results to observations obtained from the Cabauw meteorological tower in the Netherlands. The models considered included an equilibrium SCM, a time-evolving SCM (with a range of different turbulence parame-

terizations), and a time-evolving 3D mesoscale model (WRF). Using a composite data set of low-level jet (LLJ) case studies, we found that the time-evolving SCM and the WRF model accurately simulated on average the evolving stratification, the inertial oscillation, and the LLJ. The equilibrium SCM was shown to have comparatively less skill due to its inability to accurately account for time-evolving processes. Over the full 10-year data set, both the equilibrium and time-evolving SCMs overestimated wind speeds in weakly and moderately stable conditions due to the influence of the IBL but were more accurate in the higher stability classes. Model performance in all stability classes was limited by the inability of the SCM to account for fundamentally 3D effects such as horizontal temperature advection. Frequent model breakdown and the tendency to underestimate stratification limited the usefulness of the equilibrium SCM. Despite its various limitations and simplified physics, the SCM approach was generally found to be equally as accurate as the WRF model while using a fraction of the computational cost and requiring only a minimal amount of easily attainable local observations. Results from this study make a compelling case for the use of SCMs in wind resource assessment and forecasting.

Chapter 6

Conclusions

This thesis has compared the ability of several models of varying complexity to model the wind speed profile up to 200 m under stable stratification. The models considered ranged from the equilibrium-based 1D logarithmic wind speed profile to a time-evolving 3D mesoscale model. I focused in particular on the middle ground between these two approaches: a two-layer model and both equilibrium and time-evolving SCMs. Models were driven by and compared to data from the Cabauw meteorological tower in the Netherlands.

6.1 Main results

In Chapter 2, I demonstrated the limitations of similarity-based approaches to wind speed extrapolation and their breakdown under increasingly stable stratification. I first demonstrated the sensitivity of the logarithmic wind speed model to the specification of the roughness length, z_0, and the tendency of a surface flux-derived Obukhov length to overestimate the magnitude of stability aloft in the presence of IBLs. I then showed that z_0 is not required in the logarithmic wind speed model provided wind speed measurements are available at some lower altitude. I further demonstrated that using a bulk form of the Obukhov length measured between two near-surface altitudes provided significant improvements in wind speed extrapolation accuracy compared to the standard surface flux-based approach. The breakdown of MOST above the SL was then demonstrated, in particular the divergence of the stability function at high stratification, the rotation of the wind vector with altitude due to the Coriolis force, and the degree of surface decoupling from winds aloft. Various proposed modifica-

tions to the logarithmic wind speed model were found to provide little improvement in wind profile accuracy.

In Chapter 3, I compared various similarity-based models to the two-layer model. The logarithmic wind-speed profile was found to be reasonably accurate up to moderately stable conditions but became increasingly inaccurate at higher stratification. Local similarity-based profiles showed considerable improvement across all stability ranges, but were substantially more data-intensive. The two-layer model provided the best balance of low bias and variance for the entire stability range, and required only the 10-m wind speed, the geostrophic wind and surface bulk Richardson number as input parameters.

In Chapter 4, I explored the use of an equilibrium SCM for wind profile modelling and compared its performance to the two-layer model. Several limitations to the equilibrium approach were demonstrated. First, the equilibrium SCM broke down frequently due to a range of factors. Second, model attraction towards the more weakly stable of two possible equilibrium solutions for a given value of the surface turbulent temperature flux (used as a lower boundary in the SCM) generally resulted in a tendency to underestimate stratification. Finally, the equilibrium approach was by design unable to accurately account for time-evolving phenomena such as the inertial oscillation and LLJ. I further demonstrated in this study no clear association between the accuracy of the wind profile and the order of turbulence closure used in the SCM. Rather, the accuracy of the diffusivity coefficient varied across all orders of turbulence closure and had predominant influence on wind profile accuracy. Baroclinic influences due to the land-sea temperature gradient were shown to have only modest influence on the wind speed profile below 200 m in stable conditions. The IBL at Cabauw resulted in a strong tendency for the SCM to overestimate wind speeds in weakly to moderately stable conditions. In very stable conditions (where the IBL influence was low), SCM accuracy was improved. Despite its serious limitations, the equilibrium SCM (when it did not break down) was found to generally outperform a highly-tuned two-layer logarithmic-Ekman model.

In Chapter 5, I compared the equilibrium SCM to a time-evolving SCM and a time-evolving 3D mesoscale model (WRF) using a composite dataset of LLJ case studies as well as the 10-year dataset at Cabauw. For the LLJ case studies, the time-evolving SCM and the WRF model were found to accurately simulate on average the evolving stratification, the inertial oscillation, and the LLJ. The equilibrium SCM was shown to have comparatively less skill due to its inability to accurately account for

time-evolving processes. Over the full 10-year data set, both the equilibrium and time-evolving SCMs overestimated wind speeds in weakly and moderately stable conditions due to the influence of the IBL but were more accurate in the higher stability classes. The sensitivity of the time-evolving SCM to horizontally-driven temperature changes in the ABL was a considerable limitation. Yet despite its various limitations and simplified physics, the time-evolving SCM approach was generally found to be equally as accurate as the 3D WRF model while using a fraction of the computational cost and requiring only a minimal amount of easily attainable local observations.

Overall, the time-evolving SCM model has been found to perform the best (considering both accuracy and robustness) compared to a range of equilibrium approaches as well as a time-evolving 3D model, while offering the best balance of observational data requirements, physical applicability, and computational requirements. Simplified equilibrium-based analytic models required some measure of stability (i.e. turbulent flux observations, wind and temperature measurements at two different altitudes) and were shown to break down in strongly stable conditions. The 3D WRF model required much more data compared to the other models (i.e. synoptic boundary conditions, surface characteristics) but did not make use of local observations and had high computational cost. The SCM was found to provide a viable middle ground between these two approaches, providing accuracy as high or better than the analytic or mesoscale models (and with considerable room for improvement), while requiring a modest amount of computing power and minimal and easily attainable local observations.

6.2 Limitations and future work

There are several limitations to the work presented here which demonstrate the need for additional research in several areas.

The absence of some measure of stability in the lower boundary values of the time-evolving SCM was a significant limitation, specifically during observed ABL temperature changes driven by horizontal influences (i.e. advection). The inclusion of temperature measurements at an additional near-surface altitude should considerably improve model accuracy under such conditions, and would be a useful next step in this research

The WRF model made use of the YSU turbulence scheme, shown to be the least accurate of the WRF turbulence parameterizations for stable conditions (Draxl et al.

2014). In this regard, the comparison of WRF to the SCMs was somewhat biased given that the SCMs made use of the most accurate of a range of turbulence schemes considered. A sensitivity analysis of WRF results to different turbulence schemes (e.g. QNSE, MYJ) over the 10-year data set would allow for a more robust comparison between WRF and the SCM approaches.

The SCM approach is fundamentally limited in its ability to account for 3D processes, particularly advection. However, as demonstrated in Baas et al. (2010) and Bosveld et al. (2014a), simple piecewise constant functions provided a reasonable first-order approximation of advective tendencies. These piecewise constant functions specified by Baas et al. (2010) and Bosveld et al. (2014a) were calculated from hindcasts, an approach not relevant in the context of real-time forecasting of the wind resource. Alternatively, the use of real-time data from an array of weather stations surrounding a particular location (e.g. at Cabauw) may allow for the anticipation of advective tendencies and the successful modelling of these tendencies within the SCM approach. For example, a sustained change in the observed 10-m wind speeds from a given sector relative to Cabauw could in principle be sufficient to calculate the timing of a change in advective momentum tendency as well as its magnitude. This approach (if successful) would be limited to the prediction of mesoscale or larger advective tendencies, and would likely not be useful in very stable conditions due to decoupling from the winds aloft from the surface.

Models considered in this thesis were driven by and compared to data only from the Cabauw tower. The flat surrounding terrain, the well-defined IBL and the strong baroclinic influence from the North Sea make Cabauw a favourable location for the investigation of atmospheric phenomena as well as the assessment of model performance. In practice, wind farms are located over a broad range of sites subject to a broad range of atmospheric conditions (e.g. flat and complex terrain, onshore and offshore conditions, cold and warm climates, proximity to urban centres, etc.). A useful next step in this research would be to compare SCM and 3D mesoscale model performance over a larger sample of terrains and atmospheric conditions. In general, an SCM is better suited to flat terrain with homogeneous surface roughness and temperatures while a mesoscale model would likely outperform the SCM in more complex terrain and atmospheric conditions. The availability of tall meteorological towers (i.e. 200 m or greater) is an obvious limitation to this approach. In the absence of tower data, LIDAR-based observations could be used (though only wind vector observations would be available). Alternatively, models could be assessed relative to a

high-resolution simulation such as LES (as in Cuxart et al. (2006)).

6.3 Concluding remarks

The field of wind energy meteorology has evolved considerably over the last 25 years, driven by increasing hub-height and blade diameters and advances in computing power. Extrapolation equations such as the logarithmic wind speed profile were generally sufficient up to about the year 2000 when only altitudes up to 80 m were of relevance to wind energy. With relevant altitudes now regularly above 200 m and the increasing contribution of wind energy to global energy production, the need for more robust models of the wind profile at high altitudes is of increasing importance. This need is especially important under conditions of stable stratification, where conventional extrapolation tools are most limited. The use of 3D atmospheric models is a more robust approach under such conditions but is limited by large computational cost and data requirements. Furthermore, 3D models do not generally make use of local observations (unless data assimilation is included, which is more computationally expensive). Computationally-efficient models that make use of minimal local observations are often advantageous, particularly for short-term wind resource forecasting or preliminary wind resource assessments where measurements are made at various locations at a site over a period of a year or more. To date, the middle ground between 1D extrapolation equations and 3D models has been largely unexplored. This thesis has helped to fill that research gap, and has demonstrated considerable value of the SCM approach. Overall, the SCM approach has been found to be of similar or better accuracy compared to a range of other models, while offering the best balance of observational data requirements, physical applicability, and computational requirements, as well as the most room for improvement. In this thesis, I have made a compelling case for the use of SCMs in wind resource assessment and forecasting, and it is my hope that the research presented here soon finds application in the field of wind energy meteorology.

Appendix A

Cabauw instrumentation and methods

This section provides information on the instrumentation and methods used at Cabauw for the various meteorological variables considered in this thesis. Material in this section is based on a detailed description at http://www.knmi.nl/bosveld.

A.1 Wind speed and direction

Wind speed and wind direction are measured at altitudes of 200, 140, 80, 40, 20, and 10 m. Measurements are made on booms in three different directions to avoid flow obstruction from the mast. For each 10 minute interval instruments are selected that are best exposed to the undisturbed wind. Wind speed is measured with the KNMI cup-anemometer. The cup diameter is 105 mm and the distance between the centre of the cups to the rotation axis is 100 mm. Anemometers are calibrated in the KNMI wind tunnel. Wind direction is measured with the KNMI wind vane. Calibration of the cup anemometers is done in the wind tunnel of KNMI, and sensors are replaced every 26 months. Accuracy of the cup anemometer is 0.5 ms^{-1}. The threshold velocity is 0.5 ms^{-1} and the resolution is 0.1 ms^{-1}. The accuracy of the wind vane is 3^o with a resolution of 1^o.

A.2 Temperature

Air temperatures are measured at altitudes of 200, 140, 80, 40, 20, 10, and 2 m. Air temperature is measured with a KNMI Pt500-element in an unventilated KNMI temperature hut. Calibration is done at KNMI. Temperature sensors are replaced every 38 months. Sensor accuracy is 0.1^oC and resolution is 0.1^oC.

A.3 Surface pressure

Air pressure is measured at an altitude of 2 m, located 200 m South-West of the main tower. A Paroscientific 1016B-01 instrument is used and replaced every 26 months. Accuracy is 0.1 hPa and resolution is 0.1 hPa.

A.4 Turbulent fluxes

Eddy correlation fluxes are measured at altitudes of 180, 100, 60, and 5 m. At each level a sonic anemometer/thermometer and an open path H2O/CO2 sensor is installed at the South-East (130^o) boom. Data from the 280-340^o sector was excluded from analysis due to mast interference.

Bibliography

Baas, P., F. Bosveld, G. Lenderink, E. van Meijgaard, and A. A. M. Holtslag: 2010, 'How to design single-column model experiments for comparison with observed nocturnal low-level jets'. *Quarterly Journal of the Royal Meteorological Society* **136**(648), 671–684.

Baas, P., F. C. Bosveld, H. K. Baltink, and A. Holtslag: 2009, 'A Climatology of Nocturnal Low-Level Jets at Cabauw'. *J Appl Meteorol Climatol* **48**(8), 1627–1642.

Baas, P., B. van de Wiel, L. van den Brink, and A. Holtslag: 2012, 'Composite hodographs and inertial oscillations in the nocturnal boundary layer'. *Q J R Meteorol Soc* **138**(663), 528–535.

Banta, R. M., Y. L. Pichugina, N. D. Kelley, R. M. Hardesty, and W. A. Brewer: 2013, 'Wind Energy Meteorology: Insight into Wind Properties in the Turbine-Rotor Layer of the Atmosphere from High-Resolution Doppler Lidar'. *B Amer Meteorol Soc* **94**(6), 883–902.

Beare, R. J., M. K. Macvean, A. A. Holtslag, J. Cuxart, I. Esau, J.-C. Golaz, M. A. Jimenez, M. Khairoutdinov, B. Kosovic, D. Lewellen, T. S. Lund, J. K. Lundquist, A. Mccabe, A. F. Moene, Y. Noh, S. Raasch, and P. Sullivan: 2006, 'An Intercomparison of Large-Eddy Simulations of the Stable Boundary Layer'. *Boundary-Layer Meteorology* **118**(2), 247–272.

Belair, S., J. Mailhot, J. Strapp, and J. MacPherson: 1999, 'An Examination of Local versus Nonlocal Aspects of a TKE-Based Boundary Layer Scheme in Clear Convective Conditions'. *J. Appl. Meteor. Climatol.* **38**, 1499–1518.

Beljaars, A.: 1987, *The Measurement of Gustiness at Routine Wind Stations - A Review*. Royal Netherlands Meteorological Institute. 52 pp.

Beljaars, A. and A. Holtslag: 1991, 'Flux Paramterization Over Land Surfaces for Atmospheric Models'. *J Appl Meteorol Climatol* **30**(3), 327–341.

Beljaars, A. and P. Viterbo: 1999, 'The role of the boundary layer in a numerical weather prediction model'. In: Holtslag, A.A.M and Duynkerke, P. G. (ed.): *Clear and Cloudy Boundary Layers*. North Holland Publishers.

Blackadar, A.: 1962, 'The vertical distribution of wind and turbulent exchange in a neutral atmosphere'. *J Geophys Res* **67**(8), 3095–3102.

Blackadar, A.: 1998, *Turbulence and Diffusion in the Atmosphere*. New York: Springer. 185 pp.

Bosveld, F., P. Baas, E. van Meijgaard, E. I. de Bruijn, G.-J. Steeneveld, and A. A. Holtslag: 2014a, 'The Third GABLS Intercomparison Case for Evaluation Studies of Boundary-Layer Models. Part A: Case Selection and Set-Up'. *Boundary-Layer Meteorology* **152**(2), 133–156.

Bosveld, F. C.: 2015, 'Personal correspondence'. Royal Netherlands Meteorlogical Institute.

Bosveld, F. C., P. Baas, G.-J. Steeneveld, A. A. Holtslag, W. M. Angevine, E. Bazile, E. I. de Bruijn, D. Deacu, J. M. Edwards, M. Ek, V. E. Larson, J. E. Pleim, M. Raschendorfer, and G. Svensson: 2014b, 'The Third GABLS Intercomparison Case for Evaluation Studies of Boundary-Layer Models. Part B: Results and Process Understanding'. *Boundary-Layer Meteorology* **152**(2), 157–187.

Burton, T., D. Sharpe, N. Jenkins, and E. Bossanyi: 2001, *Wind Energy Handbook*. John Wiley and Sons. 780 pp.

Businger, J., J. Wyngaard, I. Y., and E. Bradley: 1971, 'Flux-Profile Relationships in the Atmospheric Surface Layer'. *J. Atmos. Sci.* **28**, 181–189.

Carvalho, D., A. Rocha, M. Gmez-Gesteira, and C. Santos: 2012, 'A sensitivity study of the {WRF} model in wind simulation for an area of high wind energy'. *Environmental Modelling and Software* **33**(0), 23 – 34.

Carvalho, D., A. Rocha, M. Gmez-Gesteira, and C. S. Santos: 2014, 'Sensitivity of the {WRF} model wind simulation and wind energy production estimates to

planetary boundary layer parameterizations for onshore and offshore areas in the Iberian Peninsula'. *Applied Energy* **135**(0), 234 – 246.

Cheng, Y. and W. Brutsaert: 2005, 'Flux-profile relationships for wind speed and temperature in the stable atmospheric boundary layer'. *Boundary-Layer Meteorol* **114**(3), 519–538.

Clarke, R.: 1970, 'Observational Studies in Atmospheric Boundary Layer'. *Q J R Meteorol Soc* **96**(407), 91–114.

Cuxart, J., A. Holtslag, R. Beare, E. Bazile, A. Beljaars, A. Cheng, L. Conangla, M. Ek, F. Freedman, R. Hamdi, A. Kerstein, H. Kitagawa, G. Lenderink, D. Lewellen, J. Mailhot, T. Mauritsen, V. Perov, G. Schayes, G.-J. Steeneveld, G. Svensson, P. Taylor, W. Weng, S. Wunsch, and K.-M. Xu: 2006, 'Single-Column Model Intercomparison for a Stably Stratified Atmospheric Boundary Layer'. *Boundary-Layer Meteorology* **118**(2), 273–303.

De Bruin, H., R. Ronda, and B. Van De Wiel: 2000, 'Approximate Solutions For The Obukhov Length And The Surface Fluxes In Terms Of Bulk Richardson Numbers'. *Boundary-Layer Meteorology* **95**(1), 145–157.

Delage, Y.: 1974, 'A numerical study of the nocturnal atmospheric boundary layer'. *Q J R Meteorol Soc* **100**(425), 351–364.

Deppe, A., W. Gallus Jr., and E. Takle: 2013, 'A WRF Ensemble for Improved Wind Speed Forecasts at Turbine Height'. *Wea. Forecasting* **28**, 212–228.

Donda, J. M. M., B. J. H. Van de Wiel, F. C. Bosveld, F. Beyrich, G. J. F. van Heijst, and H. J. H. Clercx: 2013, 'Predicting Nocturnal Wind and Temperature Profiles Based on External Forcing Parameters'. *Boundary-Layer Meteorol* **146**(1), 103–117.

Draxl, C., A. N. Hahmann, A. Pea, and G. Giebel: 2014, 'Evaluating winds and vertical wind shear from Weather Research and Forecasting model forecasts using seven planetary boundary layer schemes'. *Wind Energy* **17**(1), 39–55.

Drechsel, S., G. J. Mayr, J. W. Messner, and R. Stauffer: 2012, 'Wind Speeds at Heights Crucial for Wind Energy: Measurements and Verification of Forecasts'. *J Appl Meteorol Climatol* **51**(9), 1602–1617.

Duynkerke, P.: 1991, 'Radiation Fog: A Comparison of Model Simulation with Detailed Observations'. *Mon. Wea. Rev.* **119**, 324–341.

Dyer, A. and B. Hicks: 1970, 'Flux-Gradient Relationships in Constant Flux Layers'. *Q J R Meteorol Soc* **96**(410), 715–721.

ECMWF: 2006, *Integrated Forecast System documentation of cycle 31r1. Model documentation of the European Centre for Medium Range Weather Forecast Model*. ECMWF.

Edwards, J. M., R. J. Beare, and A. J. Lapworth: 2006, 'Simulation of the observed evening transition and nocturnal boundary layers: Single-column modelling'. *Quarterly Journal of the Royal Meteorological Society* **132**(614), 61–80.

Emeis, S.: 2010, 'A simple analytical wind park model considering atmospheric stability'. *Wind Energy* **13**(5), 459–469.

Emeis, S.: 2013, *Wind Energy Meteorology - Atmospheric Physics for Wind Power Generation*. Dordrecht, Netherlands: Springer. 150 pp.

Emeis, S., K. Baumann-Stanzer, M. Piringer, M. Kallistratova, R. Kouznetsov, and Y. Yushkov: 2007, 'Wind and turbulence in the urban boundary layer - analysis from acoustic remote sensing data and fit to analytical relations'. *Meteorologische Zeitschrift* **16**(4), 393 – 406.

Etling, D.: 2002, *Theoretische Meteorologie Eine Einfuhrung, 2nd Edition*. Berlin, Heidelberg, New York: Springer. 376 pp.

Floors, R., C. Vincent, S.-E. Gryning, A. Pea, and E. Batchvarova: 2013, 'The Wind Profile in the Coastal Boundary Layer: Wind Lidar Measurements and Numerical Modelling'. *Boundary-Layer Meteorology* **147**(3), 469–491.

Galperin, B., L. Kantha, S. Hassid, and A. Rosati: 1988, 'A Quasi-equilibrium turbulent energy model for geophysical flows'. *J. Atmos. Sci.* **45**(1), 55–62.

Garratt, J.: 1994, *The Atmospheric Boundary Layer*. Cambridge University Press. 335 pp.

Gibbs, J., E. Fedorovich, and A. Shapiro: 2015, 'Revisiting Surface Heat-Flux and Temperature Boundary Conditions in Models of Stably Stratified Boundary-Layer Flows'. *Boundary-Layer Meteorology* **154**(2), 171–187.

Giebel, G.: 2011, *The State-Of-The-Art in Short Term Prediction of Wind Power - A Literature Overview, 2nd Edition*. ANEMOS. 8 pp.

Gryning, S.-E. and E. Batchvarova: 2008, 'Modelling of the Urban Wind Profile'. In: C. Borrego and A. Miranda (eds.): *Air Pollution Modeling and Its Application XIX*, NATO Science for Peace and Security Series Series C: Environmental Security. Springer Netherlands, pp. 18–27.

Gryning, S.-E., E. Batchvarova, B. Bruemmer, H. Jorgensen, and S. Larsen: 2007, 'On the extension of the wind profile over homogeneous terrain beyond the surface boundary layer'. *Boundary-Layer Meteorol* **124**(2), 251–268.

Hicks, B.: 1976, 'Wind Profile Relationships from Wangara Experiment'. *Q J R Meteorol Soc* **102**(433), 535–551.

Holton, J.: 2004, *An Introduction to Dynamic Meteorology, 4th Edition*. Burlington, MA, U.S.A.: Elsevier. 535 pp.

Holtslag, A.: 1982, 'The derivation of fluxes from profiles in perturbed areas'. *Boundary-Layer Meteorol* **24**, 35–55.

Holtslag, A.: 1984, 'Estimates of diabatic wind speed profiles from near-surface weather observations'. *Boundary-Layer Meteorology* **29**(3), 225–250.

Holtslag, A.: 2014, 'Introduction to the Third GEWEX Atmospheric Boundary Layer Study (GABLS3)'. *Boundary-Layer Meteorology* **152**(2), 127–132.

Hong, S. and H. Pan: 1996, 'Nonlocal Boundary Layer Vertical Diffusion in a Medium-Range Forecast Model'. *Mon. Wea. Rev.* **124**, 2322–2339.

IEA: 2014, 'IEA WIND 2013 Annual Report'. Technical report, Executive Committee of the Implementing Agreement for Co-operation in the Research, Development, and Deployment of Wind Energy Systems of the International Energy Agency.

Janjic, Z.: 2002, *Nonsingular Implementation of the Mellor-Yamada Level 2.5 Scheme in the NCEP Meso model*. NCEP Office Note 437. 61 pp.

Jimenez, P., G.-R. J.F., E. Garca-Bustamante, J. Navarro, J. Montvez, J. Vil-Guerau de Arellano, J. Dudhia, and A. Muoz-Roldan: 2010, 'Surface wind regionalization over complex terrain: evaluation and analysis of a high-resolution wrf simulation'. *J. Appl. Meteor. Climatol.* pp. 268–287.

Jimenez, P. A.: 2015, 'Personal correspondence'. -.

Kleczek, M. A., G.-J. Steeneveld, and A. Holtslag: 2014, 'Evaluation of the Weather Research and Forecasting Mesoscale Model for GABLS3: Impact of Boundary-Layer Schemes, Boundary Conditions and Spin-Up'. *Boundary-Layer Meteorology* **152**(2), 213–243.

Kou-Fang Lo, A.: 1996, 'On the role of roughness lengths in flux parameterizations of boundary-layer models'. *Boundary-Layer Meteorology* **80**(4), 403–413.

Kumar, P. and M. Sharan: 2012, 'Parameterization of the eddy diffusivity in a dispersion model over homogeneous terrain in the atmospheric boundary layer'. *Atmos Res* **106**(0), 30 – 43.

Landtz, E., M. Hand, and R. Wiser: 2012, 'The Past and Future Cost of Wind Energy'. Technical report, National Renewable Energy Laboratory.

Lange, M. and U. Focken: 2005, *Physical Approach to Short-Term Wind Power Prediction*. Springer. 167 pp.

Mahrt, L.: 1998, 'Stratified atmospheric boundary layers and breakdown of models'. *Theor Comput Fluid Dyn* **11**(3-4), 263–279.

Mahrt, L.: 1999, 'Stratified atmospheric boundary layers'. *Boundary-Layer Meteorol* **90**(3), 375–396.

Mahrt, L.: 2014, 'Stably Stratified Atmospheric Boundary Layers'. *Annu. Rev. Fluid Mech.* **46**, 23–45.

Mahrt, L. and D. Vickers: 2002, 'Contrasting vertical structures of nocturnal boundary layers'. *Boundary-Layer Meteorology* **105**(2), 351–363.

Mahrt, L. and D. Vickers: 2006, 'Extremely weak mixing in stable conditions'. *Boundary-Layer Meteorol* **119**(1), 19–39.

Marjanovic, N., S. Wharton, and F. K. Chow: 2014, 'Investigation of model parameters for high-resolution wind energy forecasting: Case studies over simple and complex terrain'. *Journal of Wind Engineering and Industrial Aerodynamics* **134**(0), 10 – 24.

Mellor, G. L. and T. Yamada: 1982, 'Development of a turbulence closure model for geophysical fluid problems'. *Reviews of Geophysics* **20**(4), 851–875.

Monin, A. and A. Obukhov: 1954, 'Basic Laws of Turbulence Mixing in the Surface Layer of the Atmosphere'. *Q J R Meteorol Soc* **24**, 163–187.

Monteiro, C., R. Bessa, V. Miranda, A. Botterud, J. Wang, and G. Conzelmann: 2009, *Wind Power Forecasting: State-of-the-Art 2009*. Argonne National Laboratory. 216 pp.

Motta, M., R. Barthelmie, and P. Volund: 2005, 'The influence of non-logarithmic wind speed profiles on potential power output at Danish offshore sites'. *Wind Energy* **8**(2), 219–236.

Nieuwstadt, F.: 1978, 'The computation of the friction velocity u* and the temperature scale T* from temperature and wind velocity profiles by least-square methods'. *Boundary-Layer Meteorol* **14**(2), 235–246.

Nieuwstadt, F.: 1984, 'The Turbulent Structure of the Stable, Noctural Boundary Layer'. *J Atmos Sci* **41**(14), 2202–2216.

Nunalee, C. G. and S. Basu: 2014, 'Mesoscale modeling of coastal low-level jets: implications for offshore wind resource estimation'. *Wind Energy* **17**(8), 1199–1216.

Panofsky, H.: 1973, 'Tower Micrometeorology'. In: *Haugen DA (ed) Workshop on Micrometeorology*. pp. 151–176, American Meteorological Society.

Pena, A., S. Gryning, and C. Hasager: 2010, 'Comparing mixing-length models of the diabatic wind profile over homogeneous terrain'. *Theor Appl Climatol* **100**(3-4), 325–335.

Persson, P. O. G., C. W. Fairall, E. L. Andreas, P. S. Guest, and D. K. Perovich: 2002, 'Measurements near the Atmospheric Surface Flux Group tower at SHEBA: Near-surface conditions and surface energy budget'. *Journal of Geophysical Research: Oceans* **107**(C10), SHE 21–1–SHE 21–35.

Petersen, E. L., N. G. Mortensen, L. Landberg, J. Hjstrup, and H. P. Frank: 1998, 'Wind power meteorology. Part I: climate and turbulence'. *Wind Energy* **1**(1), 2–22.

Poulos, G., W. Blumen, D. Fritts, J. Lundquist, J. Sun, S. Burns, C. Nappo, R. Banta, R. Newsom, J. Cuxart, E. Terradellas, B. Balsley, and M. Jensen: 2002, 'CASES-99: A Comprehensive Investigation of the Stable Nocturnal Boundary Layer'. *Bull. Amer. Meteor. Soc.* **83**, 555–581.

Sathe, A., S.-E. Gryning, and A. Pea: 2011, 'Comparison of the atmospheric stability and wind profiles at two wind farm sites over a long marine fetch in the North Sea'. *Wind Energy* **14**(6), 767–780.

Sathe, A., J. Mann, T. Barlas, and Bier: 2012, 'Influence of atmospheric stability on wind turbine loads'. *Wind Energy* pp. 1013–1032.

Seidel, D. J., C. O. Ao, and K. Li: 2010, 'Estimating climatological planetary boundary layer heights from radiosonde observations: Comparison of methods and uncertainty analysis'. *J Geophys Res* **115**(D16).

Sharan, M. and Aditi: 2009, 'Performance of various similarity functions for nondimensional wind and temperature profiles in the surface layer in stable conditions'. *Atmos Res* **94**(2), 246–253.

Shimada, S., T. Ohsawa, S. Chikaoka, and K. Kozai: 2011, 'Accuracy of the Wind Speed Profile in the Lower PBL as Simulated by the WRF Model'. *SOLA* **7**, 109–112.

Skamarock, W., J. Klemp, J. Dudhia, D. Gill, D. Barker, M. Duda, X. Huang, W. Wang, and J. Powers: 2008, 'A Description of the Advanced Research WRF Version 3'. Technical report, National Center for Atmospheric Research.

Smith, R. B.: 1990, 'A scheme for predicting layer clouds and their water content in a general circulation model'. *Quarterly Journal of the Royal Meteorological Society* **116**(492), 435–460.

Sorbjan, Z.: 1988, 'Structure of the stably-stratified boundary layer during the SESAME-1979 experiment'. *Boundary-Layer Meteorol* **44**(3), 255–266.

Sorbjan, Z.: 2012, 'A Study of the Stable Boundary Layer Based on a Single-Column K-Theory Model'. *Boundary-Layer Meteorology* **142**(1), 33–53.

Sorbjan, Z.: 2014, 'Modelling of the Evolving Stable Boundary Layer'. *Boundary-Layer Meteorology* **151**(3), 407–428.

Sorbjan, Z. and A. Grachev: 2010, 'An Evaluation of the Flux-Gradient Relationship in the Stable Boundary Layer'. *Boundary-Layer Meteorol* **135**(3), 385–405.

Sterk, H. A. M., G. J. Steeneveld, and A. A. M. Holtslag: 2013, 'The role of snow-surface coupling, radiation, and turbulent mixing in modeling a stable boundary layer over Arctic sea ice'. *Journal of Geophysical Research: Atmospheres* **118**(3), 1199–1217.

Storm, B. and S. Basu: 2010, 'The WRF Model Forecast-Derived Low-Level Wind Shear Climatology over the United States Great Plains'. *Energies* **3**(2), 258–276.

Storm, B., J. Dudhia, S. Basu, A. Swift, and I. Giammanco: 2009, 'Evaluation of the Weather Research and Forecasting model on forecasting low-level jets: implications for wind energy'. *Wind Energy* **12**(1), 81–90.

Stull, R.: 1988, *An Introduction to Boundary-Layer Meteorology*. Dordrecht, Netherlands: Kluwer Academic Publishers. 670 pp.

Sukoriansky, S.: 2008, *Implementation of the Quasi-Normal Scale Elimination (QNSE) Model of Stably Stratified Turbulence in WRF*. Report on WRF-DTC Visit, Developmental Testbed Center. 109 pp.

Svensson, G., A. Holtslag, V. Kumar, T. Mauritsen, G. Steeneveld, W. Angevine, E. Bazile, A. Beljaars, E. de Bruijn, A. Cheng, L. Conangla, J. Cuxart, M. Ek, M. Falk, F. Freedman, H. Kitagawa, V. Larson, A. Lock, J. Mailhot, V. Masson, S. Park, J. Pleim, S. Sderberg, W. Weng, and M. Zampieri: 2011, 'Evaluation of the Diurnal Cycle in the Atmospheric Boundary Layer Over Land as Represented by a Variety of Single-Column Models: The Second GABLS Experiment'. *Boundary-Layer Meteorology* **140**(2), 177–206.

Tennekes, H.: 1973, 'Similarity Laws and Scale Relations in Planetary Boundary Layers'. In: *Workshop on Micrometeorology*. pp. 177–216, American Meteorological Soceity.

Tijm, A., A. Holtslag, and A. van Delden: 1999, 'Observations and Modeling of the Sea Breeze with the Return Current'. *Mon. Wea. Rev.* **127**, 625–640.

Troen, I. and E. Petersen: 1989, *European Wind Atlas*. Roskilde: Riso National Laboratory. 656 pp.

Unden, P.: 2002, *HIRLAM-5 Scientific Documentation*. HIRLAM-5 Project, SMHI. 144 pp.

Van de Wiel, B., A. Moene, and H. Jonker: 2012a, 'The Cessation of Continuous Turbulence as Precursor of the Very Stable Nocturnal Boundary Layer'. *J. Atmos. Sci.* pp. 3097–3115.

Van de Wiel, B., A. Moene, G. Steeneveld, P. Baas, F. Bosveld, and A. Holtslag: 2010, 'A Conceptual View on Inertial Oscillations and Nocturnal Low-Level Jets'. *J Atmos Sci* **67**(8), 2679–2689.

van de Wiel, B., A. Moene, G. Steeneveld, O. Hartogensis, and A. Holtslag: 2007, 'Predicting the Collapse of Turbulence in Stably Stratified Boundary Layers'. *Flow, Turbulence and Combustion* **79**(3), 251–274.

Van de Wiel, B. J. H., H. J. J. Jonker, P. Baas, S. Basu, J. M. M. Donda, J. Sun, and A. A. M. Holtslag: 2012b, 'The Minimum Wind Speed for Sustainable Turbulence in the Nocturnal Boundary Layer'. *J. Atmos. Sci.* pp. 3116–3127.

Van de Wiel, B. J. H., R. Ronda, A. F. Moene, D. H. A. R., and A. A. M. Holtslag: 2002, 'Intermittent Turbulence and Oscillations in the Stable Boundary Layer over Land. Part I: A Bulk Model'. *J. Atmos. Sci.* pp. 942–958.

van den Berg, G.: 2008, 'Wind turbine power and sound in relation to atmospheric stability'. *Wind Energy* **11**(2), 151–169.

van den Hurk, B. and A. Holtslag: 1997, 'On the bulk parameterization of surface fluxes for various conditions and parameter ranges'. *Boundary-Layer Meteorology* **82**(1), 119–133.

Van Ulden, A. and J. Wieringa: 1996, 'Atmospheric boundary layer research at Cabauw'. *Boundary-Layer Meteorology* **78**(1-2), 39–69.

Verkaik, J. and A. Holtslag: 2007, 'Wind profiles, momentum fluxes and roughness lengths at Cabauw revisited'. *Boundary-Layer Meteorol* **122**(3), 701–719.

Webb, E.: 1970, 'Profile Relationships: The Log-Linear Range and Extension to Strong Stability'. *Q J R Meteorol Soc* **96**(407), 67–90.

Weng, W. and P. Taylor: 2003, 'On Modelling the One-Dimensional Atmospheric Boundary Layer'. *Boundary-Layer Meteorology* **107**(2), 371–400.

Weng, W. and P. Taylor: 2006, 'Modelling the One-Dimensional Stable Boundary Layer with an E Turbulence Closure Scheme'. *Boundary-Layer Meteorology* **118**(2), 305–323.

WPM: 2015, 'The 10 Biggest Turbines in the World'. *Wind Power Monthly*.

Yang, Q., L. Berg, M. Pekour, J. Fast, R. Newsom, M. Stoelinga, and C. Finley: 2014, 'Evaluation of WRF-Predicted Near-Hub-Height Winds and Ramp Events over a Pacific Northwest Site with Complex Terrain'. *J. Appl. Meteor. Climatol.* **52**, 1753–1763.

Zhang, H., Z. Pu, and Z. X.: 2013, 'Examination of errors in near-surface temperature and wind from WRF numerical simulations in regions of complex terrain'. *Weather Forecast* **28**(3), 893–914.

Zilitinkevich, S. S.: 1975, 'Resistance laws and prediction equations for the depth of the planetary boundary layer'. *J. Atmos. Sci.* **32**, 741–752.